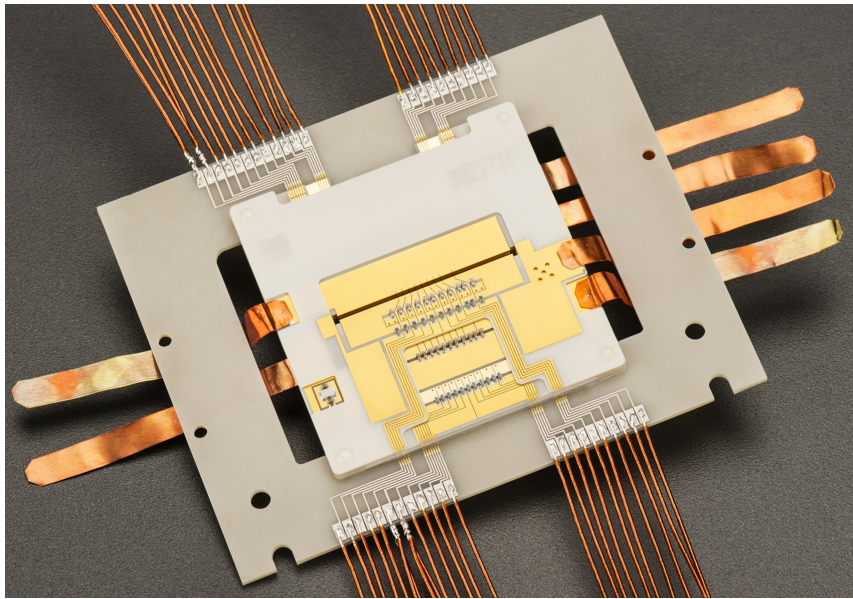

Development and characterization of a linear ion trap for an improved optical clock performance



**Von der QUEST-Leibniz-Forschungsschule der
Gottfried Wilhelm Leibniz Universität Hannover
zur Erlangung des Grades**

**Doktor der Naturwissenschaften
Dr. rer. nat.**

**genehmigte Dissertation von
Dipl.-Phys. Tobias Burgermeister
geboren am 8. August 1984 in Groß-Gerau**

2019

Referentin: Priv.-Doz. Dr. Tanja E. Mehlstäubler
Korreferent: Prof. Dr. Piet O. Schmidt
Korreferent: Prof. Dr. Christof Wunderlich
Tag der Promotion: 12. Juli 2019

Zusammenfassung

In mehreren Experimenten haben Frequenzstandards auf der Basis von einzelnen Ionen hervorragende Ergebnisse erzielt und nähern sich einer relativen Frequenzunsicherheit von 10^{-18} an. Eine weitere Reduzierung der Frequenzunsicherheit wäre durch eine verbesserte Ionenfalle möglich, da dominante Beiträge der Frequenzunsicherheit auf die Eigenschaften der Ionenfalle zurückzuführen sind. Aufgrund der Abfrage eines einzelnen Ions sind diese Frequenznormale zur Zeit durch das intrinsisch niedrige Signal-Rausch-Verhältnis limitiert und benötigen lange Mittelungszeiten in der Größenordnung von mehreren Tagen. Diese Limitierung ist für verschiedene Anwendungen, die eine hohe Frequenzauflösung nach kurzen Mittelungszeiten erfordern, ein kritischer Punkt. Die Frequenzstabilität kann durch eine höhere Anzahl von Uhrenionen verbessert werden. Allerdings werden durch diesen Ansatz auch die Anforderungen an die Ionenfalle weiter erhöht. Aus diesem Grund ist für die Realisierung einer Multi-Ionen Uhr, die gleichzeitig die Frequenzstabilität und -unsicherheit weiter verringern soll, die Kontrolle über die Eigenschaften der Ionenfalle von entscheidender Bedeutung.

Diese Dissertation setzt frühere Arbeiten zur Realisierung einer optischen Multi-Ionen-Uhr auf der Basis von Coulomb-Kristallen aus $^{115}\text{In}^+$ -Ionen, die durch $^{172}\text{Yb}^+$ -Ionen sympathisch gekühlt werden, fort. Das existierende Design einer segmentierten linearen Ionenfalle wurde optimiert und es wurde ein zuverlässiger Herstellungsprozess basierend auf goldbeschichteten Aluminiumnitrid-Wafern entwickelt. Durch Fertigungstoleranzen von weniger als $10\ \mu\text{m}$ konnte die axiale Mikrobewegungsamplitude deutlich reduziert werden. Es wird gezeigt, dass in einem Bereich von über $300\ \mu\text{m}$ der Beitrag der dreidimensionalen Mikrobewegung zur Frequenzunsicherheit unterhalb von 10^{-19} ist. Zusätzlich wurde die radiale Heizrate der Falle mit $1.1\ \text{Phononen/s}$ bei einer Fallenfrequenz von $490\ \text{kHz}$ bestimmt. Die Frequenzverschiebung durch Zeitdilatation durch die Heizrate der radialen Fallenachse beträgt damit $(2.1 \pm 0.3) \times 10^{-20}\ \text{s}^{-1}$.

Das Fallendesign wurde ebenso auf einen geringen Anstieg der Falltemperatur durch die angelegte HF-Spannung optimiert. Die Messungen der Falltemperatur mit den auf der Falle installierten Pt100 Sensoren zeigten einen maximalen Temperaturanstieg von $1.21\ \text{K}$ bei einer HF-Spannungsamplitude von $1\ \text{kV}$. Durch den Vergleich der Messergebnisse mit FEM-Simulationen wurde der Beitrag der Falltemperatur zur Frequenzverschiebung durch die Schwarzkörperstrahlung mit 2.4×10^{-20} bestimmt.

Da die Ionenfalle eine sehr gute Kontrolle über Coulomb-Kristalle bietet, eignet sie sich auch hervorragend für Experimente mit atomaren Vielteilchensystemen. Hierzu werden in dieser Arbeit Untersuchungen topologischer Defekte in zweidimensionalen Coulomb-Kristallen vorgestellt. Der Schwerpunkt lag dabei auf der Analyse des Einflusses von Massendefekten und externen elektrischen Feldern auf die Stabilität der topologischen Defekte. Es wird gezeigt wie dieser Einfluss genutzt werden kann, um die Defekte gezielt zu manipulieren und sie deterministisch zu produzieren.

Schlagwörter: Ionenfallen, optische Uhren, Mikrobewegung, Coulomb-Kristalle, Vielteilchensysteme

Abstract

Single ion frequency standards have demonstrated in several experiments excellent results and are approaching fractional frequency uncertainties of 10^{-18} . As dominant contributions to the uncertainty are linked to the ion trap properties a further reduction would be possible by an improved ion trap. Due to the interrogation of a single ion these frequency standards are currently limited by the intrinsically low signal-to-noise ratio and require long averaging times on the order of several days. This limitation is critical for various applications that require a high frequency resolution on short timescales. One possibility to improve the clock stability is to increase the number of clock ions. However, this approach further increases the requirements for the ion trap. Therefore, for the realization of a multi-ion clock that aims at simultaneously reducing the frequency stability and uncertainty the control over the characteristics of the ion trap is crucial.

This thesis continues previous work towards the realization of a multi-ion optical clock based on ion Coulomb crystals of $^{115}\text{In}^+$ ions which are sympathetically cooled by $^{172}\text{Yb}^+$ ions. The existing design for a segmented linear ion trap has been refined and a reliable trap manufacturing process for a trap based on gold coated aluminium nitride wafers has been developed. Manufacturing tolerances below $10\ \mu\text{m}$ allowed to reduce the axial micromotion amplitudes substantially. For a region of more than $300\ \mu\text{m}$ the uncertainty contribution of the three-dimensional micromotion amplitude is shown to be below 10^{-19} . Additionally the radial ion heating rate of the trap has been measured to be $1.1\ \text{phonons/s}$ for a trap frequency of $490\ \text{kHz}$. The time dilation shift due to the heating rate on the radial trap axis is found to be $(2.1 \pm 0.3) \times 10^{-20}\ \text{s}^{-1}$.

The trap design has also been optimized for a low trap temperature rise due to the applied rf voltage. Trap temperature measurements with Pt100 sensors installed on the trap showed a maximum temperature increase of $1.21\ \text{K}$ at an rf voltage amplitude of $1\ \text{kV}$. By comparing the measurement results to FEM simulations the uncertainty contribution of the trap temperature to the black-body radiation shift has been deduced to be 2.4×10^{-20} .

As the ion trap provides a high level of control on Coulomb crystals it also provides an ideal test bed for studying atomic many-body systems. This work presents results of the investigations on topological defects in two-dimensional Coulomb crystals. The emphasis was placed on the effects of mass defects and external electric fields on the stability of the topological defects. It is shown that these effects can be used to manipulate and create topological defects deterministically.

Keywords: ion traps, optical clocks, excess micromotion, Coulomb crystals, many-body systems

Contents

Contents	vii
1. Introduction	1
2. Theoretical Background	5
2.1. Optical Multi-Ion Clocks	5
2.1.1. $^{115}\text{In}^+$ Clock Ion Properties	8
2.2. Linear Paul Traps	9
2.2.1. Trapping of Single Ions	10
2.2.2. Linear Ion Coulomb Crystals	14
2.3. Interaction of Laser Light with Trapped Ions	16
2.4. Laser Cooling	19
2.4.1. Doppler Cooling	19
2.4.2. Resolved Sideband Cooling	20
2.5. Systematic Clock Frequency Shifts	23
2.5.1. Motional Frequency Shifts	23
2.5.2. Frequency Shifts due to Electromagnetic Fields	25
2.5.3. Other Frequency Shifts	27
3. Ion Trap Development	31
3.1. Main Targets of the Trap Development Process	31
3.2. Ion Trap Geometry	33
3.3. Calculations of the Electric Fields of the Trap	37
3.4. Thermal Management and Choice of Materials	42
3.5. Trap Manufacturing Process	44
3.6. Measurements of the Trap Geometry	52
3.6.1. Geometry Measurement Tools and their Uncertainty	52
3.6.2. Single Trap Wafer Geometry	54
3.6.3. Alignment Errors	56
3.6.4. Conclusions of the Geometry Measurements	57
4. Experimental Setup and Sideband Spectroscopy Sequence	59
4.1. Vacuum Setup	59
4.2. Trap Voltages	61
4.2.1. RF Circuit	61
4.2.2. DC Voltages	62

4.3.	Optical Setup	66
4.3.1.	$^{172}\text{Yb}^+$ Term Scheme	66
4.3.2.	Laser Setup and Beam Geometry	67
4.3.3.	Ion Imaging	72
4.4.	Sideband Spectroscopy Sequence	72
4.4.1.	Selection Rules for Quadrupole Transitions	72
4.4.2.	Ground State Cooling Sequence	74
5.	Ion Trap Characterization	79
5.1.	Temperature of the Ion Trap	79
5.2.	Secular Frequencies	87
5.3.	Excess Micromotion Measurements	94
5.3.1.	Photon-Correlation Spectroscopy	94
5.3.2.	Experimental Implementation	96
5.3.3.	Results of Micromotion Measurements	98
5.4.	Heating Rate Measurement	100
6.	Creation and Dynamics of Topological Defects in Ion Coulomb Crystals	103
7.	Summary and Outlook	117
A.	Appendix	123
A.1.	Trap Dimensions of Trap Potential Simulator	123
A.2.	Aluminium Nitride Material Properties	124
A.3.	DC Voltage Supply - Circuit Diagram	125
A.4.	Calibration of Temperature Sensors on Trap IV	126
A.5.	Trap Potential Simulator	128

List of Acronyms

AIN	aluminium nitride
AOM	acousto-optic modulator
BBR	black-body radiation
BSB	blue sideband transition
CMI	Czech Metrology Institute, national metrology institute of the Czech Republic
CT	computed tomography
ECDL	external-cavity diode laser
EMCCD	electron-multiplying CCD (charge-coupled device)
EMM	excess micromotion
FEM	finite element method
FWHM	full width at half-maximum
IMM	intrinsic micromotion
ICC	ion Coulomb crystal
IR	infrared
NEP	N-ethyl-2-pyrrolidone
OFHC	oxygen-free high thermal conductivity
PMT	photomultiplier tube
PPLN	periodically poled lithium niobate
QPN	quantum projection noise
rf	radio frequency
RSB	red sideband transition
RTD	resistance temperature detector

SEM	scanning electron microscope
SHG	second-harmonic generation
SI	International System of Units, abbreviated from the French <i>Système international</i> (d'unités)
SMD	surface-mount device
SNR	signal-to-noise ratio
TAC	time-to-amplitude converter
UHV	ultra-high vacuum
ZnSe	Zinc Selenide

1. Introduction

The measurement of time has always played an important role for mankind. For many centuries time measurements relied mainly on the observation of the sun, the moon and the stars in order to determine days, seasons and years. Thus the frequency of the Earth's rotation and of Earth's orbit around the sun have been used to define time scales. For measurements of shorter time periods other timekeeping devices such as water clocks, hour glasses and mechanical clocks have been constructed [1]. Major improvements of man-made mechanical clocks have been the pendulum clock invented by Christiaan Huygens in 1656 and the marine chronometers developed by John Harrison throughout the 18th century. The latter allowed the increasing number of seafarers a safer navigation, because these clocks allowed a simple and reliable determination of their longitude. However, Earth's rotation remained the time standard as it still provided a frequency accuracy, which could not be reached with mechanical clocks. With the invention of quartz crystal clocks in the 1930s and 1940s, it was discovered that the Earth's rotation frequency is fluctuating, leading to day length variations on the order of 1 ms [2]. Besides a long term deceleration due to tidal effects the fluctuations are attributed to changing mass distributions of the atmosphere and the Earth itself. Therefore in 1956 the SI second was redefined by the International Committee of Weights and Measures as a fixed fraction of the tropical year, which shows smaller fluctuations.

The next breakthrough in the development of accurate clocks was the first realization of an atomic clock that uses the microwave transition between the two hyperfine levels of the ground state of the ^{133}Cs atom as the reference frequency [3]. The first suggestion to use atoms for time measurements has been made by James Clerk Maxwell and dates back to 1870 [4]. In 1967, this approach finally led to the current definition of the SI second as the duration of 919 263 177 periods of the radiation corresponding to the above mentioned resonance frequency of ^{133}Cs [5]. Since then Cs atomic clocks have been improved continuously and nowadays approach fractional frequency uncertainties of 1×10^{-16} [6]. The existence of these highly precise clocks enabled the development of new technologies such as the global navigation satellite systems.

A number of further technological breakthroughs enabled the realization of optical clocks, which surpass the performance of microwave clocks and approach fractional frequency uncertainties of 10^{-18} [7–9]. Among others these breakthroughs have been the development of lasers [10, 11] as an intrinsically coherent and intense light source, the development of laser cooling techniques [12, 13], the development of highly stable laser sources with subhertz linewidths [14] and the invention of optical frequency

combs [15]. With the help of laser light atoms can be cooled to temperatures below 1 mK and prepared in the desired electronic and motional state. The highly stable laser sources are used as a flywheel or short-term frequency reference. The stabilized laser has to maintain the frequency stability in between two interrogations of the atomic reference transition. Finally the optical frequency comb provides a fixed link between the optical oscillations and easily countable oscillations in the radio frequency (rf) regime.

Besides the improvement of timekeeping the higher accuracy of optical clocks also has impact on further applications [16]. One field is the search for new physics beyond the standard model and for possible violations of Lorentz symmetry. The former is looking for temporal or spatial variations of fundamental constants such as the fine-structure constant α or the proton-electron mass ratio $\mu = \frac{m_p}{m_e}$ [17, 18]. Lorentz symmetry can be tested by observing the frequency differences in atomic states with different spatial orientations and track those differences while the Earth is rotating around its axis [19–21]. Another emerging application is the field of chronometric levelling in geodesy [22, 23]. These experiments make use of the relativistic time dilation shift due to the gravitational potential of the Earth. Fractional frequency uncertainties of 10^{-18} are needed for these experiments to resolve height differences at the level of 1 cm. Conversely, for a frequency comparison with a systematic uncertainty at the level of 10^{-18} , the height of the clock ion needs to be known with centimetre precision.

Of the various realizations of optical clocks, systems with trapped ions are among the most successful. For these experiments clock ions are trapped inside a quadrupole ion trap, which is often also referred to as Paul trap. The invention of these traps in the 1950s have enabled spectroscopy on individual atoms for the first time and additionally allowed particle mass determination with unprecedented accuracy [24, 25]. The quadrupole ion trap uses a combination of static and rf electric fields to create confinement in all three dimensions. The trap provides high trap depths on the order of several electronvolts, which allows to trap ions at room temperature and to store them in the trap for several days to months. Due to the tight confinement ions in the trap can be localized to within a few nanometres. This allows to precisely control and characterize external electric and magnetic fields at the ion position, which is a prerequisite for achieving low systematic frequency uncertainties. Although the trap uses electric fields to generate the confinement, the field vanishes in the centre of the trap and in first order do not disturb the internal energy levels.

Today the most accurate realizations of ion clocks use a single clock ion, because it allows to achieve the lowest systematic uncertainties [8, 9, 26]. A serious limitation of this approach is the low signal-to-noise ratio (SNR) of the binary signal of the single ion. Because of this single ion clocks require long averaging times on the order of several days in order to reduce the statistical uncertainty to the level of the estimated inaccuracy. Besides the technical challenge to realize these long averaging times they are also limiting the use of ion clocks for applications that want to measure frequency

fluctuations on shorter timescales. One approach to reduce averaging times is to increase the number of reference ions [27, 28], which is the basic idea of the experiment presented in this thesis.

If multiple ions are loaded into an ion trap and are cooled to sufficiently low temperatures they form a crystalline structure also referred to as ion Coulomb crystals (ICCs). The ion configuration of the ICCs are dependent on the interplay of the confining trap potential and the repulsive Coulomb force of the neighbouring ions. Depending on the shape of the trap potential these crystals can be one-, two- or three-dimensional. The most promising configuration for clock operation is a one-dimensional crystal in which the ions form a linear string on the trap axis of a linear ion trap. The unavoidable existence of static electric field gradients within such a setup limits the choice of atomic elements for clock operation as the shift due to the electric quadrupole moment would increase the systematic error significantly. Therefore, in the presented experiment it is planned to build a multi-ion clock with $^{115}\text{In}^+$ ions, as the considered clock transition connects two states with vanishing quadrupole moment. As the $^{115}\text{In}^+$ term scheme only provides a narrow cooling transition $^{172}\text{Yb}^+$ ions are trapped simultaneously to provide sympathetic cooling. Additionally $^{172}\text{Yb}^+$ can be used to characterize the experiment as it also provides two narrow clock transitions. In fact all experiments shown in this thesis have only used $^{172}\text{Yb}^+$.

An analysis of the dominant contributions to the total uncertainty of single ion clocks of different experiments reveals that many of those contributions are linked directly or indirectly to the characteristics of the ion trap. For a multi-ion clock some of these uncertainties are even expected to further increase. Therefore for the realization of a multi-ion clock it is indispensable to develop an ion trap design that minimizes these contributions to the uncertainty budget. Specifically this means that the trap must provide the lowest possible axial micromotion amplitudes, low external ion heating rates and a low and well-known temperature increase of the trap due to rf losses. The micromotion and the ion heating rates contribute to the motional time dilation shift. The trap temperature needs to be known for the determination of the black-body radiation (BBR) shift, which is the ac Stark shift due to the black-body radiation emitted by the environment of the ion. A scalable segmented linear ion trap design that fulfils these requirements has been presented initially in Ref. [27] and a prototype trap with this design has been characterized in Ref. [29, 30].

The aim of this thesis was to refine the existing trap design and to develop a manufacturing process for an ion trap with the best possible characteristics for the realization of a multi-ion clock. The target was to further reduce the contributions of the ion trap to the fractional frequency uncertainty. This needed to be proven by measurements of the trap characteristics.

The thesis is organized as follows. Chapter 2 reviews the theoretical foundations of optical clocks, linear ion traps, laser cooling techniques and of the relevant frequency shifts. In chapter 3 the main targets of the trap development and the trap design

are introduced. It is explained in detail how the design goals influence the targeted dimensional tolerances and the choice of the materials to build the trap. This is followed by a detailed description of the trap manufacturing process. To continuously improve this process in total five ion traps have been manufactured. Each trap consists of four aluminium nitride (AlN) wafers with sputtered gold electrodes. The semi-monolithic design allows to achieve low manufacturing tolerances. In the last part of chapter 3 the results of the trap geometry measurements are presented. Chapter 4 is dedicated to the description of the experimental setup and the experimental cycle that was implemented for ground state cooling of $^{172}\text{Yb}^+$. One of the five ion traps is characterized in chapter 5. This includes the measurements of the trap temperature, a comparison between measured and calculated trap frequencies, the measurement of the micromotion amplitudes in two of the seven trap segments and the measurement of the ion heating rates. In chapter 6 the excellent trap properties for the manipulation of ICCs are used to study topological defects that are formed during the phase transition from a one-dimensional to a two-dimensional crystal. Additionally the influence of mass defects and external electric fields on the defect stability are discussed. Chapter 7 summarizes the results of this thesis and gives an outlook on possible next steps for the ion trap and the experiment.

2. Theoretical Background

This chapter includes a brief description of the theoretical approaches that are used to describe the physical systems that are investigated in this work. The description focusses on the specific setup that was used in the experiment. For calculated numbers and graphs typical experimental parameters have been assumed. More detailed and more general theoretical descriptions can be found in the references mentioned in the text.

2.1. Optical Multi-Ion Clocks

As proposed in Herschbach et. al. [27] one aim of the experiment discussed in this work is to setup a multi-ion clock based on $^{115}\text{In}^+$ ions, which are sympathetically cooled by $^{172}\text{Yb}^+$ ions. This section describes the constituents that build an optical clock and the terms instability and accuracy that are the figures of merit of all clocks. The main motivation for the proposed setup of a multi-ion clock is to reduce the clock instability. The following subsection introduces and motivates the chosen ion species. A more general and more extensive introduction into frequency standards can be found in the textbook from Riehle [31]. A recent review focussing on optical clocks has been published by Ludlow et. al. [16].

In Fig. 2.1 the setup of an optical clock is shown schematically. A clock is based on counting the number of cycles of a periodic signal. In the case of an optical clock the periodic signal is the electric field of a laser source. The laser frequency is tuned to an atomic resonance which serves as a stable and absolute reference for the frequency. From the subsequent measurements of the atomic resonance an error signal is generated and fed back to the laser frequency. Because of the limited control loop bandwidth that locks the frequency to the atomic resonance, the laser source itself has to provide a sufficiently high short-term stability. To achieve this the laser source is pre-stabilized to a high finesse optical cavity. The pre-stabilized laser source is also referred to as local oscillator. Together with the feedback loop on the atomic resonance it forms a frequency standard. To count the cycles of the laser field a frequency comb [15] is used. The frequency comb transfers the optical frequency with a fixed and known relationship into an rf frequency. The cycles of the rf frequency can be counted by conventional electronics and this allows to measure time intervals with extremely high precision.

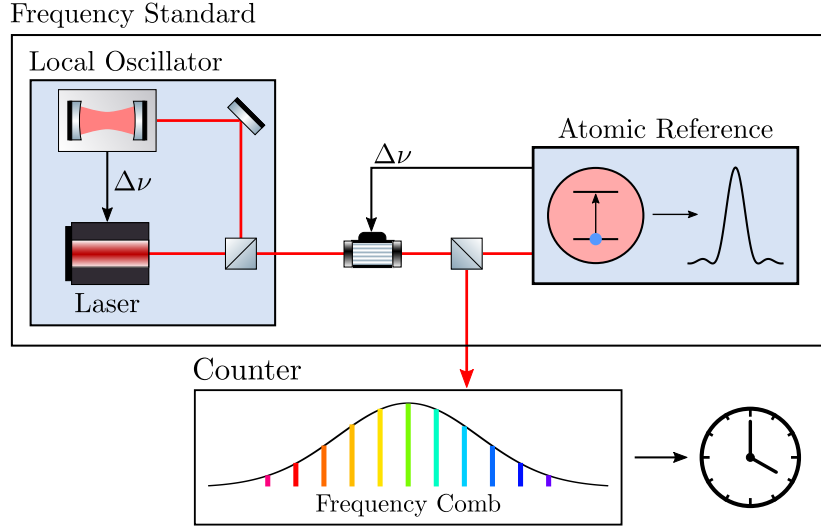


Figure 2.1.: Schematic showing the constituents of an optical clock setup. A laser source that is pre-stabilized to a high finesse optical cavity (local oscillator) is tuned to an atomic resonance. A optical frequency comb is used to transfer the optical frequency to an rf frequency. The frequency comb allows to count the oscillations of the laser field electronically and to generate a clock signal.

The two measures that define the performance of any frequency standard are its frequency instability and the frequency uncertainty. In order to be well defined and comparable, the frequency of the unperturbed atomic resonance must be determined. Any external perturbation has to be measured and corresponding corrections have to be applied. The uncertainties of measuring the perturbations and of the applied corrections have to be summed up and define how accurate the measured frequency corresponds to the unperturbed atomic resonance. Thus the total frequency uncertainty results from the uncertainties of systematic shifts of the atomic frequency. Some of the most important frequency perturbations are discussed in Sec. 2.5.

The frequency instability on the other side describes the statistical error of the frequency measurement. It defines how often or how long the atomic resonance has to be probed to average down to a certain frequency resolution. This statistical error is typically described by the so-called Allan variance [32]

$$\sigma_y^2(\tau) = \frac{1}{2} \langle [\bar{y}_2(\tau) - \bar{y}_1(\tau)]^2 \rangle. \quad (2.1)$$

Here $\bar{y}_{1,2}(\tau)$ are the average frequencies of two subsequent frequency measurements with averaging time τ . The angle brackets denote the mean value for many of such subsequent frequency measurements with the same averaging time τ . Thus the Allan variance gives the mean square deviation between two frequency measurements with averaging time τ . The square root of the Allan variance σ_y^2 is commonly referred to as Allan deviation σ_y .

For optical clocks the achievable instability is fundamentally limited by the so-called quantum projection noise (QPN) [33]. It is caused by the interrogation scheme, which projects each ion either to the ground or excited state. The resulting Allan deviation caused by the QPN for N_{ions} independent ions is given by

$$\sigma_y(\tau) = \frac{\Delta\nu}{\nu_0} \frac{1}{\kappa\sqrt{N_{\text{ions}}}} \sqrt{\frac{t_c}{\tau}}, \quad (2.2)$$

where $\Delta\nu$ is the observed full width at half-maximum (FWHM) of the atomic resonance, τ is the total measurement time, $t_c = \tau/N_{\text{cycles}}$ is the time period of a single interrogation and κ is a numerical factor of the order unity, which depends on the details of the used interrogation scheme.

For single ion clocks that are targeting fractional frequency uncertainties in the range of a few 1×10^{-18} the QPN is a severe limitation. In Huntemann et. al. [8] a record low systematic frequency uncertainty of 3.2×10^{-18} is reported for a $^{171}\text{Yb}^+$ single ion clock. However the reported instability of $5 \times 10^{-15}/\sqrt{\tau}$ requires a measurement time $\tau(N_{\text{ions}}=1) = 2.44 \times 10^6 \text{ s} = 28.3 \text{ d}$ to reach an identical statistical error. Such long averaging periods are technically challenging, because it requires a very reliable experimental setup without any downtimes. It also prevents observing frequency perturbations that oscillate at shorter time scales.

To reduce the QPN basically two methods can be found from Eq. 2.2. The first method is to reduce the observed linewidth $\Delta\nu$. In fact as long as the linewidth is Fourier-limited an increased cycle time t_c is favourable, because the linewidth decreases $\Delta\nu \propto 1/t_c$. This overcomes the effect of the direct dependency of Eq. 2.2 on the cycle time $\sigma_y \propto \sqrt{t_c}$. For clock ion species with very long living excited states, such as $^{27}\text{Al}^+$ or the octupole transition in $^{171}\text{Yb}^+$, the probe time is limited by the stability of the clock laser. Even the most stable lasers limit the interrogation time t_c to a few seconds because of the limited coherence time. For $^{115}\text{In}^+$ ions a reasonable cycle time t_c is limited by the finite excited state lifetime $t_{\text{in}} = 1/\Gamma = 194 \text{ ms}$. A longer cycle time will lead to a decreased contrast of the probe signal. It has been shown numerically by Peik et. al. [34] that the optimal cycle time for Rabi excitation is $t_{c,\text{Rabi}} = 1.88 \Gamma = 365 \text{ ms}$ and for Ramsey excitation it is $t_{c,\text{Ramsey}} = 1.0 \Gamma = 194 \text{ ms}$. Therefore with the current laser technology [35–37] the clock laser stability is considered not to be critical for an $^{115}\text{In}^+$ clock.

The second method to lower the instability due to QPN is to increase the number of interrogated ions. This is the main motivation for building a multi-ion clock. Although the instability is only reducing by $\frac{1}{\sqrt{N_{\text{ions}}}}$ the measurement time to reach a fixed statistical error is inversely proportional to the ion number N_{ion} . Assuming a single ion instability of $7 \times 10^{-16}/\sqrt{\tau}$, which is a realistic assumption for $^{115}\text{In}^+$, the averaging time to reach a statistical error of 1×10^{-18} is 5.7 d for a single ion, 13.6 h for 10 ions and could be reduced to 1.4 h for 100 ions.

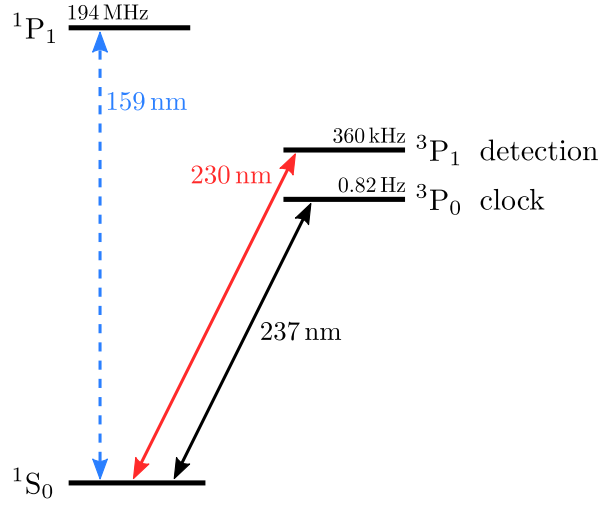


Figure 2.2.: Reduced $^{115}\text{In}^+$ ($I=9/2$) term scheme showing the wavelength and decay rates of the clock and the detection transition. The hyperfine structure splitting is not shown for simplicity.

2.1.1. $^{115}\text{In}^+$ Clock Ion Properties

There are a number of reasons for the selection of $^{115}\text{In}^+$ as clock ion species. More details of the mentioned properties of $^{115}\text{In}^+$ ions for precision spectroscopy are explained in the other sections of this chapter.

The $^{115}\text{In}^+$ ion has already been considered as clock ion in a number of experiments [38–40] and thus provides a well known system. In Fig. 2.2 a reduced term scheme of $^{115}\text{In}^+$ is shown. The hyperfine structure resulting from the nuclear dipole moment $I=9/2$ is omitted for simplicity. It is a two-electron system which provides a narrow clock transition $^1S_0 \leftrightarrow ^3P_0$ at 237 nm with a natural linewidth of 0.82 Hz. The transition of this intercombination line is only possible due to admixtures of the short-lived 1P_1 and 3P_1 states [41, 42]. Otherwise $J=0 \leftrightarrow J'=0$ transitions are forbidden for all multipole orders. Besides this long-lived clock state, $^{115}\text{In}^+$ provides a second intercombination line $^1S_0 \leftrightarrow ^3P_1$ which due to its reasonably high decay rate $\Gamma = 360$ kHz is usable for a direct detection of the clock state population via the electron-shelving technique [43, 44]. This transition can also be used for Doppler cooling (see Sec. 2.3), but only provides a reduced cooling rate compared to the usually used dipole allowed transitions. The dipole allowed transition $^1S_0 \leftrightarrow ^3P_1$ at 159 nm is in the vacuum-UV range, which makes it technically challenging to build a coherent light source at this wavelength.

When several ions are trapped in the same ion trap as proposed here, the electric field gradients will influence the clock transition frequency due to the coupling to quadrupole moments Θ (see Sec. 2.5) of participating states. For the clock transition in $^{115}\text{In}^+$ the quadrupole moments are vanishing in first order, which makes it an ideal candidate for a multi-ion clock. Furthermore it provides a low sensitivity to external perturbations

by electric [45] and magnetic [46] fields. Due to its high mass it is also less sensitive to motional frequency shifts, such as the time dilation shift.

In Herschbach et. al. [27] it is proposed to simultaneously trap $^{172}\text{Yb}^+$ ions together with the clock $^{115}\text{In}^+$ ions. $^{172}\text{Yb}^+$ provides a dipole allowed Doppler cooling transition with a natural linewidth of 19.6 MHz (see Sec. 4.3). Due to its favourable mass ratio the $^{172}\text{Yb}^+$ ions can be used for an efficient sympathetic cooling of the $^{115}\text{In}^+$ ions [47]. This cooling scheme would also allow to cool the ions during clock interrogation with a reduced light shift compared to a direct cooling of the $^{115}\text{In}^+$ ions. The $^{172}\text{Yb}^+$ ions have no hyperfine structure due to the vanishing nuclear dipole moment. This facilitates the Doppler cooling scheme. $^{172}\text{Yb}^+$ also offers two narrow clock transitions, which can be used to characterize different frequency shifts with a higher resolution than on the $^{115}\text{In}^+$ ions due to a higher sensitivity to some perturbations (e.g. electric and magnetic fields). Furthermore the fluorescence of the Doppler cooling light can be used to detect excess micromotion (see. Sec. 2.2 and Sec. 5.3). In fact all measurements presented in this thesis have been carried out exclusively with $^{172}\text{Yb}^+$ ions.

2.2. Linear Paul Traps

This section gives an introduction into the theory of Paul traps and explains why a linear Paul trap design is favourable for clock interrogation on a linear ion Coulomb crystal. More comprehensive descriptions of ion traps can be found in several text books like [48, 49]. According to Earnshaw's theorem it is not possible to create a static electric potential that confines a charged particle in all three dimensions. For a three-dimensional harmonic potential

$$\varphi(x, y, z) = \frac{U_{\text{dc}}}{2} (c_x x^2 + c_y y^2 + c_z z^2) , \quad (2.3)$$

this can be proven by inserting the potential φ into the Laplace-Equation $\Delta\varphi = 0$, restricting the parameters c_i to fulfil the equation $c_x + c_y + c_z = 0$. At least one of the three parameters has to be negative and the potential $\varphi(x, y, z)$ is repulsive in this direction. To achieve three-dimensional confinement of a charged particle a time dependent potential $\varphi_{\text{rf}}(x, y, z, t)$ has to be added. The total electric potential is then

$$\begin{aligned} \varphi(x, y, z, t) = & \frac{U_{\text{dc}}}{2} (c_x x^2 + c_y y^2 + c_z z^2) \\ & + \frac{U_{\text{rf}}}{2} \cos(\Omega_{\text{rf}} t) (\tilde{c}_x x^2 + \tilde{c}_y y^2 + \tilde{c}_z z^2) . \end{aligned} \quad (2.4)$$

Typical oscillation frequencies Ω_{rf} are within the rf range. Inserting into the Laplace equation again imposes the conditions

$$c_x + c_y + c_z = 0 \quad \text{and} \quad \tilde{c}_x + \tilde{c}_y + \tilde{c}_z = 0 , \quad (2.5)$$

on the parameters c_i and \tilde{c}_i . The parameters are defined by the geometric realization of the trap electrodes and link the electric field at the trap centre to the applied voltages by

$$E_{\text{dc},i} = c_i U_{\text{dc}} \quad \text{and} \quad E_{\text{rf},i} = \tilde{c}_i U_{\text{rf}} \quad \text{with} \quad i \in \{x, y, z\}. \quad (2.6)$$

In a linear Paul trap a chain of ions is trapped on the z -axis. Any rf field $E_{\text{rf},z}$ along this trap axis should vanish. Otherwise this field will cause driven motion at the rf frequency which is referred to as micromotion and is discussed in the following subsection. The motion is unwanted for precision spectroscopy, because it leads to a shift of the resonance frequency and can also be a heating source for the ions. This condition defines the parameters for a linear ion trap to be

$$-(c_x + c_y) = c_z > 0, \quad \tilde{c}_x = -\tilde{c}_y \quad \text{and} \quad \tilde{c}_z = 0. \quad (2.7)$$

The rf field confines the positively charged ions in the xy -plane and vanishes along the z -axis. Confinement along the z -axis is achieved by a static three-dimensional quadrupole potential. Three different electrode geometries, that have been used to realize these trap parameters are shown in Fig. 2.3. Hyperbolic shaped electrodes result in an almost purely harmonic potential over a large trapping region. The drawback of this geometry is the limited optical access for detection and laser beams. This is improved by the rod trap design, which still approximates the rounded electrodes and is easier to manufacture. The chip trap design, which is used for the trap discussed within this work, allows to have a semi-monolithic design, which greatly helps to reduce misalignments of the electrodes to a minimum. Although the electrode shape differs significantly from the hyperbolic trap, close to the trap centre the electric potential is well approximated by Eq. 2.4. Simulations of the trap design presented in this work show that within the range of ± 0.1 mm around the trap centre the maximum relative deviation of the potential from a parabola fit is on the order of 5×10^{-3} . Further deviations from the ideal trap potential of this trap design are discussed in more detail in [30].

2.2.1. Trapping of Single Ions

The equations of motion for a single ion with charge e and mass m are [50]

$$\ddot{x}_i + \frac{e}{m} (U_{\text{dc}} c_i + U_{\text{rf}} \tilde{c}_i \cos(\Omega_{\text{rf}} t)) x_i = 0 \quad \text{with} \quad x_i \in \{x, y, z\}. \quad (2.8)$$

All three equations can be transformed into the standard form of the Mathieu equation

$$\frac{d^2 x_i}{d\xi^2} + (a_i - 2q_i \cos(2\xi)) x_i = 0. \quad (2.9)$$

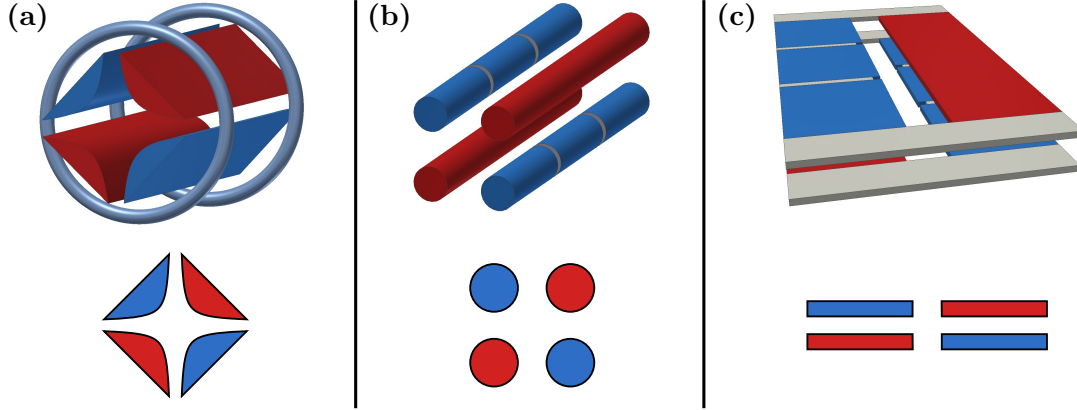


Figure 2.3.: Schematics of different linear trap geometries with 3D illustrations in the top row and electrode cross-sections in the bottom row. Red coloured electrodes illustrate a connection to the rf voltage source. The blue coloured electrodes represent a connection to rf ground and/or a DC voltage source. (a) Trap with hyperbolic electrodes with additional ring electrodes for axial confinement, (b) Rod Trap with segmented dc electrodes, (c) Wafer based trap with segmented dc electrodes.

Therefore the dimensionless parameters

$$a_z = -(a_x + a_y) = \frac{4eU_{\text{dc}}c_z}{m\Omega_{\text{rf}}^2}, \quad (2.10)$$

$$q_x = -q_y = \frac{2eU_{\text{rf}}\tilde{c}_x}{m\Omega_{\text{rf}}^2}, \quad (2.11)$$

$$q_z = 0, \quad (2.12)$$

$$\xi = \frac{\Omega_{\text{rf}}t}{2}, \quad (2.13)$$

are introduced. The relations between the different a- and q-parameters follow directly from Eqs. 2.7. Detailed calculations of the ion trajectories [48, 50] show that confinement is achieved within several regions of stability in the a- and q-parameter space. The trap discussed within this work operates in the lowest region of stability and fulfils the condition $|a_i|, |q_i| \ll 1$. Under this condition the ion trajectory can be approximated by

$$x_i(t) = (x_{0,i} + A_i \cos(\omega_i t + \phi_i)) \left(1 + \frac{q}{2} \cos(\Omega_{\text{rf}} t) \right). \quad (2.14)$$

Here $x_{0,i}$ represents a possible static shift of the ion, which can be caused by static external fields. The ion motion consists of oscillations at the frequency ω_i with amplitude A_i which is referred to as secular motion and a driven motion at the rf frequency Ω_{rf} which is referred to as micromotion. The amplitude of the secular motion A_i is connected to the temperature of the ion, but will be non-zero even if the ion is cooled

to its motional ground state, because of the spread of the wave function. The secular frequency ω_i is for the given conditions well approximated by

$$\omega_i \simeq \frac{\Omega_{\text{rf}}}{2} \sqrt{a_i + \frac{q^2}{2}}. \quad (2.15)$$

With this equation and Eqs. 2.10 - 2.12 the a- and q-parameters can be calculated for a given set of secular frequencies with

$$a_x = \frac{4}{\Omega_{\text{rf}}^2} \omega_x^2 - \frac{q^2}{2} = \frac{2}{\Omega_{\text{rf}}^2} (\omega_x^2 - \omega_y^2 - \omega_z^2), \quad (2.16)$$

$$a_y = \frac{4}{\Omega_{\text{rf}}^2} \omega_y^2 - \frac{q^2}{2} = \frac{2}{\Omega_{\text{rf}}^2} (\omega_y^2 - \omega_x^2 - \omega_z^2), \quad (2.17)$$

$$a_z = \frac{4}{\Omega_{\text{rf}}^2} \omega_z^2, \quad (2.18)$$

$$q = \frac{2}{\Omega_{\text{rf}}} \sqrt{\omega_x^2 + \omega_y^2 + \omega_z^2}. \quad (2.19)$$

Two sources of the micromotion can be identified in Eq. 2.14. First there is micromotion, which originates from a displacement $r_{0,i}$ from the centre of the trap, where the rf fields are not vanishing. This is referred to as excess micromotion (EMM) and can be minimized by shifting the ion to the trap centre using static electric fields. The excess micromotion amplitude can be quantified in various different ways. Within this work the amplitude of the rf field E_{rf} that drives the micromotion is used to quantify micromotion. Conversions to different definitions can be derived if the relevant trap parameters and informations about the considered optical transition are known.

The second source of micromotion is connected to the amplitude A_i of the secular motion. Due to the secular motion the ion oscillates around the trap centre and is therefore periodically exposed to the rf field. Because the secular motion never vanishes entirely, this effect appears in every ion trap and is referred to as intrinsic micromotion (IMM).

Phase shifts between the voltages on the different rf electrodes are another source of micromotion that does not appear in Eq. 2.14. Such phase shifts can be caused by a non equal length of conductors bringing the rf voltage to the different rf trap electrodes. The phase shift $\Delta\varphi$ caused by a length difference Δd for a conductor in vacuum is given by

$$\Delta\varphi = 2\pi \frac{\Delta d}{\lambda_{\text{rf}}} = \frac{\Omega_{\text{rf}} \Delta d}{c}. \quad (2.20)$$

Here λ_{rf} denotes the vacuum wavelength of the rf field and c is the speed of light. The time-dependent voltages on the two rf electrodes with a phase shift $\Delta\varphi$ are

$$U_1(t) = U_0 \cos(\Omega_{\text{rf}}t + \Delta\varphi/2), \quad (2.21)$$

$$U_2(t) = U_0 \cos(\Omega_{\text{rf}}t - \Delta\varphi/2). \quad (2.22)$$

The time dependent voltage difference is

$$\Delta U(t) = U_2(t) - U_1(t) \quad (2.23)$$

$$= U_0 [\cos(\Omega_{\text{rf}}t - \Delta\varphi/2) - \cos(\Omega_{\text{rf}}t + \Delta\varphi/2)] \quad (2.24)$$

$$= \underbrace{2 U_0 \sin(\Delta\varphi/2)}_{U_{0,\varphi}} \sin(\Omega_{\text{rf}}t). \quad (2.25)$$

For typically small phase shifts with $\Delta\varphi/2 \ll 1$ the voltage amplitude $U_{0,\varphi}$ is approximated with $U_{0,\varphi} \simeq U_0 \Delta\varphi$ and the voltage difference $\Delta U(t)$ simplifies to

$$\Delta U(t) = U_0 \Delta\varphi \sin(\Omega_{\text{rf}}t). \quad (2.26)$$

The voltage difference between the two rf electrodes generates an rf field at the position of the ion and drives micromotion. The amplitude of the rf field is determined by the voltage amplitude $U_{0,\varphi}$ and a geometrical factor, which can either be calculated or simulated. Because of the 90° phase shift of this rf field with respect to the trapping rf field it is not possible to compensate this effect by shifting the ion to a location with an increased trapping rf field. A target value for the discussed trap design (see Sec. 3.2) was to have $E_{\text{rf}} \leq 115 \text{ V m}^{-1}$. With FEM simulations (see Sec. 3.3) it is found that 1 V of $U_{0,\varphi}$ results in an rf field of approximately 458 V m^{-1} . Therefore $U_{0,\varphi}$ should be less than 0.25 V. For a trap frequency of 24.38 MHz and for $U_0 = 800 \text{ V}$ this results in a maximum allowed length difference of the rf leads of $\Delta d \leq 0.61 \text{ mm}$.

Luckily the phase-shifted voltage amplitude $U_{0,\varphi}$ is suppressed technically, because the ion trap is part of a resonant circuit and the capacitance of the trap for the differential voltage $\Delta U(t)$ differs from the capacitance for the in-phase rf-voltage. This will lead to different resonance frequencies for both voltage configurations. The trap is driven at the resonance frequency connected to U_{rf} and at this frequency oscillations of $\Delta U(t)$ are suppressed. The attenuation depends on the Q-factor of the resonant circuit and on the difference of the capacitances. While the Q-factor can be measured experimentally it is difficult to directly measure the differences in the trap capacitances for the different voltage configurations, as every electrical probe will have influence on the measured capacitance. Existing voltage differences $\Delta U(t)$ can be detected via micromotion measurements at different ion positions, because of the non-vanishing amplitude and the characteristic phase shift with respect to the rf drive phase.

For many practical considerations micromotion can be completely neglected. This simplifies the further treatment and often gives good approximations, because the micromotion amplitude is a factor $q_i/2$ smaller than the amplitude of the secular motion. If this is done, the secular motion can be approximated by the motion of the ion in the harmonic potential

$$V_{\text{p}}(x, y, z) = \frac{m}{2} (\omega_x^2 x^2 + \omega_y^2 y^2 + \omega_z^2 z^2), \quad (2.27)$$

which is referred to as ponderomotive potential or pseudo-potential. It represents the effect of the trap potential given in Eq. 2.4 when averaged over the time of one rf

period. When all dc potentials are neglected, the ponderomotive potential resulting from the rf field is

$$V_{\text{p,rf}}(x, y, z) = \frac{e^2 |E_{\text{rf}}(x, y, z)|^2}{4m\Omega_{\text{rf}}^2}. \quad (2.28)$$

This shows that the rf trap potential is mass dependent and decreases for higher ion masses m . This is in contrast to the static electric field potential. For linear ion traps this makes clear that the radial trap potential changes for different ion species, while the purely static axial trap potential $V_{\text{ax,dc}}$ is independent of the ion mass. Typically, the trap depth of ion traps is in the range of a few eV. These high values allow trapping of ions at and above room temperature. Also single ions can be stored in the trap for days or weeks without losing them.

If the ion is cooled to sufficiently low temperatures such that its kinetic energy becomes comparable to $\hbar\omega_i$, the quantization of the energy levels has to be taken into account. The system is then well described by a quantum harmonic oscillator with the Hamiltonian

$$\hat{H} = \sum_i \frac{\hat{p}_i^2}{2m} + \frac{1}{2}m\omega_i^2\hat{x}_i^2. \quad (2.29)$$

With the definition of the usual creation and annihilation operators

$$\hat{a}_i^\dagger = \sqrt{\frac{m\omega_i}{2\hbar}} \left(\hat{x}_i - \frac{i\hat{p}_i}{m\omega} \right), \quad (2.30)$$

$$\hat{a}_i = \sqrt{\frac{m\omega_i}{2\hbar}} \left(\hat{x}_i + \frac{i\hat{p}_i}{m\omega} \right), \quad (2.31)$$

the Hamiltonian can be rewritten as

$$\hat{H} = \sum_i \hbar\omega_i \left(\hat{a}_i^\dagger \hat{a}_i + \frac{1}{2} \right). \quad (2.32)$$

This shows that the motional energy is quantized. These motional quanta are referred to as phonons, where adding one phonon is equivalent to adding an energy of $\hbar\omega_i$. It has been shown that a quantization of the ion trajectory is also found if the time dependent potential of Eq. 2.4 is taken into account [51, 52]. These authors also showed that the regions of stability in the a- and q-parameter space that have been found with the classical treatment are also identical to those found in the quantum mechanical treatment.

2.2.2. Linear Ion Coulomb Crystals

Ion traps can be used to trap a larger number of ions simultaneously. For laser-cooled ions the kinetic energy of the individual ions typically becomes small compared to the Coulomb energy and the ions form a crystalline structure. These structures are called

ion Coulomb crystals. Depending on the aspect ratio of the trap potential along the three trap axes the resulting ion crystal will be 1-, 2- or 3-dimensional. Linear ion traps are well suited for forming larger ion crystals, because micromotion vanishes along the axial trap axis. Especially for 1-dimensional linear ion Coulomb crystals, where the ions line up on the axial trap axis, micromotion is reduced to a minimum. This subsection will summarize briefly how a linear chain of ions can be realized within a linear ion trap and how ion motion can be described in terms of a normal mode spectrum.

The total potential for N singly charged ions at positions \vec{x}_n within the ponderomotive potential $V_p(\vec{x}_n)$ is given by

$$V_{\text{tot}} = \sum_{n=1}^N V_{\text{pond}}(\vec{x}_n) + \frac{1}{2} \sum_{\substack{n,m=1 \\ n \neq m}}^N \frac{e^2}{4\pi\epsilon_0 |\vec{x}_n - \vec{x}_m|}. \quad (2.33)$$

At the equilibrium ion positions \vec{x}_n^0 the sum of all forces acting on each ion has to vanish and thus the positions are determined by

$$\left. \frac{\partial V}{\partial x_{ni}} \right|_{x_{ni}^0} = 0, \quad (2.34)$$

where n indicates the ion number and $\vec{x}_n = (x_{n1}, x_{n2}, x_{n3}) \equiv (x_n, y_n, z_n)$. This set of equations has to be solved numerically as soon as there are more than a few ions. Numerical calculations of ion positions for linear ion crystals can be found in [53, 54]. It has been shown that for the generation of 1-dimensional crystals of intermediate size ($N = 3 \dots 2000$) the condition on the aspect ratio of the trap frequencies is approximated well by [54]

$$\frac{\omega_{\text{rad}}}{\omega_{\text{ax}}} > 0.73 N^{0.86}. \quad (2.35)$$

For the further treatment of ion motion within a linear chain of ions the displacements

$$\vec{q}_n(t) = \vec{x}_n(t) - \vec{x}_n^0, \quad (2.36)$$

are introduced, where \vec{x}_n^0 are the equilibrium positions. Assuming a purely harmonic trap potential V_p the ion potential can be approximated by a second-order Taylor expansion around the equilibrium positions and is then given by [53, 55]

$$V \approx \frac{1}{2} \sum_{i=1}^3 \sum_{n,m=1}^N \left[\frac{\partial^2 V}{\partial x_{ni} \partial x_{mi}} \right]_{x_{ni}^0} q_{ni} q_{mi} = \frac{1}{2} \sum_{i=1}^3 \sum_{n,m=1}^N V_{nmi} q_{ni} q_{mi}, \quad (2.37)$$

where the first sum is over the three coordinates. For a linear ion chain the radial coordinates of the equilibrium position are $x_n^0 = y_n^0 = 0$ and the axial coefficients of the sum are given by

$$V_{nmz} = \begin{cases} m\omega_{\text{ax},n}^2 + \frac{e^2}{4\pi\epsilon_0} \sum_{k=1, k \neq n}^N |z_n^0 - z_k^0|^{-3} & \text{for } n = m, \\ -\frac{e^2}{4\pi\epsilon_0} |z_n^0 - z_m^0|^{-3} & \text{for } n \neq m. \end{cases} \quad (2.38)$$

For the the radial coordinates we receive

$$V_{nm\alpha} = \begin{cases} m\omega_{\text{rad},n}^2 - \frac{e^2}{4\pi\epsilon_0} \sum_{k=1, k \neq n}^N |z_n^0 - z_k^0|^{-3} & \text{for } n = m, \\ \frac{e^2}{4\pi\epsilon_0} |z_n^0 - z_m^0|^{-3} & \text{for } n \neq m. \end{cases} \quad (2.39)$$

In contrast to the axial direction, the Coulomb interaction in the radial potential reduces the total potential. This reflects the fact, that a radial excursion of an ion increases the distance to all other ions. The eigenvectors β_i^α with $\alpha = 1 \dots N$ of the matrices V_{nmi} define the normal modes of motion

$$\sum_{m=1}^N V_{nmi} \beta_{mi}^\alpha = \lambda_i^\alpha m_n \beta_{ni}^\alpha. \quad (2.40)$$

The eigenvalues λ_i^α of this equation define the normal mode frequencies with $\omega_i^\alpha = \sqrt{\lambda_i^\alpha}$. For linear ion crystals with identical ions, there is for each coordinate a so-called centre of mass mode (COM mode), where all ions oscillate in phase at the single ion trap frequency. Due to the Coulomb interaction term in Eqs. 2.38 and 2.39 this mode is the lowest frequency mode in the axial direction and the mode with highest frequency for the radial directions.

2.3. Interaction of Laser Light with Trapped Ions

The interactions of laser light with trapped ions provide almost perfect control over all aspects of this quantum mechanical system. Using these interactions as a tool allows to precisely characterize and manipulate all internal and external degrees freedom. Different optical transitions can be employed for a wide range of tasks: e.g. strong dipole transitions allow to detect ions by imaging their fluorescence to a photomultiplier or a CCD camera. Dipole transitions are also used for efficient state detection via the electron shelving technique [44] and for Doppler cooling of ions from above room temperature down to a few mK. Furthermore narrow transitions from the electronic ground state to a metastable excited state can be used for cooling of the ions to the motional ground state by sideband cooling [56] and to measure the mean phonon number (see Sec. 4.4). There are many more possibilities to use the light ion interaction for the characterization of the experiment. This section gives an introduction into the description of the interaction of laser light with a trapped particle and shows how laser light can be used for Doppler and sideband cooling. The description follows the summaries given in [57] and [58].

For a simplified notation the discussion is restricted to one dimension and a purely harmonic trap potential with secular frequency ω_{sec} . The internal states of the ion

shall form an effective two-level system with ground state $|g\rangle$ and excited state $|e\rangle$ with an energy difference of $\hbar\omega_0$. The ion is interacting with a travelling wave single mode laser with the wave vector \vec{k} pointing along the x-axis and with frequency ω_L which is tuned close to the ion transition frequency. The system can then be described by the Hamiltonian

$$\hat{H} = \hat{H}_0 + \hat{H}_i, \quad (2.41)$$

$$\hat{H}_0 = \hbar\omega_{\text{sec}} \left(\hat{a}^\dagger \hat{a} + \frac{1}{2} \right) + \hbar\omega_0 |e\rangle \langle e|, \quad (2.42)$$

$$\hat{H}_i = \frac{1}{2} \hbar\Omega_0 (|e\rangle \langle g| + |g\rangle \langle e|) (e^{i(k\hat{x} - \omega_L t)} + e^{-i(k\hat{x} - \omega_L t)}), \quad (2.43)$$

where \hat{a} is the harmonic oscillator annihilation operator, $k = 2\pi/\lambda_L$ is the wave number of the single mode laser and Ω_0 the free ion Rabi frequency. The Rabi frequency is defined by the coupling strength of the laser-ion interaction and contains all details of the electronic transition. Because of this, equation 2.43 can be used to describe electric-dipole-allowed transitions, electric-quadrupole-allowed transitions, as well as stimulated Raman transitions. Transforming to the interaction picture with $\hat{U} = \exp(-i\hat{H}_0 t/\hbar)$, the interaction Hamiltonian becomes [57]

$$\begin{aligned} \hat{H}_{int} &= \hat{U}_0^\dagger \hat{H}_i \hat{U}_0 \\ &= \frac{1}{2} \hbar\Omega_0 (e^{i\omega_0 t} |e\rangle \langle g| + e^{-i\omega_0 t} |g\rangle \langle e|) \\ &\quad \times e^{i\omega_{\text{sec}} t (\hat{a}^\dagger \hat{a} + \frac{1}{2})} (e^{i(k\hat{x} - \omega_L t)} + e^{-i(k\hat{x} - \omega_L t)}) e^{-i\omega_{\text{sec}} t (\hat{a}^\dagger \hat{a} + \frac{1}{2})} \\ &\approx \frac{1}{2} \hbar\Omega_0 e^{i\omega_{\text{sec}} t (\hat{a}^\dagger \hat{a} + \frac{1}{2})} (e^{i(k\hat{x} - \Delta t)} |e\rangle \langle g| + e^{-i(k\hat{x} - \Delta t)} |g\rangle \langle e|) e^{-i\omega_{\text{sec}} t (\hat{a}^\dagger \hat{a} + \frac{1}{2})}. \end{aligned} \quad (2.44)$$

In the last step the rotating-wave approximation is used to eliminate all terms that are oscillating at $\omega_L + \omega_0 \approx 2\omega_0$. This approximation is valid as long as $\Delta = \omega_L - \omega_0 \ll 2\omega_0$. The matrix element for a transition from the electronic ground state $|g\rangle$ to the excited state $|e\rangle$ with simultaneous change in the motional quantum number for $|n\rangle$ to $|n'\rangle$ is

$$\langle n', e | \hat{H}_{int} | n, g \rangle = \frac{1}{2} \hbar\Omega_0 \langle n' | e^{ik\hat{x}} | n \rangle e^{i[\Delta + (n' - n)\omega_{\text{sec}}]t}. \quad (2.45)$$

The exponential term shows that the transition frequency is shifted by $(n' - n)\omega_{\text{sec}}$ which fulfils energy conservation as the energy is effectively transferred from the electronic transition $|g\rangle \rightarrow |e\rangle$ to the motional transition $|n\rangle \rightarrow |n'\rangle$. The matrix element $\langle n' | e^{ik\hat{x}} | n \rangle$ defines the relative strength of the transition. Because of their importance these transitions have been given special names. Transitions with $n' = n$ are referred to as carrier transitions. Whereas transitions with $n' > n$ are called blue sideband transitions (BSBs) and transitions with $n' < n$ are called red sideband transitions (RSBs). Sideband transitions with $\Delta n = |n - n'| = 1, 2, \dots, n$ are also referred to as first or

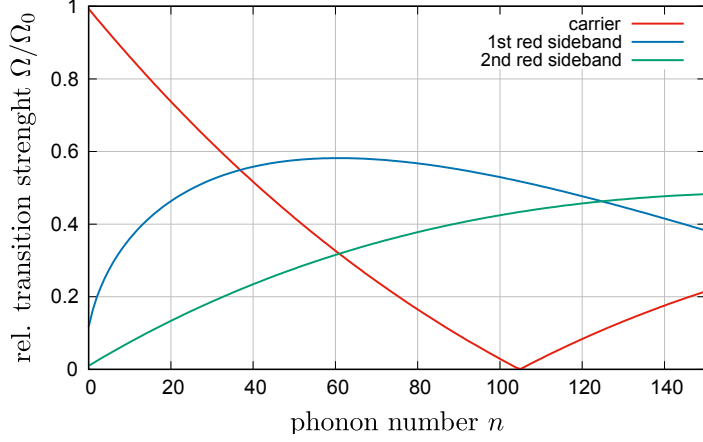


Figure 2.4.: Plot of the relative transition strength Ω/Ω_0 on the carrier, first and second red sideband, where n is the initial motional quantum number. The value of $\eta \approx 0.12$ was calculated for the 411 nm quadrupole transition in $^{172}\text{Yb}^+$ with $\omega_{\text{sec}} = 2\pi \times 500$ kHz.

der, second order, or n -th order transitions. The further discussion is simplified by introducing the Lamb-Dicke parameter [59]

$$\eta = k\sqrt{\frac{\hbar}{2m\omega_{\text{sec}}}} = \frac{2\pi}{\lambda_L}x_0 = \sqrt{\frac{\hbar\omega_r}{\hbar\omega_{\text{sec}}}}. \quad (2.46)$$

It relates x_0 , which is the extension of the motional ground-state wave function along x , to the laser wavelength λ_L . Alternatively, η^2 represents the ratio of the photon recoil energy $\hbar\omega_r$ to the single phonon energy $\hbar\omega_{\text{sec}}$. If in contrast to the initial assumptions there is an angle θ between the wave vector \vec{k} and the considered trap principal axis the Lamb-Dicke parameter reduces by the factor $\cos\theta$. It has been shown that the relative transition strength is [60, 61]

$$\langle n'|e^{ik\hat{x}}|n\rangle = \langle n'|e^{i\eta(\hat{a}+\hat{a}^\dagger)}|n\rangle = e^{-\frac{\eta^2}{2}}\sqrt{\frac{n_{<}!}{(n_{<}+\Delta n)!}}\eta^{\Delta n}L_{n_{<}}^{\Delta n}(\eta^2), \quad (2.47)$$

where $n_{<}$ is the lesser of n and n' and L_n^α are the generalized Laguerre polynomials. From this equation it can be seen that $\langle n'|e^{ik\hat{x}}|n\rangle = \langle n|e^{ik\hat{x}}|n'\rangle$. In Fig. 2.4 the relative transition strengths resulting from Eq. 2.47 are plotted. The equation simplifies in the so-called Lamb-Dicke regime where $\eta^2(2n+1) \ll 1$. This condition allows a Taylor expansion of the exponential

$$e^{i\eta(\hat{a}+\hat{a}^\dagger)} = 1 + i\eta(\hat{a} + \hat{a}^\dagger) + \mathcal{O}(\eta^2). \quad (2.48)$$

This shows that within the Lamb-Dicke regime all transitions with $\Delta n > 1$ can be neglected and transitions on the carrier and the first order sidebands are dominating. Also with respect to the carrier transition Rabi frequency the Rabi frequencies on the first red and blue sideband are suppressed by a factor η . For low motional quantum

numbers n Fig. 2.4 shows the strong suppression of second order sidebands and also that the ratio between first order and carrier transitions strength is corresponding to the Lamb-Dicke parameter. For the experimental parameters used for this plot the condition for the Lamb-Dicke regime is met only for $n \leq 3$.

2.4. Laser Cooling

Within this work two laser cooling techniques are used for the preparation of the ion for further experiments. Doppler cooling [12, 13] cools the ion from initially a few hundred Kelvin to less than 1 mK. Subsequently, resolved sideband cooling allows to cool the ion to the motional ground state which corresponds to a temperature of approximately 12 μ K. This section describes briefly the theoretical fundamentals of both cooling techniques. More elaborated reviews of laser cooling techniques can be found in [57, 61–63].

2.4.1. Doppler Cooling

The principle of Doppler cooling relies on the Doppler shift of a moving ion which leads to a velocity dependent radiation pressure. For properly chosen experimental parameters the radiation pressure results in a net cooling of the ion. For the further description the ion is considered to form a two-level system with transition frequency ω_0 and decay rate of the excited state Γ . It is irradiated by a travelling wave laser beam with frequency ω_L . For simplicity we reduce the problem to one dimension such that wave vector \vec{k} is either parallel or antiparallel to the ion velocity \vec{v} . Also, we neglect the effect of micromotion and consider the ion to be trapped in a static harmonic potential. If $\Gamma \gg \omega_{\text{sec}}$ a single absorption and spontaneous emission cycle is much shorter than the oscillation period of the ion in the trap potential and hence the velocity change between absorption and emission can be neglected. With every photon absorption the momentum $\hbar k$ is transferred to the atom. The subsequent spontaneous emission of photons is generally isotropic such that on average no momentum is transferred. Therefore the average radiation force is

$$\vec{F}_{\text{rad}} = \hbar k \Gamma \rho_{ee} = \hbar k \Gamma \frac{s/2}{1 + s + (2(\Delta - k \cdot v)/\Gamma)^2}. \quad (2.49)$$

Here ρ_{ee} is the probability to be in the excited state and $s = 2|\Omega_0|^2/\Gamma^2$ is the saturation parameter. The radiation force is maximized when $\Delta - k \cdot v = 0$. Then the laser detuning exactly cancels out the Doppler shift. For a red detuned laser $\Delta < 0$ the radiation force increases if the ion moves towards the ion¹. In this case the scattering of photons reduces the ion velocity and its temperature. On the other hand scattering

¹as long as $|kv| < |\Delta|$

a photon will be more unlikely when the ion moves away from the laser beam because the effective detuning from the resonance increases. These scattering events would lead to a heating of the ion in the trap. In summary the whole scheme will result in an effective cooling of the ion in the trap as long as the laser is red-detuned.

For an ion in a 3D harmonic potential a single red detuned laser beam is sufficient to provide cooling in all three dimensions as long as the beam has projections onto all three principal axis of the trap potential. Here the oscillating movement of the ion will also make sure that a projection of the wave vector \vec{k} is antiparallel to the ion, which is required to cool the ion.

The Doppler temperature T_D is the lowest temperature that can be achieved with Doppler cooling. For the ideal detuning of $\Delta = -\Gamma/2$ it is given by

$$k_B T_D = \frac{\hbar\Gamma}{2}. \quad (2.50)$$

The temperature is then limited by the recoil of the spontaneously emitted photons, which cause a Brownian motion in velocity space.

For the experimental realization of Doppler cooling typically a dipole transition with a decay rate of at least a few tens of MHz is used. This allows to have a high photon scattering rate and a fast cooling of the ions from above room temperature to a few mK. As the decay rate Γ also determines the Doppler temperature there is a trade-off between minimum temperature and efficient cooling. Besides the efficient cooling a large photon scattering rate helps to detect scattered light with a camera or a photomultiplier tube. The decay rate Γ is typically much larger than the secular frequency ω_{sec} and therefore the individual motional sidebands of the transition are not resolved.

Micromotion can have significant influence on the Doppler cooling efficiency, because of micromotion sidebands in the absorption spectrum at $\omega_0 \pm \Omega_{rf}$ in first order. So a laser with a detuning $|\Delta| < \Omega_{rf}$ is blue detuned to this sideband and this will lead to a heating of the ion. Such effects can be avoided by carefully reducing micromotion to a minimum.

2.4.2. Resolved Sideband Cooling

In order to be able to cool the ion to the motional ground state Doppler cooling is usually not sufficient. Cooling to the motional ground state is often advantageous or necessary for subsequent experiments. In this work it was implemented to determine the heating of the ion in the trap. The first experimental realization of ground state cooling of a trapped particle [56] used the resolved sideband cooling method. The first description of this method is found in [13]. Since then the resolved sideband cooling technique has become a standard method for cooling of strongly bound ions.

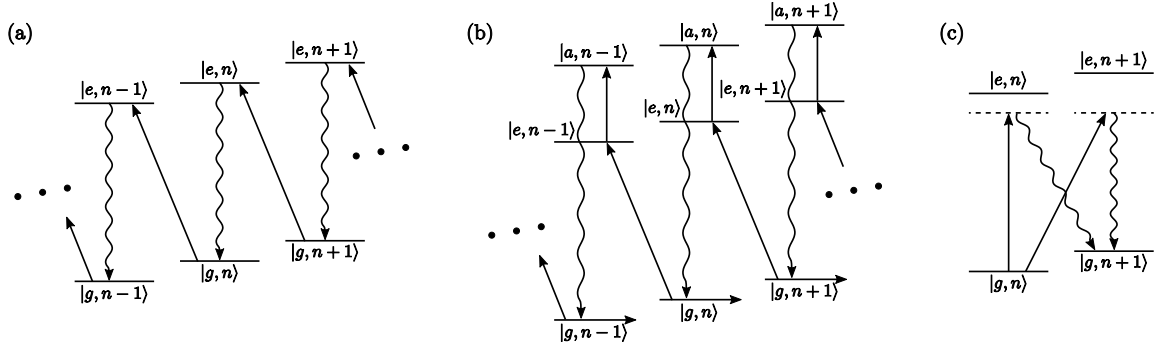


Figure 2.5.: Term schemes showing the fundamental principles of resolved sideband cooling. (a) Cooling on the first red sideband with subsequent spontaneous emission on the carrier. (b) The lifetime of the excited state can be artificially reduced by the excitation to a short-lived auxiliary state. (c) Illustration of the two dominant heating processes during sideband cooling.

For the implementation of the sideband cooling technique the linewidth Γ of the atomic transition has to be smaller than the trap frequency ω_{sec} . This conditions allows to resolve the individual motional sidebands and to explicitly address them by tuning of the laser to a specific sideband resonance.

In Fig. 2.5 (a) the basic principle of the sideband cooling technique is illustrated. A travelling wave laser is tuned to the first red sideband and excites the ion from ground state $|g\rangle$ to the excited state $|e\rangle$. At the same time the motional quantum number is reduced. In the Lamb-Dicke regime the subsequently emitted photon does not effect the motional state. Even outside the Lamb-Dicke regime on average the emitted photon does not change the motional quantum number. In total every cycle of absorption and spontaneous emission takes out a motional quantum and the ion is cooled until it reaches its motional ground state. The whole scheme also works for higher order red sidebands, but as shown in the Sec. 2.3 in the Lamb-Dicke regime close to the ground state the excitation on higher order sidebands is strongly suppressed.

Compared to Doppler cooling the cooling rate of sideband cooling is reduced because the Rabi frequencies on the narrow transition are lower and thus the excitation of the ion takes longer. As shown in Fig. 2.4 the Rabi frequency on the red sideband also depends on the motional quantum number n . Therefore also the cooling rate depends on n and is continuously changing during the cooling period. Also the subsequent spontaneous emission is taking longer, because of the longer lifetime of the excited state. A long excited state lifetime can even prevent achieving an efficient cooling rate. This problem can be overcome by using a short lived auxiliary state $|a\rangle$ as depicted in Fig. 2.5 (b). In this scheme after each excitation to the excited state another laser that is tuned to the transition $|e\rangle \rightarrow |a\rangle$ excites the ion to the auxiliary state and from there it rapidly decays to the ground state. Effectively this process shortens the lifetime of the excited state and thus increases the cooling rate.

There are two options to implement the addition of the auxiliary state. The first option is referred to as pulsed sideband cooling. Here a π -pulse on the sideband transition is followed by a pulse on an auxiliary transition that brings the ion back to the ground state. Both pulses are repeated until the ion is cooled to the motional ground state. The advantage of this implementation is that the sideband transition linewidth and frequency is not affected by the auxiliary transition. The disadvantage is that it is more complicated to implement. Also, as the red sideband Rabi frequency depends on the motional quantum number n , the π -pulse can only be approximated.

The second option is to excite both transitions simultaneously and this is referred to as continuous sideband cooling. As shown in [64] this approach allows to adiabatically eliminate the auxiliary state $|a\rangle$ and results in an effective two-level system with a dressed excited state $|e'\rangle$ and a tunable decay rate Γ' . The decay rate is given by

$$\Gamma' = \frac{\Omega_a^2}{(\Gamma_{a \rightarrow g} + \Gamma_{a \rightarrow e})^2 + 4\Delta_a^2} \Gamma_{a \rightarrow g}. \quad (2.51)$$

Here Ω_a and Δ_a are the Rabi frequency and detuning of the transition $|e\rangle \rightarrow |a\rangle$. $\Gamma_{a \rightarrow g}$ is the decay rate of the auxiliary state $|a\rangle$ to the ground state $|g\rangle$ and $\Gamma_{a \rightarrow e}$ is the decay rate of the auxiliary state $|a\rangle$ to the excited state $|e\rangle$. The effective detuning of the coupling to the dressed state is given by

$$\Delta' = \Delta_e - \Delta_a \frac{\Omega_a^2}{(\Gamma_{a \rightarrow g} + \Gamma_{a \rightarrow e})^2 + 4\Delta_a^2}, \quad (2.52)$$

where Δ_e is the detuning for the sideband transition. If both transitions are driven on resonance the dressed state is also driven on resonance. The advantage of this method is that only one long sideband cooling pulse is needed to cool the ion to the ground state. It also allows to adjust the cooling rate and the finally achievable mean phonon number \bar{n} by the tuning of Γ' . The disadvantage of this technique is that for the tuning of Γ' the intensity and the frequency of the auxiliary laser has to be controlled precisely.

The lowest achievable mean phonon number after resolved sideband cooling is approximately given by [61, 63]

$$\bar{n} \approx \frac{\Gamma^2}{\omega_{\text{sec}}^2}. \quad (2.53)$$

Here Γ is the decay rate of the excited state $|e\rangle$. The two dominant heating processes during sideband cooling are shown in Fig. 2.5 (c). The first heating process consists of off-resonant excitation on the carrier transition with subsequent decay on the blue sideband. The second possible heating process consists of off-resonant excitation on the blue sideband followed by a decay on the carrier transition. The probability for both heating processes depend on the effective linewidth of the transition to the excited state. The linewidth can be limited by the decay rate of the excited state, by the pulse duration of the laser pulse (Fourier-limited linewidth), or by the laser linewidth.

2.5. Systematic Clock Frequency Shifts

This section gives a short overview over the most dominant sources of systematic frequency shifts for trapped ion frequency standards and clocks. For the determination of the unperturbed transition frequency those shifts need to be measured and corresponding corrections need to be applied. The uncertainties of the determination of those corrections have to be characterized and contribute to the overall frequency uncertainty. A more detailed description of different sources of frequency shifts can be found in [16].

This work is focussed on the development of an ion trap which produces low systematic shifts and uncertainties. Therefore, the discussion first focuses on frequency shifts related to the ion trap. The only two experiments [8, 9] of trapped ion frequency measurements which reported fractional uncertainties in the range of 1×10^{-18} show that major contributions to the frequency uncertainties are trap related. Therefore, a suitable ion trap design that lowers those uncertainties is necessary to further reduce the frequency uncertainty.

2.5.1. Motional Frequency Shifts

In ion traps there are several motional frequency shifts that need to be distinguished. The first order Doppler shift, which is proportional to the average velocity $\langle v \rangle$, is suppressed because the trapped ion does not move with respect to the laser source. Here and in the following discussion the angled brackets shall denote an average over the probe pulse duration. Because the linewidth of the probe transition is much smaller than the secular frequency ω_{sec} and the trap drive frequency Ω_{rf} , both motions will result in resolved sidebands and the first order Doppler shift on the corresponding carrier transition is negligible. However both motions lead to a relativistic time dilation shift

$$\frac{\Delta\nu}{\nu_0} = -\frac{\langle v^2 \rangle}{2c^2} = -\frac{\langle E_{\text{kin}} \rangle}{mc^2}, \quad (2.54)$$

that is proportional to the mean of the squared velocity $\langle v^2 \rangle$ or the mean kinetic energy $\langle E_{\text{kin}} \rangle$. This shift is also known as second-order Doppler shift. As seen in Eq. 2.54 the shift does not depend on the chosen atomic transition, but only on the speed and the mass of the ion. In general a heavier ion will have a smaller second-order Doppler shift.

Shifts due to Excess Micromotion

To derive the average kinetic energy of excess micromotion the ion trajectory of Eq. 2.14 is used and the excess micromotion is separated from the thermal secular motion. For

simplicity the description is restricted to a single radial trap axis. The micromotion trajectory and velocity profile is given by

$$x_{\text{emm}}(t) = x_0 \frac{q}{2} \cos(\Omega_{\text{rf}} t), \quad (2.55)$$

$$v_{\text{emm}}(t) = -x_0 \frac{q \Omega_{\text{rf}}}{2} \sin(\Omega_{\text{rf}} t). \quad (2.56)$$

Here x_0 is the displacement of the ion from the axial trap axis and $v_{\text{emm}}(t)$ is the velocity of the ion due to micromotion. The time average of the kinetic energy over a oscillation cycle is then given by

$$\begin{aligned} \langle E_{\text{kin,emm}} \rangle &= \frac{1}{2} m \langle v_{\text{emm}}^2 \rangle \\ &= \frac{1}{16} m x_0^2 q^2 \Omega_{\text{rf}}^2. \end{aligned} \quad (2.57)$$

To receive the second order Doppler shift as a function of the rf field E_{rf} instead of the displacement x_0 , Eqs. 2.27 and 2.28 are equated and solved for x_0^2

$$\begin{aligned} x_0^2 &= \frac{e^2 |E_{\text{rf}}|^2}{2 m^2 \omega_{\text{sec}}^2 \Omega_{\text{rf}}^2} \\ &= \frac{4e^2 |E_{\text{rf}}|^2}{m^2 q^2 \Omega_{\text{rf}}^4}. \end{aligned} \quad (2.58)$$

In the last step it was assumed that the influence of the dc voltages on the radial potential can be neglected ($|a_i| \ll q_i^2$). With this assumption, Eq. 2.15 simplifies to $\omega_{\text{sec}} = \frac{q \Omega_{\text{rf}}}{2\sqrt{2}}$. The resulting second-order Doppler shift caused by excess micromotion as a function of E_{rf} is given by [65]

$$\frac{\Delta\nu}{\nu_0} = - \left(\frac{e |E_{\text{rf}}|}{2mc \Omega_{\text{rf}}} \right)^2. \quad (2.59)$$

At an rf amplitude of 100 V m^{-1} at $\Omega_{\text{rf}} = 2\pi \times 24.38 \text{ MHz}$ the micromotion Doppler shift for an $^{115}\text{In}^+$ ion is -8.3×10^{-19} . One of the targets of this work was to develop an ion tap that keeps this shift below 1×10^{-18} for a sufficiently large region on the trap axis. As already discussed in Sec. 2.2.1 phase shifts between the rf voltages on different trap electrodes can also cause second-order Doppler shifts. To estimate those shifts Eq. 2.26 can be used to derive the resulting rf field, which is then inserted into Eq. 2.59.

Shifts due to Secular Motion and Ion Heating Rates

The energy of the secular motion per trap axis is given by $\frac{1}{2} k_{\text{B}} T$. In addition the energy of the intrinsic micromotion also depends on the secular motion amplitude as

discussed in Sec. 2.2.1. Under the condition that in the radial directions the axial trapping has negligible influence on the radial trap frequency $|a_i| \ll q_i^2$, the average energy of the intrinsic micromotion equals the energy of the secular motion [65]. With this and under the consideration that movement along the trap axis does not produce intrinsic micromotion, the total second-order Doppler shift due to secular motion and intrinsic micromotion is given by

$$\frac{\Delta\nu}{\nu_0} = -\frac{5}{2} \frac{k_B T}{mc^2}. \quad (2.60)$$

The equation above assumes that the ion temperature is identical for all three trapping axes. This is not necessarily the case. For the characterization of this shift each temperature needs to be measured with high accuracy. The fractional frequency shift of $^{115}\text{In}^+$ ions that are sympathetically cooled to the $^{172}\text{Yb}^+$ Doppler temperature of 0.5 mK is $\frac{\Delta\nu}{\nu_0} = -1 \times 10^{-18}$.

At a first glance the ion temperature does not depend on the ion trap characteristics. This is only true as long as the external heating rate of the ions in the trap is sufficiently low. If this is not the case, either the temperature increases significantly during the probe pulse or it is even necessary to constantly cool the ions. A constant temperature increase will lead to an increased temperature uncertainty and an increased uncertainty of the second-order Doppler shift. When the ions need to be cooled constantly, the cooling light will lead to ac-Stark shifts. The ion heating is caused by fluctuating voltages on the trap electrodes, which produce fluctuating electric fields that increase the secular motion amplitude. There are a number of possible sources for the fluctuation of potentials on trap electrodes [66]. There is also not a single dominant source and also the combination of dominant sources for the fluctuating potentials differ between different experiments. Typically, the magnitude of the heating rate is measured by observing the increase of the mean phonon number $\dot{\bar{n}}$ per time unit. For radial modes such an increase will result in an subsequent temporal increase of the second-order Doppler shift of

$$\frac{\partial}{\partial t} \left(\frac{\Delta\nu}{\nu_0} \right) = -\frac{\dot{\bar{n}} \hbar \omega_{\text{sec}}}{mc^2}. \quad (2.61)$$

For axial modes the shift is a factor 2 lower, because there ideally is no intrinsic micromotion in axial direction. For $^{115}\text{In}^+$ ions trapped at a trap frequency of 500 kHz the addition of one phonon adds a shift of -1.9×10^{-20} .

2.5.2. Frequency Shifts due to Electromagnetic Fields

External electromagnetic fields are another source of major frequency shifts that are observed in current single ion optical clock experiments [8, 9]. Stark shifts are caused by electric fields which can be static or ac fields. Different sources of these electric fields have to be distinguished. Zeeman shifts are caused by static or fluctuating magnetic fields.

Black-body Radiation Shift

Due to the ac Stark effect, the electric field of the black-body radiation emitted by the environment of the ion shifts the energy levels of the clock transition by a significant amount. For $^{115}\text{In}^+$ all dipole allowed transitions originating from one of the clock energy levels have a significantly shorter wavelength than the peak wavelength of the black body radiation spectrum at room temperature $\lambda_{\text{BBR}, 300\text{K}} = 9.7\ \mu\text{m}$. In this case the BBR shift is well described by a static approximation [67] and is proportional to the differential static scalar polarizability $\Delta\alpha_s$ of the two clock levels. The black-body radiation shift can then be calculated with

$$\Delta\nu_{\text{BBR}} = -\frac{1}{2h}\langle E^2(T)\rangle \Delta\alpha_s (1 + \eta). \quad (2.62)$$

Here $\langle E^2(T)\rangle = (831.9\ \text{V m}^{-1})^2 [T(\text{K})/300]^4$ is the mean-squared electric field, h is the Planck constant and η is a dynamic correction factor, which accounts for deviations from the static approximation. The most accurate values of the differential static scalar polarizability $\Delta\alpha_{s,\text{In}}$ and the dynamic correction η_{In} of $^{115}\text{In}^+$ result from theoretical calculations [45] and are

$$\Delta\alpha_{s,\text{In}} = (3.3 \pm 0.3) \times 10^{-41}\ \text{Jm}^2/\text{V}^2, \quad (2.63)$$

$$\eta_{\text{In}} < 1 \times 10^{-4}. \quad (2.64)$$

With these numbers the total frequency shift $\Delta\nu_{\text{BBR}}$ and the fractional frequency shift $\Delta\nu_{\text{BBR}}/\nu_0$ at $T = 293.15\ \text{K}$ for $^{115}\text{In}^+$ are

$$\Delta\nu_{\text{BBR}} = -17\ \text{mHz}, \quad (2.65)$$

$$\frac{\Delta\nu_{\text{BBR}}}{\nu_0} = -1.25 \times 10^{-17}. \quad (2.66)$$

In order to reduce the fractional uncertainty of the shift to 1×10^{-19} we have to calculate or measure this effect with a relative accuracy of 1%. At this level the dynamic correction factor can be neglected without loss of accuracy.

From Eq. 2.62 two contributions to the uncertainty of the black-body radiation shift can be identified. Those are the uncertainty in the differential static scalar polarizability $\Delta\alpha_s$ on the one hand and the uncertainty of the effective temperature T at the position of the ion on the other hand. The latter determines the magnitude of the mean-squared electric field $\langle E^2(T)\rangle$. Using the given uncertainty of the theoretical value of the polarizability $\Delta\alpha_{s,\text{In}}$ (see Eq. 2.63) the fractional uncertainty of the black-body radiation shift is $\Delta\nu_{\text{BBR}}/\nu_0 = 1.1 \times 10^{-18}$. To further reduce this uncertainty and to verify the theoretical calculations, the polarizability $\Delta\alpha_{s,\text{In}}$ has to be measured with higher precision. This can be done by the observation of IR laser-induced light shifts. For a known light intensity and beam waist the polarizability can be derived from Eq. 2.62. The uncertainty of the temperature is related to the ion trap design as the ion trap is heating up due to different heating effects discussed in Sec. 3.4 and Sec. 5.1. An uncertainty in the effective temperature at the position of the $^{115}\text{In}^+$ ion of 1 K will lead to a fractional frequency uncertainty of 1.8×10^{-19} .

Stark Shifts induced by Trap RF Field

Besides the motional shifts, the trap rf field E_{rf} also causes a Stark shift. There are two different sources of this shift. The rf field that causes excess micromotion and the rf field that the ion is exposed to due to the secular motion, which also causes intrinsic micromotion. The resulting Stark shift is given by

$$\frac{\Delta\nu}{\nu_0} = -\frac{1}{2h\nu_0}\Delta\alpha_s\langle E_{\text{rf}}^2\rangle. \quad (2.67)$$

$\langle E_{\text{rf}}^2\rangle$ is the time averaged squared rf field amplitude that it is seen by the ion and it is given by [65]

$$\langle E_{\text{rf}}^2\rangle \approx \frac{m\Omega_{\text{rf}}^2 k_{\text{B}}T}{e^2} + \frac{|E_{\text{rf,emmm}}|^2}{2}. \quad (2.68)$$

The first term in the equation results from the secular motion and the second term originates from excess micromotion. For the equation it is again assumed that the influence of the dc trap fields on the radial trapping frequency can be neglected ($|a_i| \ll q_i^2$).

For $^{115}\text{In}^+$ at a temperature of 0.5 mK the shift due to intrinsic micromotion at a trap drive frequency $\Omega_{\text{rf}} = 2\pi \times 24.38$ MHz is -2.4×10^{-20} . The shift resulting from an EMM rf field of $E_{\text{rf,emmm}} = 100$ V m $^{-1}$ causes a shift of -9.8×10^{-20} . Compared to other shifts discussed so far both values are negligible and are therefore not taken into account in this work.

2.5.3. Other Frequency Shifts

There are various other sources for frequency shifts, that are not discussed in detail within this work. Here the shifts that are particularly important for a multi-ion clock are briefly introduced.

Quadrupole Shift

The electric quadrupole shift results from the interaction of static electric field gradients with the electric quadrupole moments of the clock states. The Hamiltonian describing this interaction is [68]

$$H_{E2} = \nabla E^{(2)}\Theta^{(2)}. \quad (2.69)$$

Here $\nabla E^{(2)}$ is the symmetric traceless second-rank tensor that describes the electric field gradient at the position of the ion. $\Theta^{(2)}$ is the electric quadrupole moment tensor of the ions. Within ion trap static electric fields are usually well compensated, because they are easily detected by micromotion measurements. However, field gradients at the ion position are not easily detected and can have a significant magnitude. For

linear ion traps that are proposed here for multi-ion optical clocks an electric field gradient is needed to provide axial confinement. The magnitude of this gradient can be obtained by a measurement of the axial trap frequency. Additionally, in a multi-ion trap there are field gradients due to the electric fields of the neighbouring ions. These field gradients are significant and therefore clock states should be selected that do not have a quadrupole moment in first order. This is the case for the $^{115}\text{In}^+$ clock states 1S_0 and 3P_0 , because of the rotational symmetry ($J = 0$) of both clock states. Higher order calculations [69] show that the excited state has a small non-vanishing quadrupole moment due to state mixing with the 3P_1 and 1P_1 states. Because of this, the quadrupole shift cannot be neglected and has to be characterized. A more detailed description of quadrupole shifts can be found in [68]. Several techniques have been proposed that lead to a cancellation of the quadrupole shift.

Zeeman Shift

The Zeeman shift results from the interaction of external magnetic fields with the magnetic moments of the clock states. For $^{115}\text{In}^+$ ions the first-order Zeeman sensitivity is small compared to other clock species, because the total electronic angular momentum vanishes and only the much smaller nuclear spin ($I = 9/2$) contributes to the first order Zeeman shift. First-order Zeeman shifts are typically cancelled out by an alternated probing of Zeeman sublevels that are symmetrically shifted. For a multi-ion clock, besides temporal fluctuations of the magnetic field, also spacial gradients have to be sufficiently small.

In addition to the first-order shift also the second-order Zeeman shift has to be characterized. The frequency shift is given by $\Delta\nu = c_2 \langle B^2 \rangle$ and is proportional to the time-averaged squared magnetic field $\langle B^2 \rangle$. With $c_2 = 4.1 \text{ Hz/mT}^2$ the clock transition in $^{115}\text{In}^+$ ions offers a low sensitivity to this shift [16, 27]. Typically it is expected that the alternating trap currents have the largest contribution to $\langle B^2 \rangle$. Low trap drive currents and large ion-electrode distances help to reduce the resulting magnetic fields.

Effect of Ion Mode Structure

As discussed in Sec. 2.3 the Rabi frequency of the clock transition depends on the motional quantum number n . For an ion string of N ions that are interacting with the clock laser there will be N normal modes per trap axis. In Eq. 2.40 the eigenvector β_i^α shows how each normal mode can be decomposed in relative motion amplitudes of the individual ions. In general, each individual ion contributes to all normal modes. Unless all normal modes are cooled to the ground state with high probability, a thermal Boltzmann distribution is expected for all normal mode quantum numbers. Hence the Rabi frequency Ω_i of ion i will fluctuate from experiment to experiment. Furthermore,

the uncertainty of the Rabi frequency $\sigma_{\Omega,i}$ will be different for each ion position i . In total those effects will effectively lead to an increased clock instability. The effect becomes more important for a larger number of ions and for higher ion densities. For a two-species ion crystal this effect also depends on the position of the clock ions. Further details of how the ion mode structure influences the effective transition strengths can be found in [70].

3. Ion Trap Development

The main target of the trap development process was to build a trap that is optimized for precision spectroscopy on linear ion Coulomb crystals. This chapter highlights the most important steps of the development process. The first section describes the different goals of the trap development and briefly discusses how they can be achieved. Then the design of the trap electrodes, which is based on the proposal of Herschbach et al. [27], is introduced. The electrode geometry is optimized for minimal axial rf fields. It is shown how the trap geometry and imperfections of it are influencing the axial rf fields. Based on finite element method (FEM) calculations of the electric fields, tolerances for the geometry of the trap are defined. This is followed by a section about the thermal management and the choice of materials. The next section then focusses on the trap fabrication process. All process steps from the bare AlN wafer to the finished trap are discussed in detail. The chapter finishes with a section about the measurements of the achieved trap geometry, which are compared to the given target values.

3.1. Main Targets of the Trap Development Process

This section explains which objectives have been pursued in order to optimize the ion trap for precision spectroscopy on linear ion Coulomb crystals. For each objective it is briefly discussed why it is important and how it was addressed in the trap development.

Excess micromotion

As discussed in Sec. 2.2 micromotion is a driven motion at the trap drive frequency Ω_{rf} . It appears if the rf field at the position of the ion is not vanishing. Micromotion changes the atomic transition frequency due to the 2nd-order Doppler shift and due to the dc Stark shift (see Sec. 2.5). In an ideal linear ion trap there are no axial rf fields and the radial rf fields vanish completely at the nodal line in the centre of the trap. Nevertheless there are several reasons for non-vanishing rf fields that need to be distinguished and are discussed in detail in Sec. 2.2 and 3.3. Trap related effects are phase shifts between different rf electrodes and axial rf fields that are induced by the design or an imperfect geometry of the trap electrodes. Phase shifts can be avoided by a careful adjustment of the length of the different rf leads. Axial rf fields are minimized by an optimized

design (see Sec. 3.2) and by reducing alignment and manufacturing errors to a minimum (see Sec. 3.5 and 3.6). The design target was to achieve a fractional 2nd-order Doppler shift below 10^{-18} for $^{115}\text{In}^+$ ions. For the trap parameters in this work this corresponds to an rf field amplitude of $E_{\text{rf}} < 110 \text{ V m}^{-1}$.

Temperature of the ion trap

The black-body radiation of the environment of the ion shifts the atomic transitions due to the Stark effect as described in Sec. 2.5. As the trap covers a large fraction of the solid angle seen by the ions, the temperature of the trap needs to be known precisely in order to account for the resulting frequency shift. The application of the rf voltage heats up the ion trap due to resistive and dielectric losses (see Sec. 3.4). The temperature rise was minimized by choosing materials with minimal dielectric losses and high heat conductivities. Furthermore the trap temperature was measured by calibrated Pt100 sensors directly attached to the trap and by imaging the trap with an IR camera (see Sec. 5.1 and appendix A.4).

External heating rates

As discussed in Sec. 2.5.1 the thermal secular motion leads to a second-order Doppler shift. Therefore, the temperature of the ions needs to be known with low uncertainties. External electric fields fluctuating at one of the secular frequencies of the ions lead to an increasing ion temperature and a larger frequency shift and uncertainty. This effect can limit the duration of the spectroscopy pulse or even make it necessary to constantly cool the ions during the spectroscopy pulse. This is unwanted, because of the resulting ac Stark shifts due to the cooling light. There are various effects that contribute to the heating rate [66] and there is not a single dominant effect. Observed ion trap heating rates spread over several orders of magnitude even for similar experimental parameters. Because of the complexity of this topic the reason for the wide range of measured heating rates is currently not fully understood. The influence of noise on the trap electrodes can be limited by an increased ion-electrode distance d . Different theories predict the heating rate to scale with $d^{-\beta}$ with $\beta = 2$ to 4. For the presented design the effect of external heating rates was limited by choosing a rather large ion-electrode distance of $\approx 0.71 \text{ mm}$. Furthermore all dc electrodes have a low-pass filter with a cut-off frequency of $\approx 100 \text{ Hz}$ directly soldered onto the trap chips. Additionally, technical voltage noise on the trap electrodes is suppressed by a high Q-factor of the rf drive resonant circuit and a low noise dc voltage supply as introduced in Sec. 4.2.

Stable trapping of ions and ion Coulomb crystals

It has been shown theoretically [71, 72] and experimentally [73–75] that deviations from the perfect quadrupole potential lead to additional unstable regions within the region of stability. These additional instabilities become more prominent for large values of the q -parameter. In order to achieve stable trapping of single ions and ion Coulomb crystals it is therefore useful to minimize the deviation from the quadrupole potential and to operate the trap at a low q -parameter. For the

trap design presented here, the deviation from the quadrupole potential has been discussed in the thesis of Karsten Pyka [30]. It was shown that close to the trap centre, the contribution of higher order terms to the trap potential is small or negligible. In addition, the trap is operated at a low q -parameter of $q \approx 0.055$.

Segmentation and scalability

One central goal of the development of the trap design was to increase the number of ions used for spectroscopy in order to reduce the averaging time to achieve a given frequency accuracy. At the same time the uncertainty of the transition frequency must be kept as low as possible for all probed ions. The maximum meaningful number of ions within a single linear ion Coulomb crystal can be limited by various effects (e.g. micromotion and ratio of radial and axial trap frequencies). To be able to overcome this limit a segmented trap design was chosen. This gives the possibility to simultaneously trap and probe ion chains in every other trap segment. The trap design realized in this work has eight trap segments and two long end segments. Hence up to four ion Coulomb crystals can be trapped at the same time. The segmentation of the ion trap also allows to scale up the number of segments and hence the number of ions in future versions of the trap design. Segmented traps are also needed for quantum simulation and for quantum computing experiments. For these experiments it is desirable to be able to transport quantum information from one point to another by shuttling ions between the different segments. The segmentation of the ion trap also allows to tailor the axial trap potential and have influence on the shape of the axial trap potential.

Non-magnetic materials

Transition frequencies of ions are influenced by Zeeman shifts as discussed in Sec. 2.5.3. Thus the magnetic field at the position of the ions needs to be measured with high accuracy in order to subtract these shifts. Nevertheless fluctuations of the magnetic field that appear on timescales shorter than the time needed for one measurement cannot be accounted for and lead to an increased frequency uncertainty. To reduce magnetic field fluctuations only non-magnetic materials were used to built the ion trap.

3.2. Ion Trap Geometry

The focus of this section is to introduce the geometry of the trap and all important dimensions. The design is based on the proposal of Herschbach et al. [27] and has been successfully tested with a prototype trap based on a glass-reinforced thermoset laminate (Rogers 4350B™) by Pyka et al. [29, 30].

The geometry of the trap electrodes is illustrated in the drawings of Fig. 3.1. The trap consists of four layers of planar electrodes, which are labelled from bottom to top

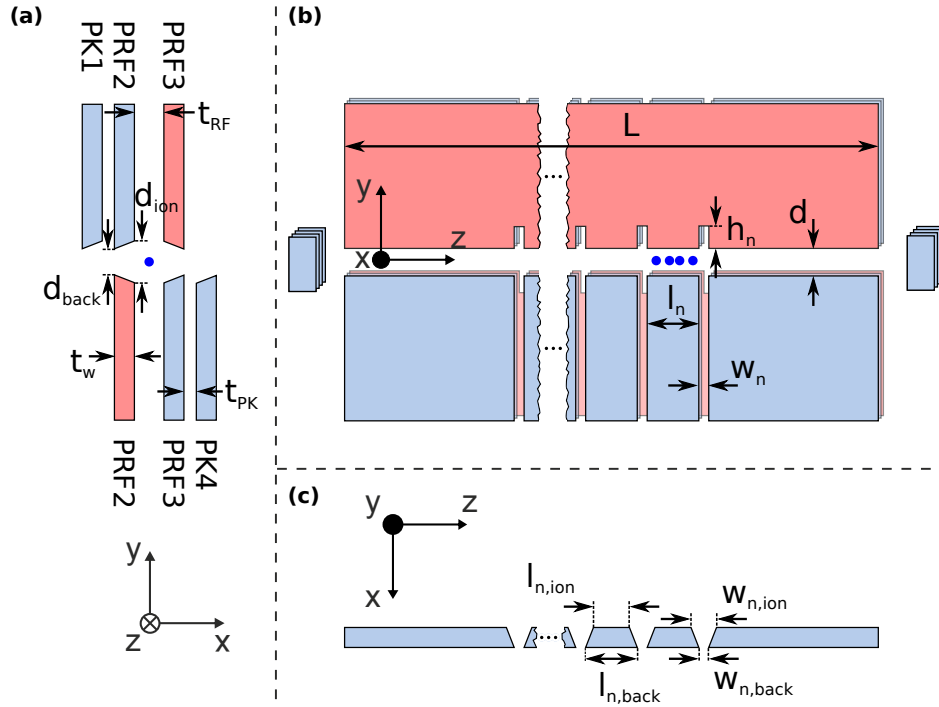


Figure 3.1.: Drawings of the trap electrodes, which show all important geometric dimensions and the chosen orientation of the coordinate system. The depicted dimensions are discussed in the main text. Electrodes which are connected to the rf voltage are coloured in red. The light blue dc electrodes are all connected to rf ground via capacitors. (a) In the side view the four layers of electrodes are visible. The position of the ions is indicated by the dark blue dot. (b) The top view of the ion trap shows the segmentation of the dc and of the rf electrodes. Grounded end electrodes on both sides of the central trap slit are used to avoid having dielectric material in the line of sight of the ions (dark blue dots). (c) The front view on a set of dc electrodes illustrates the chamfered geometry of the individual electrodes which is resulting from the laser cutting process.

PK1, PRF2, PRF3 and PK4 (see also Fig. 3.2). Because of the manufacturing process, the edges of the electrodes are chamfered. Therefore, the dimensions on different sides of the same electrode differ. The side which is facing the ion is referred to as ion side and the other side is defined as backside. The four electrodes of the two inner PRF layers form the typical geometry of a linear ion trap (see Fig. 2.3) and provide confinement in the radial plane. The rf voltage is applied only to two electrodes and all other electrodes are grounded via capacitors. This asymmetric voltage configuration has the benefit that dc voltages only have to be applied to rf grounded electrodes. This avoids the use of capacitors to feed the rf voltage to the electrodes. The capacitors would heat up and introduce phase shifts, because of tolerances in capacity [30]. Axial confinement in a certain trap segment is achieved by applying positive dc voltages to the dc electrodes of the neighbouring segments. Each trap segment has four dc electrodes. They can be used to shift the ions in the radial plane, to influence the orientation of the radial principal axes and to change the radial trap frequencies. The

parameter	design value	description
L	29 mm	Length of the trap
$d, d_{\text{back}}, d_{\text{ion}}$	1 mm	Width of the trap slit
t_{RF}	1 mm	Separation of PRF layers thick spacer thickness
t_{PK}	0.127 mm	Separation between PRF and PK layer, thin spacer thickness
t_{w}	0.380 mm	Electrode thickness, thickness of trap wafer
$l_{\text{n}}, l_{\text{n,back}}, l_{\text{n,ion}}$	1 mm, 2 mm	Length of the n th trap segments
$w_{\text{n}}, w_{\text{n,back}}, w_{\text{n,ion}}$	0.1 mm	Width of the n th notch between trap segments
h_{n}	0.5 mm	Height of the n th notch in the rf electrode

Table 3.1.: Design values and description of the most important trap dimensions. All dimensions are also shown in the schematic drawing of Fig. 3.1. The subscript "ion" is used for dimensions on the ion side and the subscript "back" is used for dimensions on the backside of the electrode.

coordinate system is chosen such that the z -axis is parallel to the axial trap axis. The y -axis is parallel to the electrode planes and the x -axis is perpendicular to them.

All important trap dimensions are depicted in Fig. 3.1 and the design values for those dimensions are given in Tab. 3.1. There are various reasons for choosing these design values and most of them have been discussed already in [27, 29, 30] in detail. The length of the trap L has to be large enough to reduce its effect on the axial micromotion and the length of 29 mm is a safe choice for that. The width of the trap slit d and the separation between the two PRF layers t_{RF} define the distance between electrodes and ions. It is approximately 0.707 mm. This is chosen as a compromise between achievable trap frequencies at a given rf voltage amplitude and the unwanted external heating rate. Both values increase when the distances are reduced. For the separation between PRF and PK layers t_{PK} a small value was chosen to increase the solid angle that is available for the detection optics. The thickness of the AlN wafer t_{w} is a compromise between access for detection and handling limitations. Thinner wafers do easily break during the manufacturing process. The length of the trap segments l_{n} was chosen to be 1 mm in order to maximize axial trap frequencies. Also, this allows to have more segments compared to the prototype trap. One segment was kept at a length of 2 mm, because this length was proven to work well with the prototype trap. The notches which separate the different segments have a strong influence on the amount of axial micromotion. Smaller notches lead to lower axial micromotion amplitudes. The value of 100 μm was chosen due to manufacturing limitations.

The exploded view of Fig. 3.2 shows that the trap consists out of four micro-structured AlN wafer with outer dimensions of 50 mm \times 50 mm and a thickness of 0.38 mm. As described in Sec. 3.5, laser cutting was used for the cut-outs of the AlN wafer.

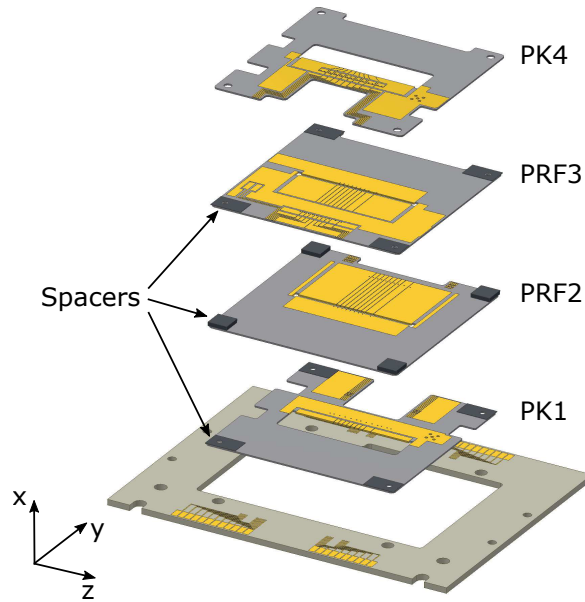


Figure 3.2.: Exploded drawing of the ion trap. The image shows the four trap wafer labelled PK1, PRF2, PRF3 and PK4. The support board at the bottom is used to mount the trap and for the electrical connection of the dc and rf voltages. PK1 is directly glued onto the support board. Spacers placed at the corners of the trap chips (depicted in dark grey) separate the other trap chips in x-direction.

Compared to Fig. 3.1 each wafer realizes one layer of electrodes. The electrodes are formed by a gold coating of approximately $4\ \mu\text{m}$ thickness. The separation of the electrodes along the x-axis is achieved by placing four AlN spacers at the edges of the wafer. The four wafers are glued onto a support board also made out of AlN. The support board is used for mechanical mounting of the trap inside the vacuum chamber and for the electrical connections of all electrodes.

Fig. 3.3 shows the backside and the ion side of a PRF3 wafer. The trap segments are numbered from 1 to 8 starting with the larger 2 mm long segment. The larger end segments are also numbered. End segment 1 is next to segment 1. End segment 2 is on the opposite side. For the rf voltage connection, 5 mm wide copper stripes are soldered to the shown solder pads on the left and the right side of the backside. The dc voltages and the Pt100 sensor are connected through bond wires to the bonding pads at the bottom of the backside. Vias are used to guide the dc voltages from the backside to the ion side of the wafer. The drawings also show the positions of the surface-mount device (SMD) resistors, capacitors and of the Pt100 temperature sensor. The resistors and capacitors are used to form a low-pass filter for the applied dc voltages. Next to the Pt100 sensor, two capacitors are placed in parallel that short all ac voltages. This prevents a heating of the sensor due to rf currents. All SMD's are soldered to the gold electrodes with lead-free solder¹.

¹Kester EM907, alloy Sn96.5Ag3Cu0.5, “no-clean” flux

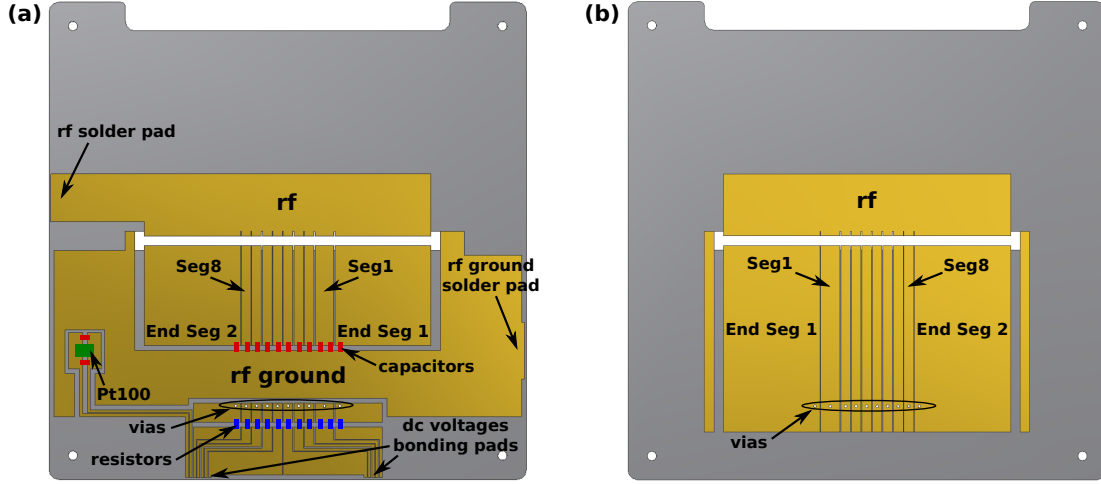


Figure 3.3.: Drawings of the PRF3 wafer which show the labelling of the different trap segments. (a) Backside of the wafer with SMD resistors (blue), capacitors (red) and Pt100 sensor (green). There are two solder pads for the connection of the rf and rf ground and 12 bonding pads for the dc voltages and for the temperature sensor readout. For each dc electrode there is a via with 300 μm diameter connecting the electrodes on the ion side to the backside. (b) Ion side of the PRF3 wafer. The electrode geometry is identical to the ion side of the PRF2 wafer.

3.3. Calculations of the Electric Fields of the Trap

The optimization of the trap geometry and the definition of tolerances for the trap fabrication was achieved by FEM calculations of the trap potential [27, 29, 30]. The objective was to minimize the amplitude of axial rf fields on the trap axis in order to keep the 2nd-order Doppler shift due to axial micromotion as low as possible. The section starts with general remarks that help to understand the relation between geometry and axial rf field. The main part shows examples of how the trap geometry influences the axial rf field. FEM calculations have also been used to realize a trap potential simulator. The goal of the simulator was to predict the strength and orientation of the three-dimensional trap potential for any combination of rf and dc voltages.

The reason for the non-vanishing axial rf field is that the trap geometry breaks a number of symmetries. For a perfectly symmetric, perfectly machined and perfectly aligned trap the axial rf field would vanish. In the trap geometry presented in the previous section the following symmetries are broken.

Translational symmetry in z-direction

The trap has a finite length. The effect of the finite length has been analysed in [27]. It has been shown that a length of 30 mm is sufficient to have a central region of more than 10 mm with an axial rf field $E_{\text{rf},z} < 110 \text{ V m}^{-1}$.

Voltage configuration

The rf voltage is only applied asymmetrically to two electrodes while the other

electrodes are grounded. The asymmetric voltage configuration is chosen deliberately. It facilitates the application of dc voltages to the individual trap segments. For a symmetric rf voltage configuration it would also be more difficult to guide two rf lines to the trap electrodes without having phase shifts (see. Sec. 2.2.1).

Rotational symmetry

The design of stacked layers and the additional PK layers break the rotational symmetry around the z-axis.

Segmentation

In contrast to the rf electrodes the dc electrodes have electrically separated segments.

Geometry imperfections

The real trap will have manufacturing and alignment errors.

In the following the effects of the segmentation and of the geometry imperfections are discussed. Those are the only two effects that can be influenced during design and manufacturing without a fundamental change of the trap design.

For the calculation of the axial rf field it is sufficient to solve a static problem. If phase shifts are neglected only the time instant where the rf voltage is at its maximum is of interest. A simplified two-dimensional picture of the trap as shown in Fig. 3.4 is useful to get a better understanding for the electric fields. Instead of field lines it is often easier to think of equipotential lines. Close to the electrodes those equipotential lines have to be parallel to the electrode surface. This makes it relatively simple to estimate the course of the equipotential lines. The electric field lines are perpendicular to the equipotential lines. Therefore, if the equipotential line is not parallel to the trap axis, there is an axial component of the rf field. The axial trap axis should ideally coincide with an equipotential line, because if an equipotential line crosses the trap axis, the rf field on the trap axis does have an axial component. If a flat rectangular rf electrode and segmented dc electrodes are chosen (see Fig. 3.4 (a)), the equipotential lines will bend into the notches that separate the dc electrodes. Only very close to the rf electrode we will have a straight equipotential line and low axial rf fields. If such notches are also added to the rf electrodes (see Fig. 3.4 (b)), the equipotential lines will bend also into those notches. Both effects will cancel each other out at the centre of the trap. Because of the remaining asymmetry the effects do not cancel out perfectly and there will still be a small amount of axial micromotion. In addition, with this picture it can be realized that the width w_n and the height h_n of the notches can influence the strength of the effect and thus influence the magnitude of the residual axial rf fields.

All FEM calculations presented in this work were carried out with the commercially available software COMSOL Multiphysics 4.1. The geometry of the trap model has been implemented with the integrated model builder. The design values of the trap dimensions of Tab. 3.1 have been adjusted by small corrections of less than 20 μm in

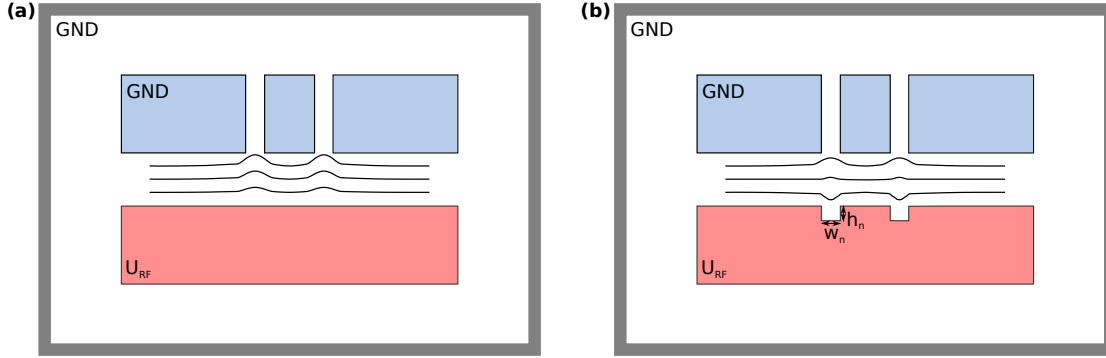


Figure 3.4.: Simplified two-dimensional sketches of the ion trap with equipotential lines at the trap centre. The grey box depicts the grounded vacuum chamber. (a) Equipotential lines for an ion trap with a flat rf electrode. (b) Equipotential lines for an ion trap with an rf electrode that includes notches. The width w_n and the height h_n of these notches influence the deformation of the equipotential lines. Hence these two dimensions can be used to minimize axial rf fields.

order to match to the measured trap dimension (see Sec. 3.6). This has been done in order to use the FEM results for a trap potential simulator that can be used to simulate the trap potential for a given set of rf and dc voltages. The simulator program is described at the end of this section. The exact geometry values that were used for the simulation are listed in the appendix section A.1. Because of the limited computation power the geometry has been simplified slightly. Besides small deviations it resembles the geometry depicted in Fig. 3.1. All dielectric materials such as the AlN material have been left out. The effect of the chamfered electrode edges has not been modelled. All electrodes are cuboids. The vacuum chamber was replaced by a grounded box with a minimum distance to the electrodes of 20 mm. It has been checked that a further increase of this distance does not change the calculated fields and potentials close to the trap axis. Finally the number of segments has been reduced to three 1 mm wide segments and a single 2 mm wide segment. This was necessary to be able to perform the simulations with the available computing power. Nevertheless compared to the FEM calculations in [27, 29, 30] the modelled geometry is closer to reality. In contrast to those simulations, a single rf electrode with notches as shown in Fig. 3.1 (b) was used and also the PK electrodes are included in all calculations. All electrode surfaces have been set to a defined potential and the resulting electric field has been simulated. The integrated meshing routine has been used to create mesh points with tetrahedral shape. Different regions have been defined to be able to get a finer mesh at the centre of the trap. The finest mesh was generated on the trap axis where the distance between the meshing points was chosen to be 20 μm . The total number of mesh points was on the order of a few million.

The results of the FEM calculations have been used to define manufacturing tolerances for the trap geometry. As an example of how this was achieved, the influence of a deviation Δw of the notch width w on all rf electrodes is discussed in the following. Therefore, the axial rf field $E_{\text{rf},z}$ has been simulated for different values of Δw . The

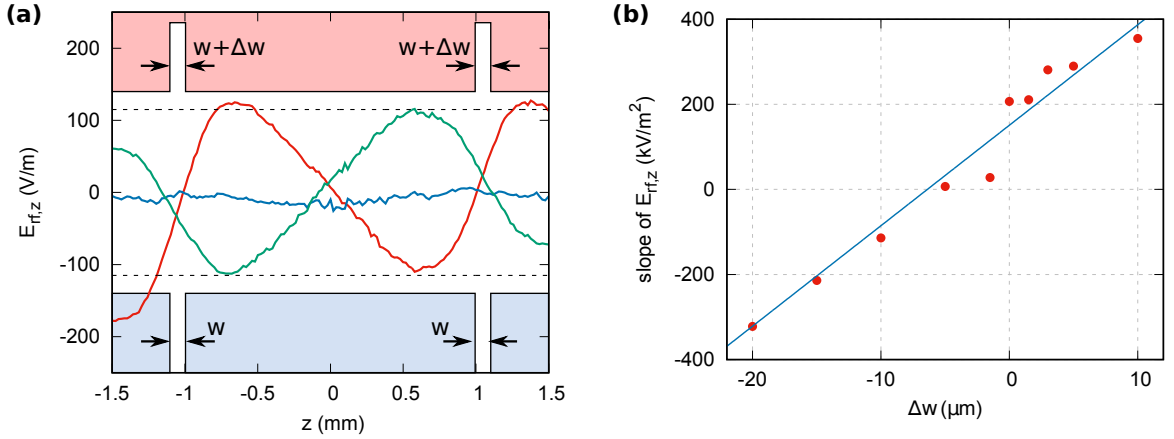


Figure 3.5.: FEM calculation of the axial rf field $E_{\text{rf},z}$ for an applied voltage of 1 kV. The width of all notches on the two rf electrodes has been varied by Δw . (a) Plot of the axial rf field $E_{\text{rf},z}$ along the trap axis for values Δw of $-15 \mu\text{m}$ (red), $-5 \mu\text{m}$ (blue) and $0 \mu\text{m}$ (green). The dashed lines indicate the electric field magnitude that corresponds to a 2nd-order Doppler shift of 1×10^{-18} for $^{115}\text{In}^+$. The electrodes at the top and bottom indicate the position of the central trap segments. (b) Fit results for the slope of $E_{\text{rf},z}$ at $z = 0 \text{ mm}$ for different values of Δw . The fit errors are smaller than the dot size. The error of the FEM calculation is expected to be the dominating error source, but it is difficult to estimate the size of this error. It is expected to be of equal size for all calculations. The blue line is the result of a linear fit to the data points. The slope vanishes and changes its sign at $\Delta w \approx -6 \mu\text{m}$.

results are shown in Fig. 3.5. In the two graphs it can be seen that the field vanishes for $\Delta w \approx -6 \mu\text{m}$ and increases quickly if the deviation differs from the optimum value by only a few μm . The fact that the field does not vanish at $\Delta w = 0 \mu\text{m}$ but at a negative value shows that the effect of the notches on the rf electrodes is slightly stronger than the effect of the separated dc electrodes. For a variation of the height h of the slits on the rf electrodes, similar results have been obtained. There is an optimum height at which the axial rf field almost vanishes and for deviations in both directions it increases with a different sign. However, the sensitivity on the height h is approximately a factor 10 lower than the sensitivity on the width w .

In similar simulations different errors in the trap geometry have been simulated in [27]. The results obtained show, that besides the discussed error of the notch width Δw , there are two further critical geometry errors. Those two errors are illustrated in Fig. 3.6 and are alignment errors between the two PRF layers of the trap. First of all, any tilt angle α between the two PRF layers will introduce a constant offset in the axial rf field [27]. As depicted, α is a rotation around the z -axis, but the same effect appears for a rotation of the upper layer around the y -axis. These two rotations lead to a reduced parallelism of the electrode edges. The second critical misalignment error is a shift Δz of the upper layer along the x -axis. This error has a high sensitivity, because it influences the counteracting effects of the notches on rf and dc electrodes. The misalignment along the y -axis, Δy , only has a weak influence on the axial rf

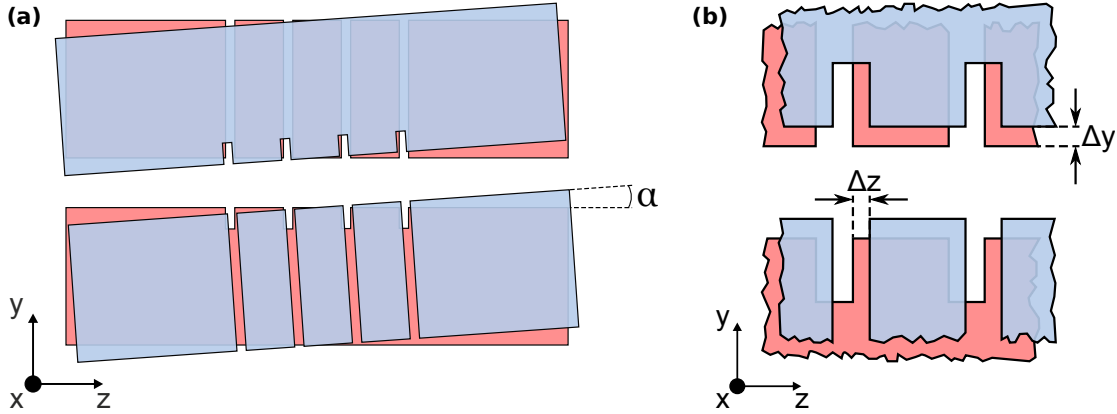


Figure 3.6.: Illustration of critical alignment errors between lower lying (coloured orange) and upper wafer (coloured blue). (a) tilt angle α : the upper wafer is rotated around the x -axis. (b) displacements Δz and Δy : the upper wafer is displaced in z - and y -direction.

field. From the simulation results, the tolerances listed in Tab. 3.2 have been deduced. The target values are chosen to reach a fractional frequency shift caused by axial micromotion of less than 1×10^{-18} . The target values can only serve as an estimate, because they are results of a simplified model. Because of the complex geometry it is not sensible to model all possible deviations. E.g., the effect of combinations of the mentioned critical deviations or the effect of a possible waviness of the electrode edges has not been investigated.

The FEM calculations have also been used to program a trap potential calculator as described in detail in the appendix A.5. The calculator is a Matlab program that takes the rf amplitude and a set of dc voltages as input and calculates the 3D trap potential and the resulting secular frequencies. For the calculator, the electric potential that result from applying 1 V to each single dc electrode has been calculated. The resulting dc electric potentials and the rf field amplitude on the trap axis and on xy -planes lying in the centre of each trap segment have been exported. Within the Matlab script those values have been used to derive the total potential that results from the application of a set of rf and dc voltages. The resulting total potential is then analysed in order to obtain the three trap frequencies, the orientation of the principal axes and the

parameter	target value
α	0.14 mrad
Δz	10 μm
Δw	3 μm

Table 3.2.: Target values for the most critical geometry deviations causing axial rf fields. The values are chosen such that the resulting axial rf field is below 115 V m^{-1} for an rf voltage amplitude of 1 kV. For the used trap drive frequency of 24.38 MHz this corresponds to a second order Doppler shift of 1×10^{-18} for $^{115}\text{In}^+$.

location of the potential minimum. All results are visualized graphically. From the axial potential graph also the axial trap depth can be evaluated. The trap potential simulator is described in more detail in the appendix A.5.

3.4. Thermal Management and Choice of Materials

This section discusses the choice of materials used to built the trap. Besides several other aspects the main focus was to minimize the increase of the trap temperature due to the applied rf voltage. The section starts with an introduction of the different effects that influence the temperature of the trap. Details of how to design an ion trap with optimized thermal management have been published in [76].

The uncertainty of the temperature of the ion trap has a major contribution to the uncertainty of the BBR shift (see Sec. 2.5.2) and therefore the trap temperature has to be known precisely. Two Pt100 temperature sensors have been placed on the PRF wafers to be able to monitor the trap temperature during operation. However, the temperature sensors do not give a full picture of the temperature gradients across the whole trap and the effective temperature seen by the ions. In order to reduce the uncertainty of the spatial temperature distribution on the ion trap it is helpful to keep the temperature of the trap as close as possible to the temperature of the vacuum chamber. This decreases temperature gradients and the uncertainty in the effective temperature seen by the ions.

The steady state temperature of the trap is determined by the amount of heat that is introduced by the application of the rf voltage and by the removal of the heat via heat conduction and radiation. The two sources of heat generation are resistive heating in conductors and rf absorption in insulators. All these effects depend on material parameters.

For a known electric current I , the resistive heating P_{res} can be calculated from the geometry of the conductor and the effective electrical resistivity ρ of the conductor material

$$P_{\text{res}} = RI^2 = \rho \frac{l}{A} I^2. \quad (3.1)$$

Here l is the length of the conductor, A is its cross-sectional area and ρ is the electrical resistivity of the conductor material. As ion traps are operated at high frequencies, it has to be considered that the skin effect can significantly increase the effective resistivity and the resistive heating. To reduce the consequences of the skin effect it is useful to increase the surface of the conductor. For the connection of the rf voltage from the helical resonator to the ion trap, a 100 μm thick copper foil was used and the trap chips have been coated with a 4–5 μm thick gold layer. Both materials offer a high conductivity and the usage of a metal sheet increases the surface compared to round wire. The thickness of the gold layer was limited by the production process (see Sec. 3.5). Because the gold layer thickness is below the skin depth of 15 μm

at 24.38 MHz, the skin effect does only have a minor effect on the resistivity of the gold layer. Another method to reduce resistive heating is to minimize the current $I \propto U_{\text{rf}} \Omega_{\text{rf}} C$, where C is the trap capacitance. A reduction of the trap voltage U_{rf} also reduces the radial trap frequencies ω_{sec} and increases the Lamb-Dicke parameter (see Eq. 2.46), which puts a limit on how far the voltage can be reduced. According to Eq. 2.28 a reduction of the trap drive frequency Ω_{rf} increases the secular frequency ω_{sec} . But it would also result in increased frequency shifts due to micromotion (see Eqs. 2.59 and 2.68). The trap capacitance is determined by the trap design and by the relative permittivity ε_r of the dielectric material that is used. The presented trap design profits here from the fact that the amount of dielectrics close to strong electric fields is reduced to a minimum.

The power dissipation per unit volume due to rf absorption in dielectrics, p , can be calculated with [77]

$$p = \Omega_{\text{rf}} \varepsilon_0 \varepsilon_r \tan(\delta) |E|^2 . \quad (3.2)$$

It depends on the trap drive angular frequency Ω_{rf} , the relative permittivity ε_r , the loss factor $\tan(\delta)$ and the electric field E . In Tab. 3.3, material parameters of some common materials are listed. The list shows that there are large variations in the loss tangent $\tan \delta$ and smaller differences in the relative permittivity ε_r . The loss factor of AlN is already a factor 10 smaller than that of Rogers, but still higher than for aluminium oxide (Al_2O_3) or sapphire. Besides the material parameters, the rf absorption also depends quadratically on the electric field strength. Thus in Doležal et al. [76] it is recommended to have dielectric material only at locations with weak electric fields. For the presented trap design this recommendation has not been considered and can probably be further optimized. This optimization of the layered design will always be a trade off between the rf absorption on one hand and the mechanical stability and the heat conduction capability on the other hand.

Heat removal via thermal radiation is undesirable, because the emitted radiation causes the unwanted BBR shifts. The amount of radiation that is emitted by a surface is determined by its temperature and emissivity. The emissivity of a surface depends on the material and on the surface quality. A rough surface will have a higher emissivity than a polished surface of the same material. In addition, the emissivity is a function of the emitted frequency. Materials that are transparent for visible light can be opaque and absorbing in the infrared (IR) spectral range, that is relevant for the black-body radiation close to room temperature. In order to reduce the thermal radiation, hot surfaces that are in direct line of sight of the ions, should have a low emissivity. The emissivity of the polished AlN wafers with and without gold coating have been measured in [76]. It is $\varepsilon_{\text{Au}} = 0.05$ for the sputtered gold surface and $\varepsilon_{\text{AlN}} = 0.73$ for the polished AlN. These are the average values over the wavelength range from 7 to 14 μm .

Because heat removal via radiation is problematic, heat conduction is the best way to efficiently remove the generated heat. Therefore, the thermal conductance from the

Material	Rogers 4350B	Al ₂ O ₃	Sapphire	AlN
loss tangent $\tan \delta$	37×10^{-4}	2×10^{-4}	0.5×10^{-4}	4×10^{-4}
relative permittivity ϵ_r	3.7	9	9.3	8.9
thermal conductivity λ [W/m K]	0.7	23	40	170

Table 3.3.: Material parameters of some materials that have been considered to built the ion trap. The decision to use AlN mainly based on these values and the fact that the first laser cutting tests showed promising results for AlN and problems for sapphire.

hottest parts of the trap to the vacuum chamber has to be maximized. This is achieved by increasing the cross section of the connection and by using materials with a high thermal conductivity λ . The values of the thermal conductivities of some material are listed in Tab. 3.3. The table shows that from the listed materials AlN has the highest value. As ion traps are typically assembled from different parts, the thermal contact between those parts can significantly reduce the effective thermal conductance. The thermal contact conductivity depends on the surface roughness, the material hardness, the cleanliness and the contact pressure. For the ion trap presented in this work, the thermal contact conductivity has been improved by using polished AlN wafer with a surface roughness $R_a = 0.05 \mu\text{m}$ and wherever possible a thin sheet of soft metal (copper or indium foil) or glue between the surfaces was added. Both methods help to increase the effective area of the thermal contact.

Apart from the thermal properties, the materials used inside the vacuum chamber have to fulfil further requirements. They have to be ultra-high vacuum (UHV) compatible in order to reach pressures at the 1×10^{-11} mbar level. They have to be non-magnetic, because magnetic field fluctuations need to be minimized. Furthermore the insulator used for the trap chips needs to have a high breakdown threshold and also a high mechanical stability. A bending of the trap chips, which was observed for the prototype trap, [30] can lead to an increased amount of axial micromotion and needs to be avoided.

3.5. Trap Manufacturing Process

This section summarizes the trap manufacturing process that was developed in close collaboration with PTB's scientific instrumentation department. The complex process is divided into many steps that depend on each other.

In total five AlN traps have been assembled completely. The traps are listed in chronological order in Tab. 3.4. The numeration will be used throughout this work to refer to the individual traps. The first two traps were not fully functional and have been used to further improve the manufacturing process and the trap design. However, trap II was also used for the first experimental thermal analysis [76]. The results of

trap number	year of assembly	description
I	2013	first test of assembly process, problems with gold layer adhesion, with hand soldering of SMD's and with flux removal
II	2014	used for experimental thermal analysis (see Ref. [76] and Sec. 5.1) improved cleaning processes and reflow soldering implemented minor problems with gold layer adhesion on cut faces
III	2015	used for experimental thermal analysis (see Sec. 5.1) fully functional trap, final test of manufacturing process PRF chips with thinner gold layer of 2.5 μm
IV	2015	installed into vacuum chamber, fully functional trap fully characterized trap (see chapter 5)
V	2016	backup for future experimental setups, fully functional trap

Table 3.4.: List of manufactured AlN traps. The numeration is used throughout the text to refer to a certain trap. Further differences in the trap manufacturing process are discussed in the main text.

these investigations have been used to further improve the thermal management (see Sec. 3.4 and 5.1). Besides small differences, the trap manufacturing process has been identical for traps III, IV and V. Trap IV was installed into the vacuum chamber for a full characterization of the trap properties. The manufacturing steps 1 to 6 of the following description have been carried out by PTB's scientific instrumentation department. The last manufacturing steps 8 to 10 have been carried out in PTB's clean room centre, which reduces the contamination with dust particles to a minimum.

1. Aluminium nitride wafer

The starting basis for the trap chips are polished AlN wafer² with a size of 114.3 mm \times 114.3 mm and a thickness of (380 ± 25) μm . One of these wafers is used to manufacture four trap chips. The raw material for the spacer that separate the trap chips are also polished AlN wafer with a thickness of (1000 ± 25) μm and (127 ± 13) μm . For traps I and II, unpolished material has been used, which reduces the thermal contact conductivity (see Sec. 3.4 and 5.1).

2. Laser cutting of the chip geometry

The first step in the manufacturing process is to cut the AlN wafer to get the desired geometry (see Fig. 3.7 (a)). Before the laser cutting, a protective lacquer³ was applied on both sides of the wafer with a lint-free wipe. The purpose of the

²Valley Design Corporation; www.valleydesign.com; Material properties as supplied by the manufacturer are listed in Tab. A.2.

³AZ positive photo resist

lacquer layer is to protect the surface of the AlN wafer from residues originating from the cutting process. Laser cutting was done with a nanosecond pulsed laser⁴. The laser beam was steered by a scanning mirror, which was placed approx. 200 mm above the AlN sample. The laser cutting parameters have been optimized to get smooth and reproducible edges.

3. Cleaning and etching of the chip

Before the gold coating can be applied to the wafer, the protective lacquer and all cutting residues have to be removed. The cleaning process is crucial to ensure a good adhesion of the gold layer to the AlN substrate. The problems with the gold layer of the traps I and II could be traced back to an insufficient cleaning procedure. Usually the lacquer dissolves easily in any common solvent, but it is more difficult to remove the burnt lacquer close to the laser cuts. Furthermore, at the cutting point the laser is melting the AlN wafer and leaves an aluminium layer on the cut faces. This aluminium layer also reduces the adhesion of the coating and therefore needs to be removed. For trap II this layer was not removed properly and therefore the gold layer was peeling off only at the cut faces. In a first step the wafer is immersed into N-ethyl-2-pyrrolidone (NEP) for at least 12 h and put into an ultrasonic bath for further 15 min. This removes the protective lacquer. The Al layer at the cut faces is then removed with phosphoric acid. For every trap chip the cleanliness is checked by optical inspection.

4. Gold coating

In the next step a gold coating is sputtered onto the trap chips (see Fig. 3.7 (b)). A titanium layer of 20 nm thickness is used as adhesion layer between the AlN substrate and the gold coating. In order to coat also the side walls of the slits and the vias the AlN wafer is tilted to different angles during the sputtering process (-15° , 0° and 15°). It is estimated by geometric considerations that the coating thickness within the 100 μm wide slits is only 1/10 of the nominal thickness. A mask has been used to cover areas that should not be coated. Different designs for this mask have been tested. It is important to use a rigid design, because otherwise the tension, that is exerted by the sputtered gold layer, bends the mask and gold is deposited underneath the mask. If this happens, the gold layer will not have a defined edge, but will run out. This makes it difficult to see where the coating ends and a larger area of the coating needs to be removed by time-consuming laser ablation. If especially the very thin gold layers are not removed they will lead to additional rf losses and an increased temperature rise [78]. The thickness of the gold layer has been measured with a profilometer. The measurements showed that there are thickness fluctuations varying from chip to chip on the order 1 μm and additionally there is a reproducible thickness gradient. The gradient can be explained with the geometry of the sputtering system. Areas that are further away or laterally shifted to the sputter source have a thinner gold coating. The measured thickness varied from 3.5 to 6.0 μm .

⁴Coherent AVIA 355-10-20 QS, 355 nm, 23 ns pulses, 300 μJ max. pulse energy, 15 μm focus size

Additionally, the electrical conductivity of the gold surface has been measured with 4-wire sensing. Compared to bulk conductivity of a 4 μm thick layer, the measured conductivity is on average a factor 1.7 lower.

5. Formation of electrodes via laser ablation

After the sputtering process the gold layer has to be separated into individual electrodes (see Fig. 3.7 (c)). Therefore, a protective lacquer is applied to the AlN wafer as described in step 2. Subsequently the electrodes are divided by laser ablation. The alignment of the trap chip to the laser beam was achieved via a camera and a pilot beam. The laser parameters used for ablation have been optimized to safely remove the gold layer and at the same time not to cut deeper into the AlN than needed. With a tactile surface profiler it was measured that approximately 5 μm of the AlN substrate have been removed due to the laser ablation. Also, along the path of the laser, ridges are visible on the AlN surface.

6. Cleaning and etching of the chip

As described before for the laser cutting, also the laser ablation leaves burnt lacquer and an aluminium layer on the trap chip which both have to be removed. If the aluminium layer is not removed, the trap electrodes will not be electrically isolated against each other. The lacquer is not vacuum compatible and leads to increased rf losses. The cleaning procedure was identical to the one in step 3.

7. Soldering of SMD's and copper stripes

To reduce ac noise on the dc electrodes to a minimum, all of them have an RC low-pass filter soldered directly onto the trap chips (see Fig. 3.7 (d) and (e)). The resistors⁵ have a resistance of $(300 \pm 15) \text{ k}\Omega$ and the capacitors⁶ have a capacity of $(4.70 \pm 0.24) \text{ nF}$. Both parts have SMD package size 0402, which is approximately 1 mm \times 0.5 mm. Additionally, the two PRF chips are equipped with Pt100 temperature sensors⁷ of SMD package size 0805 (2.1 mm \times 1.4 mm). To avoid self heating, the temperature sensors are protected from ac currents by two capacitors⁵ placed in parallel. For trap I it has been tried to hand solder the SMD's onto the trap chips. This turned out to be very problematic. First of all, the high thermal conductivity of the AlN makes it necessary to heat up the trap chip with an IR heating plate in order to achieve a sufficiently high temperature. Furthermore there are many small solder pads close together (1 mm width, separated by 0.1 mm), which has a high risk of producing short circuits. To have a reliable result, a reflow soldering process was implemented. Therefore, a solder paste⁸ was applied to the chips using a custom-made solder mask⁹. Because the trap chips do not have any solder stop mask, it is necessary to reduce the amount of flux in the solder paste. This was achieved by not stirring the paste

⁵Barry Industries, RP0402BA-3003JN-91, alumina chip resistor with palladium silver termination

⁶Novacap, 0402C472J500PH-HB, non-magnetic X7R dielectric with palladium silver termination

⁷Heraeus, SMD 0805-FC, tolerance class B with silver platinum thick film termination

⁸Kester EM907, alloy Sn96.5Ag3Cu0.5, "no-clean" flux

⁹Beta Layout GmbH

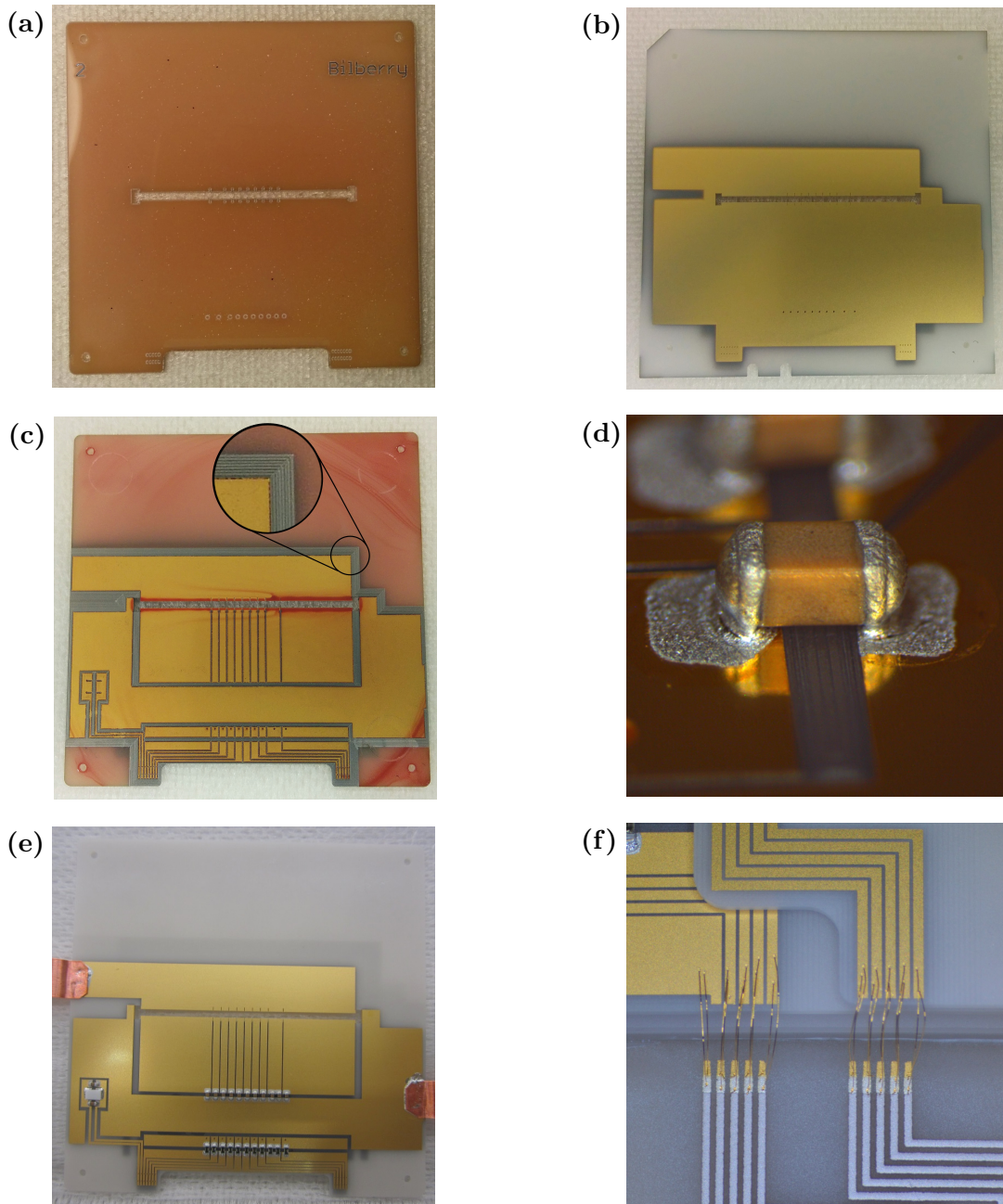


Figure 3.7.: The pictures show the different steps of the trap manufacturing process. **(a)** PRF2 wafer of trap II after laser cutting of the geometry, but before the reddish protective lacquer is removed. **(b)** PRF2 wafer of trap IV after sputtering of the gold layer. **(c)** The same wafer as in (b) after formation of the electrodes via laser ablation. The aluminium layer that is generated by the laser ablation process is visible in the inset. The ablated lines have a shiny silver colour. **(d)** Microscope image of a reflow soldered SMD capacitor after removal of the flux. The size of the capacitor is approximately $1 \text{ mm} \times 0.5 \text{ mm}$. **(e)** The same PRF2 wafer as in (b) and (c) after flux removal and before the trap assembly. Copper stripes have been hand soldered to the wafer for the rf and the ground connection. **(f)** Microscope image of the wire bonds with a diameter of $25 \mu\text{m}$. The bonds connect the conductors from the support board to the trap chips.

before it is applied, because during storage of the solder paste the flux settles at the bottom of the pot. The next step was to place all SMD parts on the solder and put the chips into a reflow oven¹⁰. The temperature profile of the reflow oven was optimized to follow the recommendation of the solder paste data sheet. Therefore, the temperature was measured with an external thermocouple placed directly on the AlN surface. The reflow soldering process was very reliable. For traps III to V in total 546 SMD parts have been soldered. The solder did not produce any short circuit. Even if the paste is not centred on the electrode, when it melts it aggregates at the terminations of the SMD parts. The only defect, which was observed for 3 capacitors, was the so-called tombstone effect, where one end of the SMD part raises and does not have contact to the solder pad any more. It occurs if the solder on one side of the chip melts earlier than the other and due to the surface tension lifts up the part. This defect was not observed for any part on traps IV and V, where the SMD parts have been aligned centred between the two solder pads. The defective SMD parts have been replaced using hand soldering. The last soldering step was to hand solder the oxygen-free high thermal conductivity (OFHC) copper stripes (5 mm width and 0.1 mm thickness) for the rf and ground connection. After soldering, each trap chip has been tested for short circuits and all capacitances and resistances have been measured. At this point also the preparation of the support board¹¹ started by soldering Kapton wires to the solder pads. To have a strain-relief the Kapton wires have been fixed to the board with glue¹².

8. Cleaning of flux

After soldering of the SMD parts and of the copper stripes, the solder flux needs to be removed, because of its unknown vacuum compatibility and rf loss tangent. The first step of the cleaning procedure was to immerse the chip for 1 h into a water-based flux remover¹³. The flux remover was heated in a water bath to 50 °C. The ultra sonic bath was used for 30 s. To remove all residues of the flux remover the chip was cleaned in the ultra sonic bath with isopropyl alcohol for further 30 s. In the end, the chips were rinsed with deionized water and blow-dried with nitrogen. All trap chips have been optically inspected with a stereo microscope after the cleaning procedure. For some trap chips the described procedure has been repeated to remove all visible flux residues. The trap support board has been cleaned with the same procedure.

9. Trap assembly

The critical point of the trap assembly is the alignment of the trap chips (see Sec. 3.3). Therefore, the alignment was done under a measuring microscope¹⁴. The accuracy and repeatability of the microscope measurements is described in

¹⁰Eurocircuits GmbH, ec-Reflow-mate

¹¹Lust Hybrid-Technik GmbH, incl. thick film solder and bonding pads

¹²Electronic Materials Inc., Optocast 3410 Gen2

¹³Techspray, ECO-dFluxer SMT100, 1:4 dilution with high-purity water

¹⁴Nikon MM-400

the following Sec. 3.6. The different trap chips and spacers are glued together using a vacuum compatible epoxy with ultra low shrinkage¹². The glue can be cured with UV light and heat. With the UV light it was possible to cure the glue directly on the microscope table with a minimized risk of misalignments. The first step of each alignment was to align the first lower lying trap chip to the cross-hairs of the microscope. For the alignment of the lower trap chip the xy translation stage and the rotation stage of the microscope has been used. Then the next trap chip is placed on top of the aligned trap chip. The friction between the two chips is increased by carefully putting some weight onto the trap chip. After checking the alignment of the lower lying trap chip to the cross-hairs again the focus is adjusted to the upper trap chip. Then the upper chip is manually aligned to the cross-hairs. Before the glue is applied it was checked again that the lower lying trap chip did not move with respect to the cross-hairs. Then the glue is applied with a thin copper wire to the four gluing holes of the trap chip and cured with UV light. Now the additional weight also ensures that the glue is not creeping in between the trap chips. Besides using a different more convenient microscope, the alignment and assembly process is identical to the process described in Karsten Pyka's thesis [30]. It also includes a more detailed description of the geometry of the gluing holes. Compared to this description only the gluing of the support board was changed for traps III to V. In order to increase the thermal contact conductivity a thin layer of glue was applied to the whole contact area between the trap stack and the support board. In order to make sure that the glue is cured everywhere, the glue has been cured also thermally. Therefore the trap was baked in an oven at 150 °C for 1 hour.

10. Wire bonding

The final step of the trap manufacturing process was to bond wires between the support board and the dc electrodes of the trap chips (see Fig. 3.7 (f)). Therefore, a half automated gold wire wedge bonder¹⁵ has been used. The thickness of the bond wire was 25 µm. The bonding parameters have been optimized to get the best possible bond strength. For each connection, two bond wires were used to reduce the risk of failures due to loose bond wires.

An image of the fully assembled trap is shown in Fig. 3.8. The trap is mounted inside the vacuum chamber with the help of L-shaped mounts and screws that fix the trap carrier board. An image of the trap mounted inside the vacuum chamber is shown in Fig. 4.1.

¹⁵Kulicke & Soffa, 4523A Digital

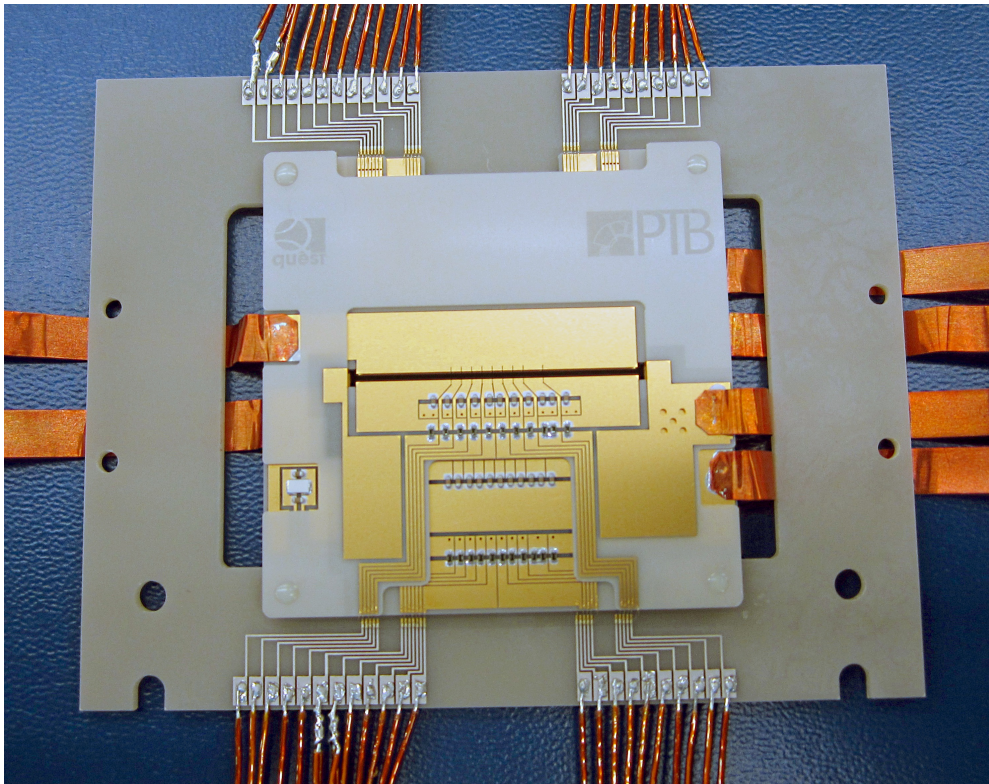


Figure 3.8.: Photo of the fully assembled trap number IV. On the left side there are the two copper stripes for the rf voltage. The four stripes on the right are for the connection to ground. On the top and at the bottom, the Kapton wires for the dc voltages and the temperature sensor readout are shown. For the two temperature sensors two wires are soldered to each solder pad. This is needed for the more accurate four wire resistance measurement.

3.6. Measurements of the Trap Geometry

In order to compare the achieved trap geometry to the target values given in Secs. 3.2 and 3.3, the final trap geometry of trap IV has been characterized extensively. This section summarizes the results of these measurements. The results show that the deviations to the target geometry are within or close to the targeted range given in Tab. 3.2.

3.6.1. Geometry Measurement Tools and their Uncertainty

The trap geometry has been measured with two different tools. Before, during and after the assembly the geometry has been measured with the measuring microscope Nikon MM-400. A photo of this microscope is shown in Fig. 3.9 (a). The microscope with 50-fold magnification is equipped with a manual xy translation stage. The two linear encoder of the stage allow distance measurements with an absolute accuracy of $(2.5 + L/50) \mu\text{m}$, where L is the measured distance in mm. The resolution of the position readout is $0.1 \mu\text{m}$. In addition to the intrinsic errors of the microscope, there is an uncertainty in defining the location of the edges used as start and endpoint of each measurement. By repeated measurements of the length of a single segment a repeatability of 2 to $3 \mu\text{m}$ was deduced. Small angles can be measured with the microscope by moving the cross-hairs along one axis of the translation stage and then measuring the resulting offset to the edge along the perpendicular direction. Moving along the edge of the 30 mm long trap slit and the repeatability of $3 \mu\text{m}$ in the transverse direction gives an uncertainty of 0.10 mrad for the angle.

The second method used to measure the geometry was to make a computed tomography (CT) scan¹⁶ of the assembled trap. The CT scan and its evaluation have been performed in collaboration with the PTB department for coordinate metrology. From the CT images, a three-dimensional computer model of the trap has been generated. The measurements were then performed by fitting lines or planes to the surface of the model. The 3D reconstruction of trap IV is shown in Figs. 3.9 (b) and (c). The algorithm used to generate the 3D model produced artefacts, which can have various reasons. Localized artefacts like peaks or holes on a surface have only a minor influence on the uncertainty of the measurements, because planes were fitted to a larger area and such defects are averaged out. The most important observed artefact was that in the generated model the gold coating appeared to be much thicker than in reality. This effect can be seen by comparing the 3D model in Fig. 3.9 (c) to the microscope image in Fig. 3.9 (d). As a result, in the CT model the distances between all electrodes appear to be smaller than in reality and all trap segments appear to be larger. For the distances and angles deduced from the CT model it is difficult to define an

¹⁶Nikon MCT 225

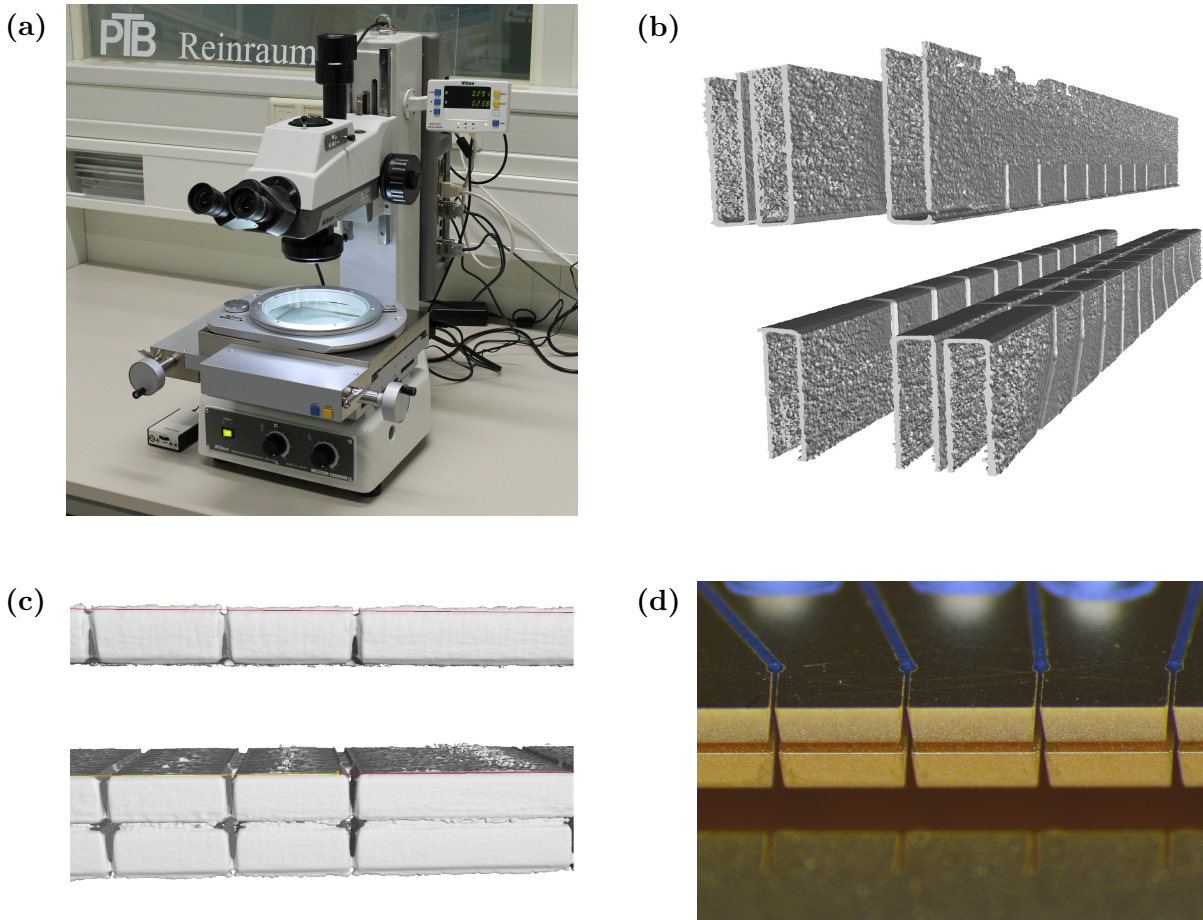


Figure 3.9.: (a) Photo of the Nikon MM-400 measuring microscope that was used to assemble the trap and to measure the trap geometry and alignment. (b) CT scan result: 3D reconstruction of the central electrodes of trap IV. (c) Zoom on the cut faces of the 3D reconstruction. Artefacts are visible that do not allow a precise measurement of the trap geometry. (d) Stereo microscope image showing the real appearance of the cut faces of trap IV. Blurred regions in the image are due to the limited depth of focus of the microscope.

error. The order of magnitude for errors is given by the voxel size, which is approximately $10\ \mu\text{m} \times 10\ \mu\text{m} \times 10\ \mu\text{m}$. To get an idea of the accuracy of angle measurements within the CT scan, angles between the backside edge and the ion side edge of the same laser-cut were evaluated. The largest deviation from zero measured there was 1 mrad. Assuming that the edges are almost perfectly parallel, this value serves as an estimate for the uncertainty of angle measurements in the CT data. Even though the voxel size and the 3D reconstruction artefacts prohibit an accurate measurement of the geometry, the measured distances can be compared to results of the microscope measurement and significant deviations from the targeted geometry should show up in both measurements.

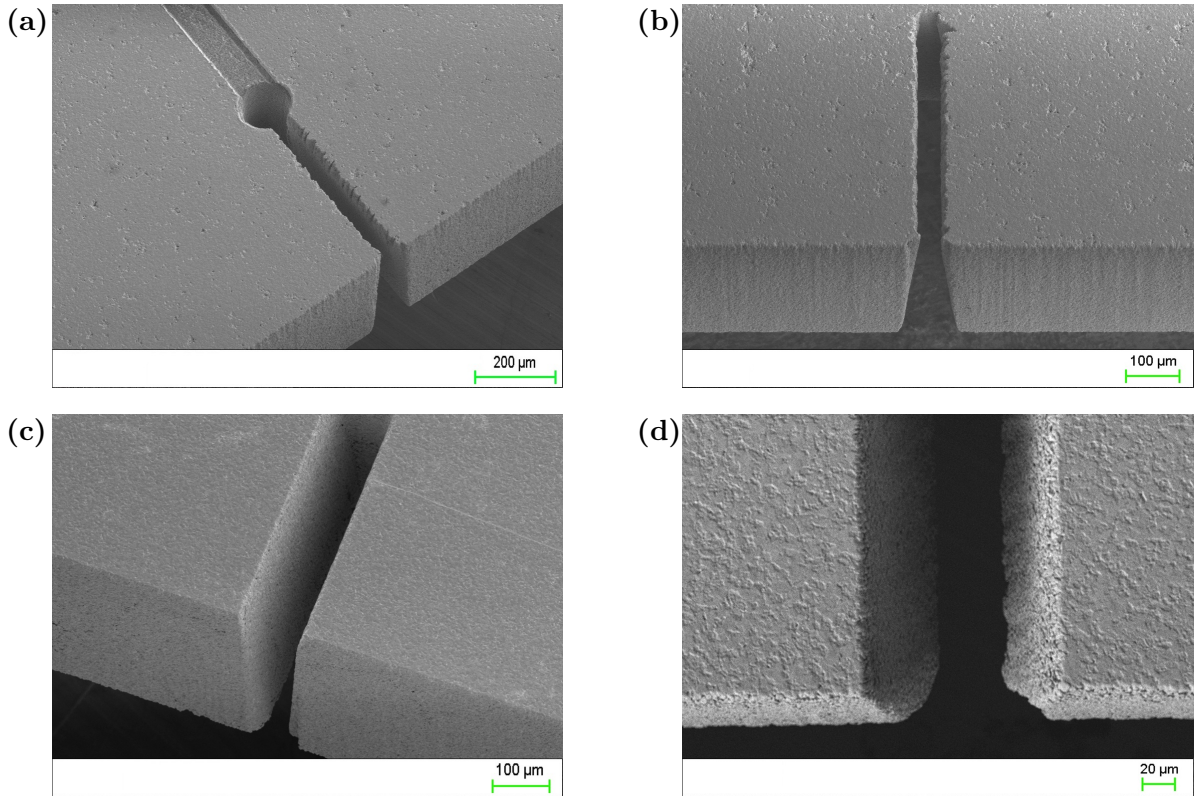


Figure 3.10.: Scanning electron microscope images of a trap wafer showing the achieved laser cut quality. (a) The backside edges of the electrodes show ripples and imperfect corners. The cut faces are mainly smooth with ripples closer to the backside. (b) Backside edge quality of an rf segment. The chamfered geometry of the laser cut is clearly visible. (c) On the ion side the edges are very straight and flat. (d) Close up of the edge quality on the ion side. The backside edge with its irregularities is also visible.

3.6.2. Single Trap Wafer Geometry

The laser cutting parameters have been optimized to achieve highest possible edge quality and reproducibility. The resulting edge quality is shown on the scanning electron microscope (SEM) images of Fig. 3.10. The backside of the chip, which is the side where the laser is exiting, is shown in Figs. 3.10 (a) and (b). Here, the notches between the trap segments show a waviness with an amplitude of approximately $10\ \mu\text{m}$. The ripple originates from diffraction of the laser and appears to be randomly distributed. The waviness along the segment edge is still visible but has a reduced amplitude. It can also be seen that most of the corners on the backside are broken off. However, most of the irregularities are not in a direct line of sight to the ions. Hence, the influence on the electric field at the position of the ions will be reduced. The edge quality on the ion side of the trap chips is shown in Figs. 3.10 (c) and (d). The waviness of the edges is on the order of a few μm . The corners are faultless and have radii of a few μm .

	ion side	backside	CT scan
$\bar{l}_{1\text{mm}}$ [μm]	997	1042	1050
$\Delta l_{1\text{mm}}$ [μm]	2	6	2
$\bar{l}_{2\text{mm}}$ [μm]	1974	2036	2049
$\Delta l_{2\text{mm}}$ [μm]	2	8	1
\bar{w} [μm]	122	60	49
Δw [μm]	2	7	2
\bar{d} [μm]	1021	974	-

Table 3.5.: Average values of the trap segment length \bar{l} , of the notch width \bar{w} and of the width of the trap slit \bar{d} of the four wafers of trap IV and the corresponding standard deviations Δl and Δw . The number of measurements contributing to the mean values are 42 for $\bar{l}_{1\text{mm}}$, 6 for $\bar{l}_{2\text{mm}}$, 54 for \bar{w} and 2 for \bar{d} .

Before trap IV has been assembled, the geometry of each individual wafer was measured with the measuring microscope. The measured distances (see Fig. 3.1) were the segment lengths l_n , the widths of the notch between the segments w_n and the width of the trap slit d . All distances have been measured on the ion side and on the backside of the wafer. The same distances have also been deduced from the CT scan. To measure the notch width and the segment length in the CT reconstruction, planes were fitted to the cut faces of the notches. The distances were then defined as the distance between the geometric centres of two such planes. This differs from the definition shown in Fig. 3.1. The relation between the two definitions is given by

$$l_{n,\text{CT}} \approx (l_{n,\text{back}} + l_{n,\text{ion}}) / 2, \quad (3.3)$$

$$w_{n,\text{CT}} \approx (w_{n,\text{back}} + w_{n,\text{ion}}) / 2. \quad (3.4)$$

The results of the measurements are summarized in Tab. 3.5. The data shows that because of the chamfer the electrodes are longer on the backside than on the ion side. Using the difference of the measured data and the wafer thickness of $380 \mu\text{m}$, the angle of the chamfer is calculated to be between 6° and 10° . The segment lengths l measured with the CT are significantly larger than expected by using Eq. 3.3. Because of an artefact in the 3D reconstruction, the gold coating appears to be much thicker than in reality. This offset makes the segments longer and notches narrower. From the data it can also be seen that the standard deviation of the notch width Δw and the segment length Δl on the ion side is within the target value of $3 \mu\text{m}$. The CT measurements also show a high reproducibility. Both values for the standard deviations are within the measurement uncertainty. The standard deviation on the backside is significantly larger, which is probably a side effect of the random waviness of the backside edges. Compared to the prototype ion trap [29, 30] made out of Rogers the edge quality has been improved significantly. The reproducibility of the notch width of the prototype trap $\Delta w_{\text{proto}} = 10 \mu\text{m}$ could also be improved.

The parallelism between the two opposing trap electrodes (rf and ground electrode) was measured with the microscope and in the 3D model. In general, it is challenging to measure very small angles in the range of 0.1 mrad with the needed accuracy. An angle of 0.1 mrad corresponds to a distance deviation of only $3\ \mu\text{m}$ over a length of 30 mm. For the backside of the PRF3 wafer, a parallelism deviation of (0.15 ± 0.10) mrad was measured with the measuring microscope. This deviation originates from a waviness of the ground electrode. It was observed that the ground electrode bends slightly at the outer end of end segment 1. Otherwise the edge of the electrode can be described by a straight line. The deviation of all other pairs of electrode edges have been within the measurement uncertainty of 0.10 mrad. The evaluation of the same angles in the CT scan showed that the edges of the ground and rf electrodes are perfectly parallel to each other, if the uncertainty of 1 mrad is taken into account.

3.6.3. Alignment Errors

Besides the imperfections of the individual trap wafer, also all important alignment errors have been measured or at least estimated. The tilt α and the displacements Δz and Δy as illustrated in Fig. 3.6 have been measured after the assembly with the measuring microscope and in the CT model. The measurement results are listed in Tab. 3.6. All measured values of the displacement Δz are below the target value of $10\ \mu\text{m}$. The displacements in y -direction, Δy , stay below this value, too. The microscope measurement of the misalignment angle α also show that the achieved values are at least close to the target value of 0.14 mrad. It has to be considered that the estimated measurement uncertainty of 0.10 mrad is already close to the target value.

When the results of the microscope measurement are compared to the CT measurements, it is seen that both measurements are consistent among each other. Therefore, the uncertainties of both measurements have to be taken into account. The uncertainties have been estimated to be $3\ \mu\text{m}$ for the microscope measurements and $10\ \mu\text{m}$ for CT measurements.

Besides the tilt angle α , there are two more angular misalignments possible. Those two tilts in the xy - and in the xz -plane have been measured by measuring the distance in x -direction between the two PRF wafer at all four corners. This distance is in principle given by the thickness of the spacers between these two wafers, but it could also be that dirt or glue between the contact surfaces lead to an angular misalignment. The distance was measured with the measuring microscope and was in the range between $1024\ \mu\text{m}$ and $1028\ \mu\text{m}$. This corresponds to a maximum tilt angle of 0.08 mrad, which is also below the targeted value. In the same way, the thickness of the trap wafer t_w and the thinner spacer t_{PK} have been measured. The measurement showed $t_w = (389 \pm 6)\ \mu\text{m}$ and $t_{PK} = (135 \pm 2)\ \mu\text{m}$.

compared wafer	$\Delta z/\mu\text{m}$	$\Delta y/\mu\text{m}$	α/mrad
PK1 relative to PRF2	-2	4	0.10
PRF3 relative to PRF2	-2	0	0.10
PK4 relative to PRF3	4	-2	-0.13
PK1 relative to PRF2 (CT)	9	-7	0.4
PRF3 relative to PRF2 (CT)	-7	2	0.0
PK4 relative to PRF3 (CT)	1	-9	0.0

Table 3.6.: Measured displacements Δz , Δy and tilts α around the x-axis between separate trap wafer. Δy was always measured at the position of Segment 4. The values from the CT scan do coincide with the values of the microscope measurement, if the uncertainties of both measurements are taken into account.

3.6.4. Conclusions of the Geometry Measurements

The measurements show that the most important geometry imperfections are within the targeted deviations. Only the waviness on the backside edges and the broken corners lead to larger deviations from the desired geometry. Within its limited accuracy, the CT measurement could confirm the results of the microscope measurement.

For the final fabrication process of single trap wafers it is expected that a high degree of reproducibility can be achieved. The most critical process step here is the laser machining, which is an automated process that allows a high reproducibility independent of the operator. In contrast to this, the assembly of the trap wafers is a purely manual process and therefore different traps may show different alignment errors. Nevertheless the deviation from trap to trap can theoretically be limited by the measurement uncertainty of the microscope measurement. In practice, the person assembling the trap will also have an influence on the final alignment errors.

4. Experimental Setup and Sideband Spectroscopy Sequence

This chapter describes the main components of the experimental setup and the experimental sequence that was implemented for the sideband spectroscopy using the quadrupole transition of $^{172}\text{Yb}^+$. First, the vacuum setup and the electronics for the trap rf and dc voltages are discussed. This is followed by a description of the optical setup that was used to address the transitions of the $^{172}\text{Yb}^+$ ions. Lastly, the implementation of the sideband spectroscopy sequence and the ground state cooling results are presented.

4.1. Vacuum Setup

The main vacuum chamber and the setup inside is shown Fig. 4.1. Its main body is a DN250 tube with additional DN60 and DN40 flanges arranged radially. An ion pump and a titanium sublimation pump maintain the pressure inside the chamber at the level of 5×10^{-10} mbar. In total 11 viewports allow optical access for lasers and for the detection of the ion fluorescence. In order to increase the numerical aperture for the detection, a reentrant viewport has been installed. This allows to have the detection objective on the air side at a distance of approx. 31 mm to the ions.

The mounting of the ion trap in the vacuum chamber has been optimized for a maximum heat transfer from the trap to the vacuum chamber as this helps to reduce the trap temperature and the uncertainty of the temperature distribution. The ion trap is mounted vertically on AlN legs, which are clamped onto an aluminium platform. Thermal contacts have been improved by putting Indium and Copper foils between the contact areas of the trap, the legs, the platform and the vacuum chamber. The aluminium platform is also used to mount the two atomic ovens and the copper shield. The shield is used to collimate the atomic beams to the loading segment and reduce contamination of the trap with a conducting Yb or In layer. For each beam the shield has a vertical slit of 2 mm length and 0.65 mm width. The ovens are filled with isotope enriched ^{172}Yb and with Indium of natural abundance. The oven design is described in detail in [30]. For future use ablation targets have been added to the setup, but have not been used during this work. The targets consist of thin stripes of Yb and In, both in natural abundance, which are glued onto a Macor mount. Macor has been used because of its low thermal conductivity. Compared to atomic ovens, the use of

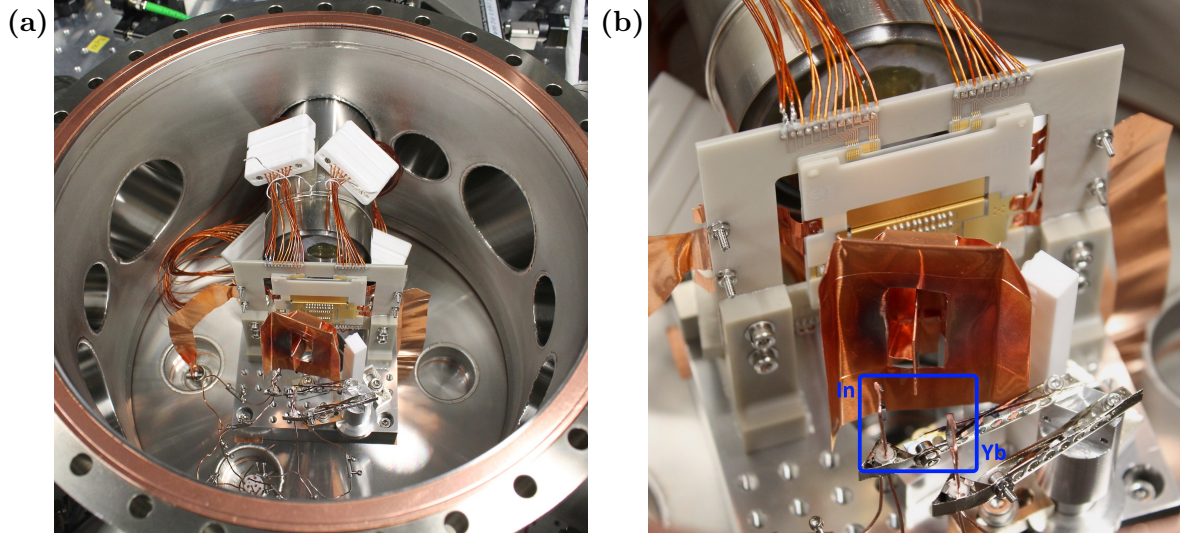


Figure 4.1.: Photographs of the vacuum setup. (a) The image shows the vacuum chamber with its various viewports for 3D laser access and ion imaging. OFHC copper foils on the left and right side of the trap are used for the rf voltage connection. The dc voltage connections are realized with Kapton isolated wires. (b) The close-up of the setup shows the atom ovens for In and Yb inside the blue box in front of the copper shield. Behind the ion trap the re-entrant viewport with the detection objective is visible. The Macor mount for the ablation targets is located to the right of the copper shield.

ablation targets for the generation of neutral atoms has the advantage that the loading time can be reduced from several minutes to a few seconds.

All electrical feedthroughs are located at the bottom of the chamber. A high current feedthrough is used to apply currents of up to 15 A to the atom ovens. A HN-type coaxial feedthrough is used for the trap rf voltage. This type of feedthrough has the advantage that the inner conductor is a thick pin with a diameter of approximately 4.9 mm. This increases rf conductivity and minimizes electrical losses, which would otherwise heat up the chamber and reduce the Q-factor of the rf circuit. The rf voltage is connected to the trap electrodes via copper foils of 100 μm thickness. The rf ground electrodes are directly connected to the vacuum chamber. Two 25 pin D-sub feedthroughs have been used for the dc voltages and for the 4-wire readout of the two Pt100 sensors on the trap. Kapton isolated wires connect the dc electrodes of the trap to the feedthrough. Four UHV compatible 15 pin Sub-D connectors have been used to allow a more convenient exchange of the trap in the future.

To reduce magnetic field fluctuations, almost all materials in the vacuum chamber are non-magnetic. The chamber itself and all attached flanges are made from non-magnetic stainless steel. All materials on the trap chips including the SMD parts and the temperature sensors are completely non-magnetic. The only exception are the crimp pins of the in-vacuum D-sub connectors that have a Ni adhesion layer underneath their Au coating. They are located approximately 80 mm away from the ions. In order

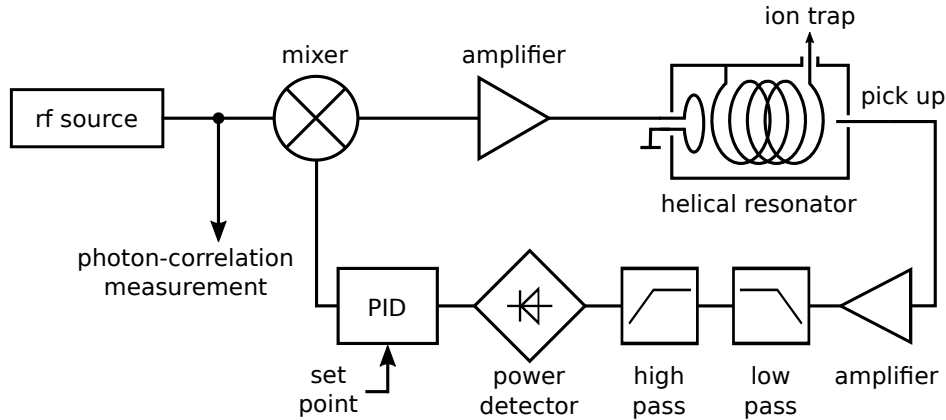


Figure 4.2.: Schematic of the main components of the rf drive circuit. An isolated pin inside the helical resonator has been used to pick up a fraction of the rf voltage. The pickup signal can be used to either monitor the rf voltage amplitude or as depicted to close a feedback loop and stabilize the rf amplitude.

to compensate the constant magnetic fields and to set the quantization axis, three pairs of magnetic field coils in Helmholtz configuration have been attached to the vacuum chamber. The coils allow to apply magnetic fields of approximately 0.2 mT pointing into an arbitrary direction.

4.2. Trap Voltages

4.2.1. RF Circuit

A schematic of the setup of the rf circuit that was used at the end of this work is depicted in Fig. 4.2. The rf signal, which is generated by a signal generator¹, is divided into two paths. One path is used for the photon-correlation measurement (see Sec. 5.3) and the other path is used to drive the trap. A frequency mixer² is used to control the amplitude of the rf signal. There have been three different use cases for this mixer. Firstly it has been used to modulate the rf amplitude for the determination of trap frequencies via parametric heating. Secondly it has been used to quickly ramp down the rf amplitude for the generation of topological defects (see Sec. 6). Thirdly, as depicted in Fig. 4.2, the mixer has been used as the control element of the feedback loop for the rf amplitude stabilization.

The output signal of the frequency mixer is first amplified³ and then enhanced by a helical resonator, which is directly attached to the vacuum feedthrough. The design of the helical resonator is described in detail in [30]. Inside the helical resonator the

¹Marconi, 2024

²Minicircuits, ZAD-6+

³Minicircuits, ZHL-5W-1, amplification 46dB

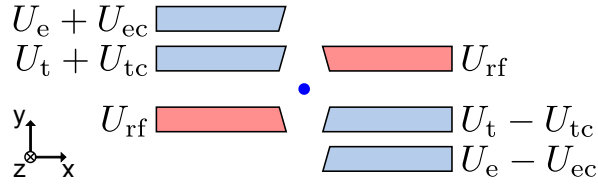


Figure 4.3.: Side view of a trap segment illustrating the application of the different dc voltages. The two symmetric voltages U_t and U_e allow to set the orientation of the principal axes arbitrarily. The two asymmetrically applied voltages U_{tc} and U_{ec} are used to shift the ion in the xy -plane.

signal is coupled inductively from a single turn primary coil to a 9-turn secondary coil. For impedance matching of the two circuits, the distance between the primary and secondary coil has been optimized. Besides enhancing the rf voltage, the narrow resonance of the helical resonators filters electric noise effectively. With the new trap installed, the quality factor of the resonance was measured to be $Q = 604$ and the resonance frequency was at $\Omega_{\text{rf}} = 24.38$ MHz. A short isolated wire protruding into the helical resonator is used to pick up a fraction of the rf voltage $U_{\text{rf}} = k \cdot U_{\text{pick up}}$. The comparison between the measured pick up voltage, the measured trap frequencies and the results of the trap potential simulator (see Sec. 3.3 and appendix A.5) results in a calibration factor of $k = 4940$. The pick up voltage has been used either to monitor the trap voltage amplitude or for the stabilization of the rf amplitude. Therefore, the signal has first been amplified. A low-pass and a high-pass filter has been used to filter noise above and below the resonance frequency. An rf power detector⁴ is used to generate a dc voltage, which increases almost linearly with the dc voltage. The resulting signal is used as an input for a PI controller. With the rf stabilization loop both the long term and the short term stability of the rf amplitude could be improved significantly.

4.2.2. DC Voltages

The increased number of segments of the AIN trap compared to the prototype trap made it necessary to build a new dc voltage supply. The setup is similar to the dc voltage supply described in [30]. Fig. 4.3 shows the voltages that are generated for each trap segment including the two end segments. The symmetric voltage configuration of the voltages U_t and U_e is used for axial confinement of the ions and for squeezing of the radial trap potential with an arbitrary orientation of the two principal axes. The antisymmetric voltage configuration of the voltages U_{tc} and U_{ec} is used to shift the total potential minimum radially. These voltages are used to compensate stray fields and to minimize radial micromotion.

⁴Keysight 8471D

The voltages \tilde{U}_t , \tilde{U}_{tc} , \tilde{U}_e and \tilde{U}_{ec} are generated for each trap segment by three computer-controlled analogue output modules⁵ mounted in a single chassis⁶. In order to avoid ground loops, the chassis is connected to the host PC via an USB galvanic isolator and is powered by a floating linear power supply. The voltages from the analogue output modules are used as input signal for a self built analogue circuit (see appendix A.3). This circuit generates the four voltages for the individual trap electrodes according to the following equations.

$$\begin{aligned} U_{t+} &= 1.2\tilde{U}_t + 0.25\tilde{U}_{tc} = U_t + U_{tc}, \\ U_{t-} &= 1.2\tilde{U}_t - 0.25\tilde{U}_{tc} = U_t - U_{tc}, \\ U_{e+} &= 1.2\tilde{U}_e + 1.2\tilde{U}_{ec} = U_e + U_{ec}, \\ U_{e-} &= 1.2\tilde{U}_e - 1.2\tilde{U}_{ec} = U_e - U_{ec}. \end{aligned}$$

The scaling factors are used to increase the resolution of the electric field generated by U_{tc} , or respectively to increase the voltage range of the other three voltages. Measurements with a digital multimeter⁷ showed that for all voltages the total deviation between expected and measured output voltages is less than 30 mV over the whole voltage range. This deviation is caused by the tolerances of the used resistors, the tolerances of the offset and gain factors of the operational amplifiers, and the limited accuracy of the voltage source.

For the usual trap parameters used within this work ($\Omega_{rf}/2\pi = 24.38$ MHz and $\omega_{rad}/2\pi \approx 500$ kHz), a change of 1 mV of U_{tc} corresponds to a dc field of 0.92 V m⁻¹, a change of the ion position causing a change of rf field amplitude of $E_{rf} = 63$ V m⁻¹ or respectively to a fractional frequency shift of 3.3×10^{-19} for $^{115}\text{In}^+$. Therefore, it is required that the voltage resolution is sufficiently high and the long term drift of the voltages is as low as possible. The measurement of the long term voltage stability plotted in Fig. 4.4 (a) shows, that for the duration of 14 h the voltage drift is within an error band of approximately ± 100 μV . This demonstrates that the dc voltage supply does not contribute significantly to the second order Doppler-shift and also has a suitable resolution for the minimization of micromotion.

Another requirement for the dc voltage supply is to suppress voltage noise at the trap frequency ω_{sec} . This technical noise will otherwise contribute to the ion heating rate [66]. For noise suppression the analogue circuit includes a second order low pass filter with cut off frequencies around 1 kHz. Additionally, each trap segment is equipped with another low pass filter with a cut off frequency of 113 Hz placed directly on the trap chips. The measured voltage noise spectrum at the output of the self-built analogue circuit is shown in Fig. 4.4 (b). It shows that the second order low pass filter suppresses the noise above 1 kHz efficiently. For frequencies above 10 kHz, the measurement is limited by the instrument noise. The graph also shows the expected voltage noise

⁵NI 9264, 16 channels, ± 10 V, 16-Bit resolution

⁶NI cDAQ 9174

⁷Agilent, 34401A, 6 1/2 digit multimeter

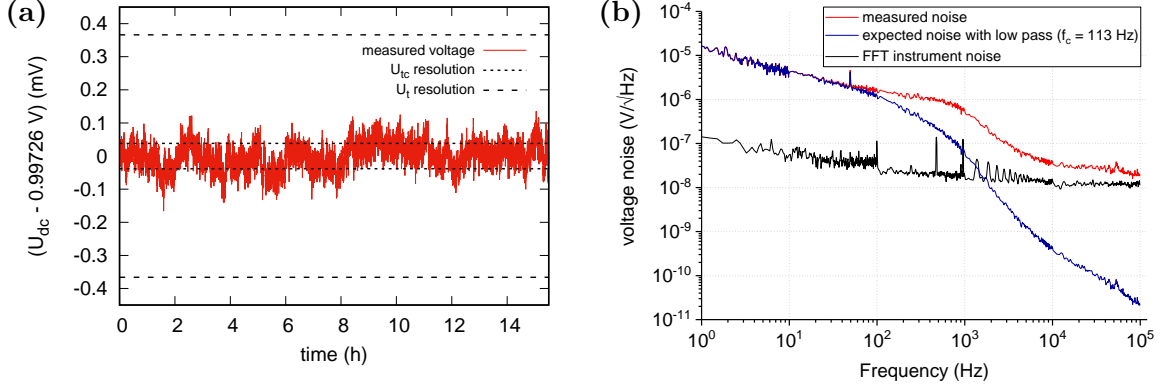


Figure 4.4.: (a) Long term stability of one dc voltage as generated by the self built analogue circuit. The voltage remains in an error band of approximately $\pm 100 \mu\text{V}$. The graph also shows the voltage resolution for U_{tc} and U_t . (b) Plots of the dc voltage noise: Red Curve: Measured voltage noise at the output of the self built analogue circuit. Black Curve: Instrument noise of the spectrum analyzer with shorted input. Blue Curve: Calculated voltage noise with theoretically expected behaviour of low pass filter ($f_c = 113 \text{ Hz}$) directly on the trap wafer.

spectrum when the theoretical effect of the low pass filter on the trap chips is added to the measured signal. Then the voltage noise at 100 kHz is at a level of $20 \text{ pV}/\sqrt{\text{Hz}}$. For a trap frequency of $\omega_{\text{rad}}/2\pi = 500 \text{ kHz}$ and $^{172}\text{Yb}^+$ ions this corresponds to a heating rate of 3×10^{-3} phonons/s (derived with Eqs. 4.2, 4.5), which is significantly lower than the measured heating rate of 1.1 phonon/s (see Sec. 5.4). Thus technical noise most certainly only has a minor contribution to the observed heating rate.

Another source of voltage noise that is contributing to ion heating rate is Johnson-Nyquist noise, which is generated by the thermal motion of the electrons (or other charge carriers) inside electrical conductors. The following calculation of the effect of Johnson noise on the heating rate in the 2 mm wide trap segment 1 is based on the descriptions in Ref. [66]. The power spectral density of the generated voltage noise due to the Johnson noise is given by

$$S_V(\omega, T) = 4k_B T R(\omega, T). \quad (4.1)$$

The voltages noise generates an electric field noise at the ion position of

$$S_E(\omega, T) = \frac{2S_V(\omega, T)}{D^2} = \frac{8k_B T R(\omega, T)}{D^2}, \quad (4.2)$$

where D is the characteristic distance of the trap electrodes to the trap center and a factor 2 is added, because the independent voltage noise on both U_{tc} electrodes of the selected trap segment contribute to the electric field noise. The characteristic distance is defined by $D = U_{tc}/|\vec{E}_{\text{dc}}| = 2.2 \text{ mm}$, where $|\vec{E}_{\text{dc}}|$ is the absolute value of the electric field strength that is generated by a differential voltage of U_{tc} between the two dc electrodes. By using the absolute value of the electric field, the worst case is

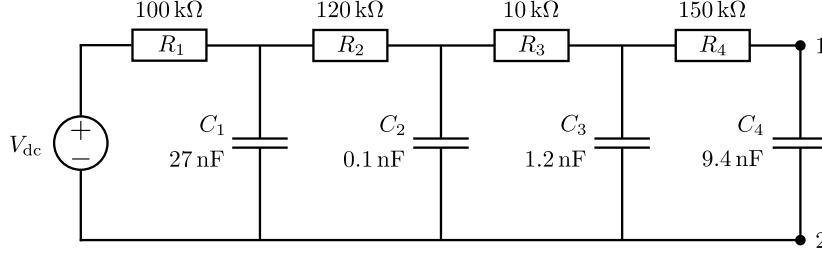


Figure 4.5.: Schematic representation of the dc voltage circuit for U_{tc} . The ions see the voltage noise between point 1 and 2. The resistors R_1 , R_2 , R_3 and the capacitors C_1 , C_2 are part of the self built analogue circuit (see appendix Sec. A.3). C_3 is the capacitance of the cables and connectors that connect the voltages to the ion trap. R_4 and C_4 are part of the low-pass filter that is placed directly on the trap chips.

considered, which assumes that the trap axis is parallel to the electric field vector. The voltage noise will only create a fluctuation of the field amplitude, but the orientation of the field vector is fixed as this is defined by the trap geometry.

For the determination of the effective resistance $R(\omega, T)$, the whole dc filter network as depicted in Fig. 4.5 has to be taken into consideration. With the denotation of $a \parallel b = ab/(a + b)$ for the calculation of parallel impedances, the total impedance between the points 1 and 2 of the circuit is

$$Z_{12} = \frac{-i}{\omega_{\text{sec}} C_4} \parallel \left\{ R_4 + \frac{-i}{\omega_{\text{sec}} C_3} \parallel \left[R_3 + \frac{-i}{\omega_{\text{sec}} C_2} \parallel \left(R_2 + \frac{-i}{\omega_{\text{sec}} C_1} \parallel R_1 \right) \right] \right\}. \quad (4.3)$$

Because $R_4 \gg |-i/(\omega_{\text{sec}} C_3)|$ and any further parallel impedance can only reduce the impedance that is added to R_4 , the real part of $R_{12} = \text{Re}(Z_{12})$ can be approximated by

$$\begin{aligned} R_{12} &\approx \text{Re} \left(\frac{-i}{\omega_{\text{sec}} C_4} \parallel R_4 \right) \\ &= \frac{R_4}{(\omega_{\text{sec}} R_4 C_4)^2 + 1}. \end{aligned} \quad (4.4)$$

With this approximation and using $\omega_{\text{sec}} = 2\pi \times 500 \text{ kHz}$, the effective resistance is $R_{12} = 7.6 \text{ m}\Omega$, which has also been confirmed by the full calculation of the impedance according to Eq. 4.3. Inserting this value in Eq. 4.2 and using $T = 300 \text{ K}$ results in a power spectral density of the electric field noise of $S_E(\omega_{\text{sec}}) = 5.3 \times 10^{-17} \text{ V}^2 \text{ m}^{-2} \text{ Hz}^{-1}$. This value can be transferred to a heating rate \dot{n} measured in the unit phonons/s by

$$\dot{n} = \frac{e^2}{4m \hbar \omega_{\text{sec}}} S_E(\omega_{\text{sec}}). \quad (4.5)$$

Inserting the obtained value of $S_E(\omega_{\text{sec}})$ and using the mass of $^{172}\text{Yb}^+$ the heating rate due to Johnson noise is calculated to be $\dot{n} = 3.6 \times 10^{-3} \text{ phonons/s}$. This value is found to be negligible compared to the measured heating rate of 1.1 phonon/s (see Sec. 5.4).

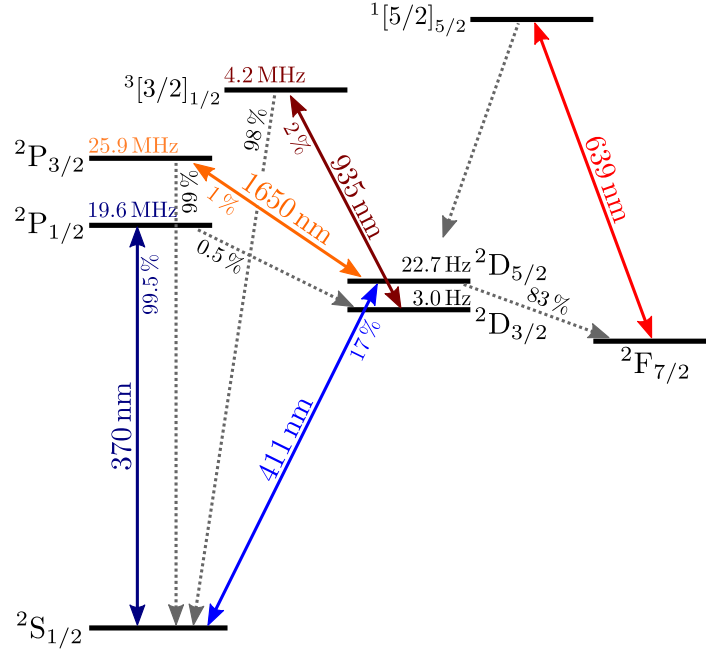


Figure 4.6.: Reduced $^{172}\text{Yb}^+$ term scheme which shows all used transitions and the natural linewidths and branching ratios of the excited states. Numbers are taken from the Appendix of [58] and references therein.

4.3. Optical Setup

4.3.1. $^{172}\text{Yb}^+$ Term Scheme

For the ion trap characterization, $^{172}\text{Yb}^+$ ions have been used for various reasons. It offers a convenient alkali-like term scheme (see Fig. 4.6) and because of its mass it allows efficient sympathetic cooling of $^{115}\text{In}^+$ [47]. $^{172}\text{Yb}^+$ has a vanishing nuclear spin and thus no hyperfine structure, which greatly reduces the number of transitions that need to be addressed. All relevant transitions are accessible with diode lasers (partly frequency doubled). It also offers two usable narrow clock transitions namely the quadrupole transition $^2S_{1/2} \leftrightarrow ^2D_{5/2}$ and the octupole transition $^2S_{1/2} \leftrightarrow ^2F_{7/2}$. Those can be used to characterize the main sources of frequency shifts of the $^{115}\text{In}^+$ clock transition or to realize a frequency standard solely with $^{172}\text{Yb}^+$ ions.

The dipole transition $^2S_{1/2} \leftrightarrow ^2P_{1/2}$ at 370 nm with a linewidth of $2\pi \times 19.6$ MHz [79] is used for efficient Doppler cooling, ion imaging and state detection via the electron shelving technique [44]. Because the excited $^2P_{1/2}$ state has a 0.5% probability to decay into the $^2D_{3/2}$ state [80], it is necessary to drive the repumping transition $^2D_{3/2} \leftrightarrow ^3[3/2]_{1/2}$ at 935 nm to keep the ion in the cooling cycle. A combination of collisional and radiative decays can also lead to a population of the long living $^2F_{7/2}$ state [81]. This state is depleted by laser light at 639 nm that drives the $^2F_{7/2} \leftrightarrow ^1[5/2]_{5/2}$ transition.

For resolved sideband spectroscopy the narrow quadrupole transition ${}^2S_{1/2} \leftrightarrow {}^2D_{5/2}$ at 411 nm with a linewidth of $2\pi \times 22.7$ Hz was used. The transition ${}^2D_{5/2} \leftrightarrow {}^2P_{3/2}$ at 1650 nm has been used for repumping and for quenching of the quadrupole transition [64]. As shown in [58], in combination with the transition at 639 nm it also allows a faster clear out of the ${}^2F_{7/2}$ as it prevents cycling transitions. Further details on the implementation of the sideband cooling scheme are found in Sec. 2.4.2 and Sec. 4.4. The second quadrupole transition ${}^2S_{1/2} \leftrightarrow {}^2D_{3/2}$ is not used, because here the electron shelving technique cannot be used for state detection.

4.3.2. Laser Setup and Beam Geometry

The optical setup around the vacuum chamber and the ion trap is illustrated in Fig. 4.7. All laser beams are coupled into polarization maintaining single mode fibers to deliver the light to the vacuum chamber. This decouples the pointing onto the ions from the rest of the laser setup. The wavelengths of all lasers are monitored by a wavemeter⁸. An 8-channel fiber switch is used to automatically switch between the different laser sources. The highly stable laser light at 822 nm [37, 58] (which is mainly used to generate light at 411 nm) has been used to automatically recalibrate the wavemeter every 10 min. Using a software PI control all other lasers have been continuously tuned to the desired wavelength. In [58] it has been shown that this stabilization to the wavemeter reading has an instability of about 1 MHz for the Doppler cooling laser.

Loading of individual ions into the trap is achieved by photoionization of neutral Yb atoms. Therefore, the atoms in the horizontal neutral atom beam are first excited by laser light at 399 nm from the 1S_0 ground state to the intermediate 1P_1 state. In order to avoid large Doppler shifts this photoionization laser is oriented perpendicular to the atom beam and thus goes vertically through the ion trap. From the intermediate 1P_1 state, a photon at 370 nm has sufficient energy to ionize the atom. As shown in [30] this method is isotope selective.

Doppler Cooling Laser at 370 nm

The Doppler cooling light is generated by an optically amplified and frequency doubled external-cavity diode laser (ECDL)⁹ with an output power of up to 50 mW at 370 nm. The cooling light is guided to the ions from three different directions. Throughout this work, the two horizontal beams are named H1 and H2 and the vertical beam is denoted V. The H1 and H2 beams are aligned at an angle of 25° to the trap axis. V is aligned perpendicular to the trap axis. A telescope setup including a cylindrical lens widens all three beams along the trap axis. The widened beams are implemented to

⁸HighFinesse Angstrom WS/7R MC Super Precision, Measurement range: 350–1100 nm

⁹Optica TA-SHG pro

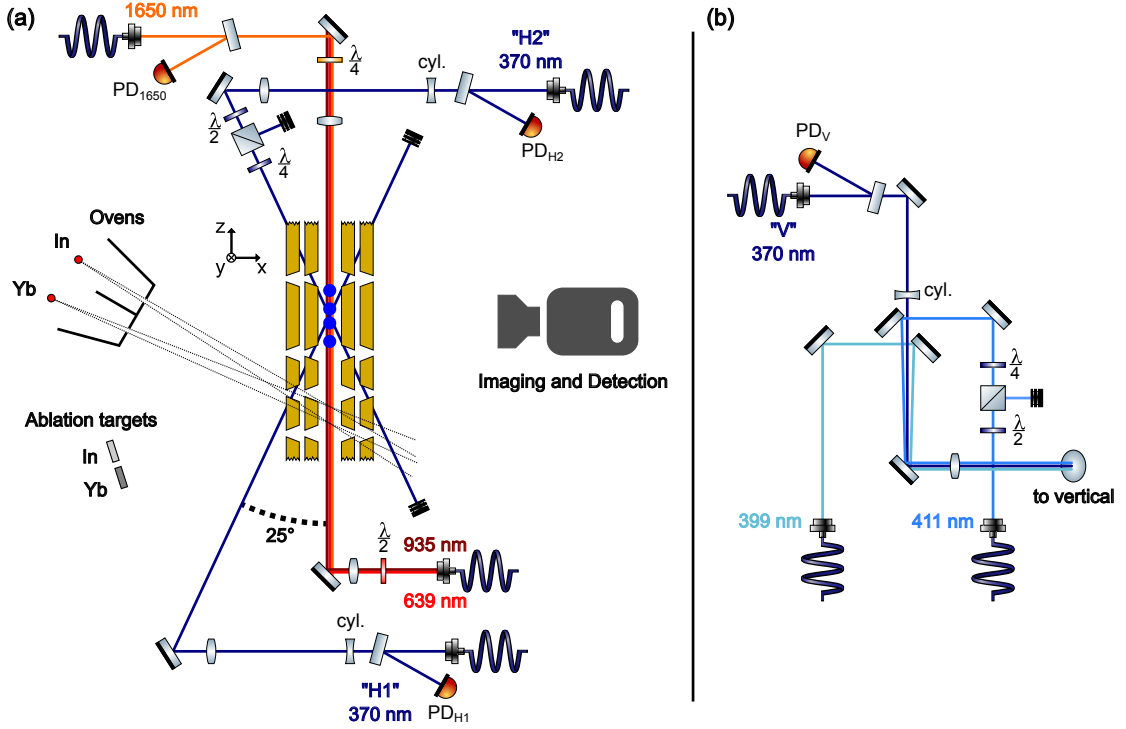


Figure 4.7.: Sketch of the arrangement of the laser beams around the ion trap. To have efficient Doppler cooling of the ions in several segments simultaneously the cooling light beams H1, H2 and V are widened with the help of cylindrical lenses. (a) Beams in the horizontal plane. The three repumping beams (935 nm, 638 nm and 1650 nm) are superimposed along the trap axis. (b) Setup of the laser beams going vertically through the ion trap.

illuminate several segments of the trap simultaneously and to have an approximately homogeneous intensity distribution over larger ion crystals. A fraction of each of the beams is guided to a monitor photodiode. A software control loop uses these signals to adjust and to stabilize the power of the beams via a common acousto-optic modulator (AOM) in the 370 nm laser setup. The three beams can be switched off independently via mechanical shutters that are placed in front of each fiber. H2 has also been used for optical pumping of the ion into the ground state Zeeman level with $m_j = -1/2$ (see Sec. 4.4.2). For an efficient optical pumping, a pure σ^- polarization is needed. Therefore, the polarization is first cleaned by a polarizing beam splitter and with a motorized quarter-wave plate the polarization can subsequently be switched from linear to circular polarization. In order to control the optical pumping pulses independently from the cooling light, a separate AOM is installed in the H2 beam path. This AOM was also used to modulate the H2 intensity in order to measure the trap frequencies (see Sec. 5.2).

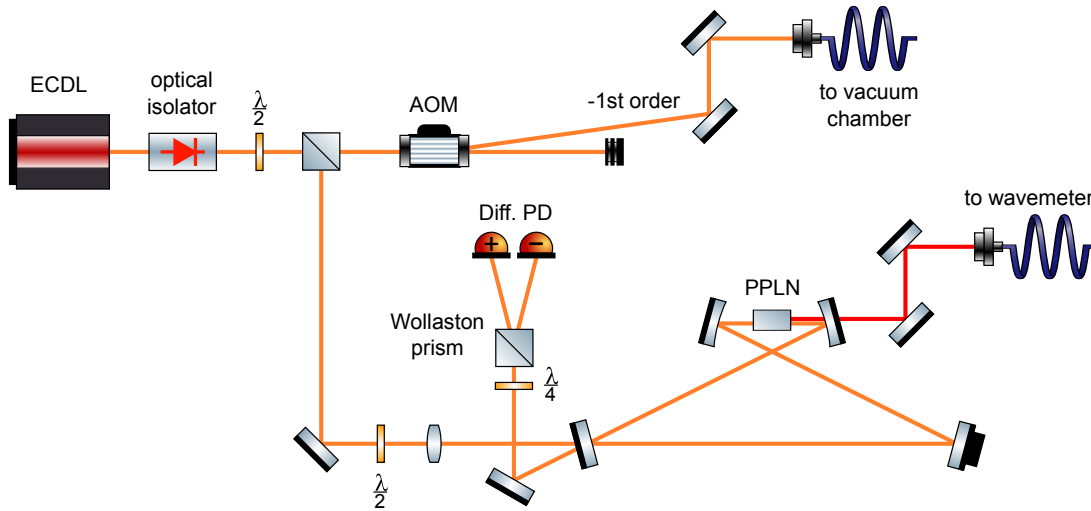


Figure 4.8.: Sketch of the setup for the repumping laser at 1650 nm. In order to have a wavemeter reading with the existing wavemeter and its limited measurement range, a part of the light is frequency doubled by a PPLN crystal inside a bow tie cavity. This also allowed to implement a software lock of the wavelength.

Repumping Lasers

The three repumping beams at 638 nm, 935 nm and 1650 nm are aligned with the trap axis. The 1650 nm beam is counter-propagating to the other two repumping beams. The different directions have been chosen in order to facilitate coupling into single mode fibers and to have an independent control of the polarization of two of the three beams. The polarization of the 935 nm with respect to the vertical quantization axis is adjusted for maximum repumping efficiency from the $^2D_{3/2}$ state. For the generation of pulses for the spectroscopy sequences, the lasers at 1650 nm and at 638 nm have an AOM placed in their beam path. A monitor photodiode is used for the 1650 nm beam to realize a software control of the beam intensity.

A sketch of the laser setup that is used for generating the light at 1650 nm is shown in Fig. 4.8. A part of the light that is generated by an ECDL is frequency doubled in a second-harmonic generation (SHG) cavity with a PPLN crystal¹⁰. The frequency-doubled light is used to couple it to the wavemeter in order to determine the wavelength of the fundamental beam. With a total power of 11 mW in the fundamental beam a maximum power of 0.7 mW was achieved at 825 nm.

The chosen cavity design with a relatively long round-trip length of 0.96 m turned out to be problematic, because of the associated narrow cavity resonances. With the given length the free spectral range is $\text{FSR} = \frac{c}{L} = 312 \text{ MHz}$. Together with the highest measured cavity finesse of $F = 133$ this results in a FWHM value of the cavity

¹⁰Deltronic, 20 mm length, 10 mm width, 1 mm thickness, 9 poling periods from 21.4 μm to 23.0 μm

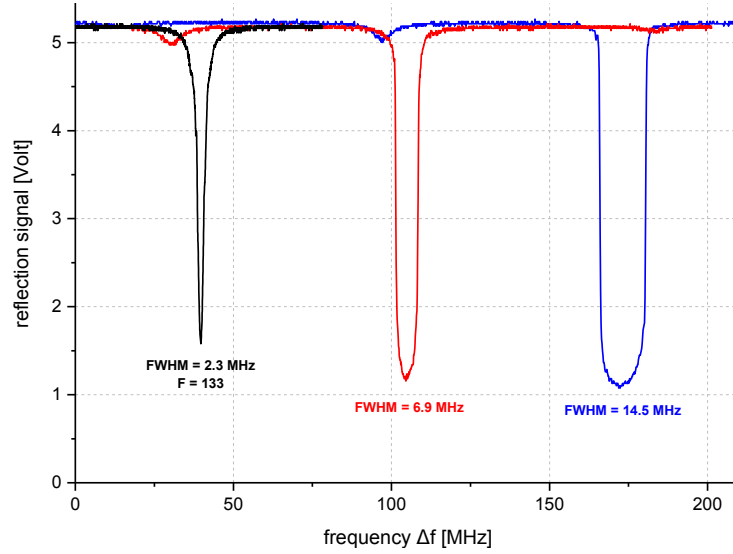


Figure 4.9.: Reflection signals of the 1650 nm SHG cavity during a scan of the cavity length. The only difference between the three shown resonances is the laser frequency, which was changed within one mode hop free tuning range. The broad blue resonance was observed only at the edge of the tuning range. When the laser frequency is changed, the observed cavity resonances are alternating between the black and the red resonance profile.

resonance of 2.3 MHz. This value of the finesse matches to the value which is expected by the specified reflectivity values of the mirror and of the AR coated PPLN crystal. As shown in Fig. 4.9, the FWHM of the SHG cavity was observed to be fluctuating between two values when the laser frequency was changed by the grating of the ECDL setup. A possible explanation for this behaviour could be that the cavity linewidth was comparable to the laser linewidth and in addition the laser linewidth shows a periodic fluctuation when the laser frequency is changing. The fluctuations of the laser linewidth would cause the fluctuating resonance width in the cavity reflection signal. The fluctuating resonance width caused problems for the feedback electronics used for locking the cavity to the resonance. The fluctuating resonance width caused a fluctuating slope of the error signal, that was generated by a Hänsch-Couillaud setup [82]. Because of the fluctuating error signal slope a stable lock could not be achieved. To improve this the cavity finesse was intentionally lowered by clipping a part of the beam inside the cavity. This reduced the output power of the SHG by a factor of four, but allowed to have a stable lock on the cavity resonance.

The ability to measure the frequency of the 1650 nm laser now allowed to measure the resonance frequency of the $^2D_{5/2} \leftrightarrow ^2P_{3/2}$ transition with a higher precision. For this measurement the $^{172}\text{Yb}^+$ ion was illuminated simultaneously with Doppler cooling light at 370 nm, the 411 nm laser, the repumper at 638 nm and the 1650 nm laser. The ion is excited to the $^2D_{5/2}$ state with the light at 411 nm. From there the transition to the $^2P_{3/2}$ state is probed. Subsequently, the ion decays back to the ground state. The

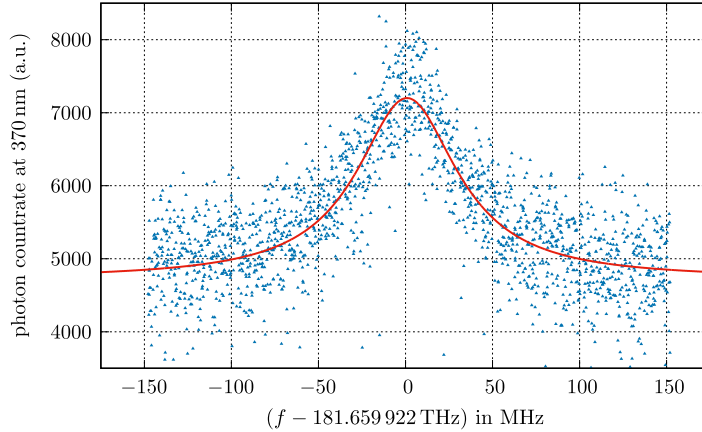


Figure 4.10.: Measurement of the ${}^2D_{5/2} \leftrightarrow {}^2P_{3/2}$ transition resonance frequency. The red line is a Lorentz profile fitted to the recorded data points.

Doppler cooling light is used to cool the ion and to detect the 1650 nm resonance. On resonance, the repumping efficiency is maximized and also the detected fluorescence at 370 nm is maximized. The repumper at 638 nm is needed additionally to get the ion back into the experimental cycle when it has decayed to the ${}^2F_{7/2}$ state. In order to avoid excessive saturation broadening, the 1650 nm laser power has been reduced to approximately 280 nW, which are focused to a calculated waist of 220 μm . The recorded resonance is shown in Fig. 4.10. The fit of a Lorentz profile to the measured data points results in a resonance frequency of 181.659 922(75) THz. The frequency uncertainty results from the uncertainty of the wavemeter of 150 MHz. This error reduces to 75 MHz at 1650 nm, because the wavemeter measures the frequency-doubled light. The vacuum wavelength of the ${}^2D_{5/2} \leftrightarrow {}^2P_{3/2}$ transition is calculated to be 1650.294 98(68) nm. The observed linewidth of the transition is $\Gamma_{1650} = 2\pi \times 70(3)$ MHz. It is assumed that main part of the broadening can still be attributed to saturation broadening.

Sideband Spectroscopy Laser

To resolve the motional sidebands of the quadrupole transition at 411 nm, a highly stable laser was used [37, 58]. It consists out of an ECDL at 822 nm, that is stabilized to a 12 cm long cavity made out of ultra low expansion glass. With this setup a fractional frequency instability of $\sigma_y = 4 \times 10^{-16}$ is reached at 10 s. A fraction of this light is amplified by an injection-locked laser diode. The emitted laser beam of this slave laser is frequency doubled to generate laser light at 411 nm. A double-pass AOM is used for frequency shifting and for pulse generation. The quadrupole transition beam goes vertically through the ion trap. To achieve a clean polarization of the beam, it is equipped with a combination of wave plates and a polarizing beam splitter cube.

This setup also counteracts the birefringence of mirror coatings and of the vacuum viewport.

4.3.3. Ion Imaging

For imaging of the ion fluorescence, a self built objective with a working distance of 31 mm and numerical aperture $NA \approx 0.27$ was used. The objective consists out of five lenses [30] and is placed on the air side of the re-entrant viewport (see Fig.4.1). This allows to move the objective with three perpendicular translation stages. The movement along the trap axis and the focus position can be adjusted with motorized actuators¹¹, which allows to move the objective to different trap segments in a few seconds.

With a moveable slider, the fluorescent light was guided either to a photomultiplier tube (PMT)¹² or to an electron-multiplying CCD (EMCCD)¹³. A beam splitter also allowed to use both detection signals at the same time. In order to reduce stray light to a minimum, a narrow band filter was inserted into the imaging beam path. Additionally, a movable slit aperture was put in front of the PMT.

At the used ion-objective distance, the magnification of the objective was measured to be 24.4. With a pixel size of the EMCCD camera of 16 μm , this results in a theoretical resolution of 656 nm and a field of view of 336 μm . The optical resolution as determined by the FWHM of the image of a single ion was measured to be approximately 2 μm .

4.4. Sideband Spectroscopy Sequence

This section explains the different phases of the experimental sideband spectroscopy sequence using the $^2S_{1/2} \leftrightarrow ^2D_{5/2}$ quadrupole transition. One of the main objectives of this sequence is to cool an $^{172}\text{Yb}^+$ ion to the ground state via the resolved sideband cooling technique. The ability to monitor and keep the wavelength of the 1650 nm laser at the desired frequency allowed to implement a continuous sideband cooling scheme (see Sec. 2.4.2). Each step of the experimental cycle is described briefly.

4.4.1. Selection Rules for Quadrupole Transitions

The applied external magnetic field of $B = 65 \mu\text{T}$ leads to a Zeeman splitting of the ground state $^2S_{1/2}$ and the excited state $^2D_{5/2}$ sublevels. The splitting magnitude and the resulting spectrum of the quadrupole transition are illustrated in Fig. 4.11. The

¹¹Zaber T-LA28A

¹²Hamamatsu, R7207-01, Bi-alkali window

¹³Andor iXon EM+ DU-897D-CS0-UVB

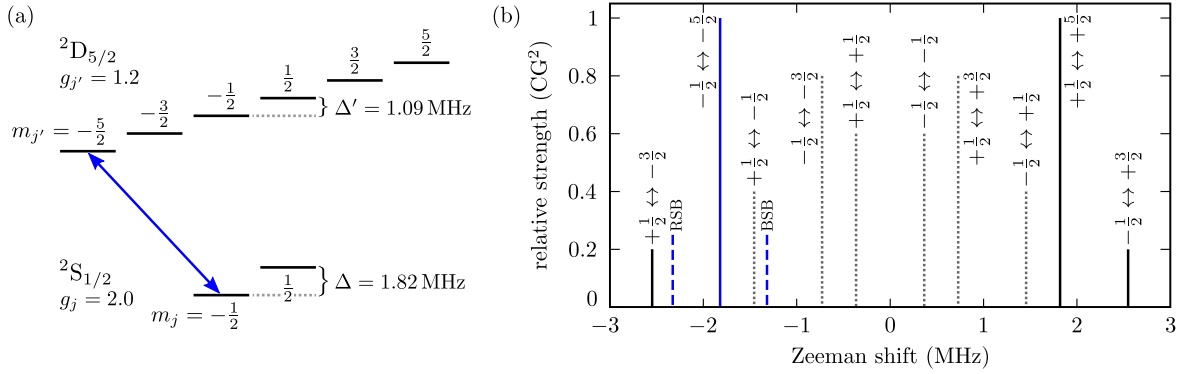


Figure 4.11.: Zeeman splitting of the of the $2S_{1/2} \leftrightarrow 2D_{5/2}$ quadrupole transition in the experimentally used magnetic field of 65 μ T. (a) Term scheme showing all Zeeman states of the quadrupole transition. For spectroscopy and sideband cooling the transition $m_j = -\frac{1}{2} \leftrightarrow m_{j'} = -\frac{5}{2}$ is used. (b) Resulting spectrum of transitions between all Zeeman sublevels relative to the unperturbed transition and their relative strength according to the squared Clebsch-Gordan coefficients. The chosen orientation of the magnetic field vector \vec{B} , the beam axis and the polarization only allows transitions with $\Delta m = \pm 2$ (blue and black solid lines). The blue dashed lines indicate the frequencies of the first red and blue sideband of the $m_j = -\frac{1}{2} \leftrightarrow m_{j'} = -\frac{5}{2}$ transition.

transition strength Ω_{E2} between each of the Zeeman sublevels depends on the choice of the orientation of the polarization and the laser beam direction relative to the quantization axis, which is defined by the external magnetic field vector \vec{B} . According to James [53] the Rabi frequency Ω_{E2} of the quadrupole transition is given by

$$\Omega_{E2} = \frac{eE_0}{\hbar\sqrt{c\alpha}} \sqrt{\frac{45A}{2k^3}} \left| \sum_{q=-2}^2 \begin{pmatrix} 1/2 & 2 & 5/2 \\ m_j & \Delta m & -m_{j'} \end{pmatrix} c_{ij}^{\Delta m} \epsilon_i n_j \right|, \quad (4.6)$$

where E_0 denotes the electric field amplitude of the laser, α the fine structure constant and A is the Einstein coefficient. The term in the round brackets are the Wigner 3-j symbols. The geometry-dependent part is given by the second rank tensors $c_{ij}^{\Delta m}$ and the unit vectors $\vec{\epsilon}$, \vec{n} , that represent the orientation of the polarization \vec{E} and of the laser beam \vec{k} , respectively. The explicit expressions for the tensors $c_{ij}^{\Delta m}$ can be found in [53]. A graphical representation of the dependence of the transition strength on the selected geometry can be found in [83]. In the experiment, \vec{B} , \vec{E} and \vec{k} are selected to be mutually orthogonal. \vec{B} is pointing in the direction of the H2 beam and \vec{k} is going vertically through the ion trap (see Fig. 4.7). With this arrangement, only transitions with $\Delta m = \pm 2$ can be excited. After optical pumping to the $2S_{1/2}(m_j = -\frac{1}{2})$ state only two possible transitions remain. Those are $m_j = -\frac{1}{2} \leftrightarrow m_{j'} = -\frac{5}{2}$ and $m_j = -\frac{1}{2} \leftrightarrow m_{j'} = +\frac{3}{2}$. For the experiments the former is selected, because of its larger transition strength and because it has the lower frequency, which reduces the risk of off-resonant excitation on the blue sideband of other transitions (see Fig. 4.11).

With this geometric selection, the quadrupole transition is effectively reduced to a two-level system. Inserting $m_j = -\frac{1}{2}$, $\Delta m = -2$, $m_{j'} = -\frac{5}{2}$ and the chosen geometry into

4. Experimental Setup and Sideband Spectroscopy Sequence

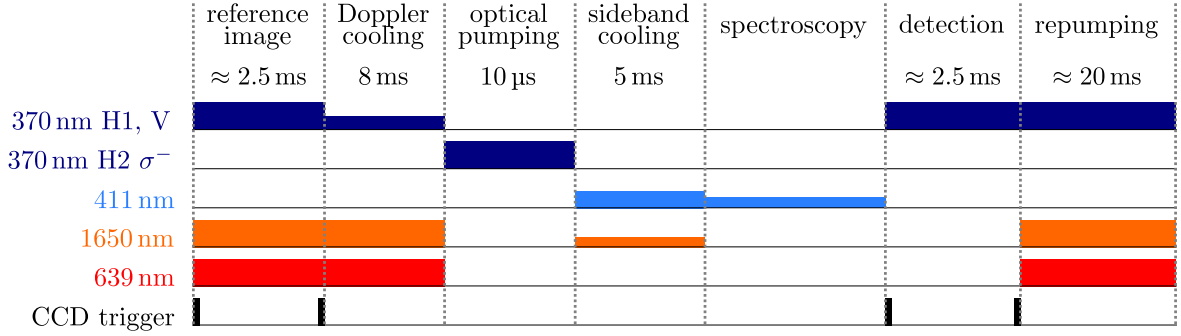


Figure 4.12.: Experimental sequence used for continuous sideband cooling.

Eq. 4.6, the term inside the absolute value bars gives a factor $\frac{1}{6}$ and the quadrupole Rabi frequency for the transition $m_j = -\frac{1}{2} \leftrightarrow m_{j'} = -\frac{5}{2}$ becomes

$$\Omega_{E2} = \frac{eE_0}{\hbar} \sqrt{\frac{5\lambda^3 A}{64\pi^3 c\alpha}}. \quad (4.7)$$

With the available power $P_{411\text{ nm}} = 1.8\text{ mW}$ and a beam waist of $70\ \mu\text{m}$, the achievable Rabi frequency is $\Omega_{E2} = 2\pi \times 141\text{ kHz}$.

4.4.2. Ground State Cooling Sequence

The used experimental sequence that was implemented for continuous ground state cooling is schematically shown in Fig. 4.12. Before starting this sequence, the trap voltages have been adjusted such that one radial trap axis is oriented vertically along the y -axis (see Fig. 4.7). Additionally, the magnetic field is adjusted to point into the H2 beam direction and with a motorized quarter wave plate, the H2 beam polarization is changed from linear to circular polarization. These two steps make sure to have a pure σ^- polarization for the optical pumping. The experiment is repeated for each parameter set 200 times in order to have the needed statistics on ground state and excited state population.

Reference Image and Detection

Each experimental sequence is started with a trigger signal at the same phase of the mains voltage to suppress fluctuations due to 50 Hz noise. At first, a reference image is recorded in order to confirm that the ion is initially in the ground state. Therefore, all repumpers and the Doppler cooling laser are switched on and the camera is triggered to start and to end the exposure. At the end of the experimental cycle, the camera is triggered again for the electron shelving state detection [44]. Here, only the Doppler cooling light is switched on, because excited ions should stay in the excited state and not be pumped back to the ground state during detection.

Although only a single ion has been used in all experiments, the EMCCD camera was used for the detection. This was done as preparation for the future plan to detect multiple ions simultaneously. For the detection, the count rate of a region of interest of typically 4×4 pixels was evaluated. A fixed threshold value has been defined. All images with count rates above the threshold are counted as ‘bright’, which corresponds to ground state population. Otherwise the images are counted as ‘dark’, which correspond to population of the $^2D_{5/2}$ state. All cycles with a ‘dark’ reference image have been discarded and not been used for the further evaluation, because the initial state preparation is not ensured.

The exposure time used for detection is a trade off between a clear differentiation of bright and dark images and unwanted spontaneous decay from the excited state back to the ground state. Such decays during the detection period reduce the contrast of the state detection. Typically a detection time of 2.5 ms has been used. The differentiation between bright and dark images had a fidelity of 99.7%. This number does not include the error due to decay from the excited to the ground state. From the given decay rates of the $^2D_{5/2}$ state it is assumed that the excited state population is reduced by approximately 2.7% due to decay during the detection period.

Doppler Cooling

For detection, the maximum available intensity at 370 nm is used to achieve maximum count rates. For the subsequent Doppler cooling phase the intensity is significantly reduced to achieve the lowest possible temperature. The intensity, the frequency and the Doppler cooling period of 8 ms have been optimized with subsequent recording of Rabi oscillations on the carrier transition. From the observed Rabi frequency and contrast also the achieved temperature can be inferred as described in [58]. Typically, the achieved temperature is close to the Doppler cooling limit of 0.47 mK (see Eq. 2.49).

Optical Pumping

In the following step the ion is optically pumped to the $^2S_{1/2}(m_j = -\frac{1}{2})$ ground state. Therefore, the σ^- polarized light of the H2 beam is used. Perfectly polarized light only drives the transition $^2S_{1/2}(m_j = +\frac{1}{2}) \leftrightarrow ^2P_{1/2}(m_{j'} = -\frac{1}{2})$ with $\Delta m = -1$ and the desired $^2S_{1/2}(m_j = -\frac{1}{2})$ state becomes a dark state. The optical pumping has been optimized either by minimizing the scattering rate on the Doppler cooling transition or by minimizing the observed excitation on the $^2S_{1/2}(m_j = +\frac{1}{2}) \leftrightarrow ^2D_{5/2}(m_{j'} = +\frac{5}{2})$ transition. The parameters that need to be optimized are the rotation and the tilt angles of the 370 nm quarter waveplate and the pointing of the magnetic field vector.

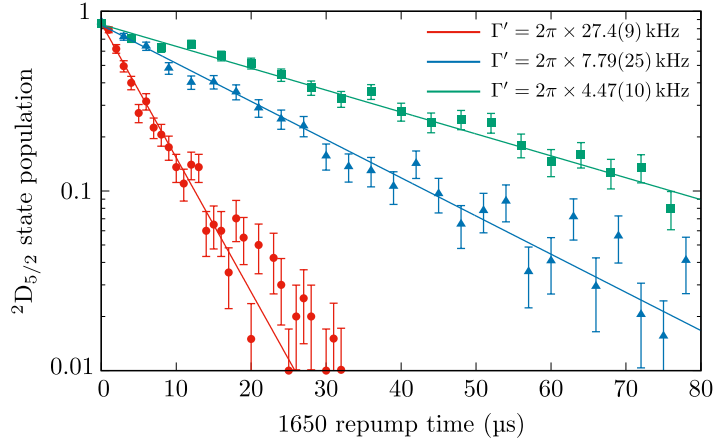


Figure 4.13.: Results of the decay rate measurements for three different laser intensities. The shown lines are simple exponential decay functions fitted to the respective data. The decay rates given in the legend are results from these fits.

Sideband Cooling

For sideband cooling the 411 nm laser is tuned to the first red sideband transition (RSB) and simultaneously the repumper at 1650 nm is illuminating the ion. Both lasers are switched on continuously for 5 ms. The ion is cycling between the Zeeman states ${}^2S_{1/2}(m_j = -1/2) \leftrightarrow {}^2D_{5/2}(m_j = -5/2) \leftrightarrow {}^2P_{3/2}(m_j = -3/2)$. Because of the respective selection rules, this is a closed cycle. As explained in Sec. 2.4.2, this scheme results in an effective two-level system with a dressed excited state with a tunable decay rate Γ' . As denoted in Eq. 2.51, the new decay rate can be adjusted by changing the Rabi frequency of the ${}^2D_{5/2} \leftrightarrow {}^2P_{3/2}$ transition or by changing the detuning of the 1650 nm laser. Here the repumper is tuned to the ${}^2D_{5/2} \leftrightarrow {}^2P_{3/2}$ resonance (see Fig. 4.10 and Sec. 4.3) and the Rabi frequency is adjusted by changing the laser intensity.

The decay rate of the dressed excited state has been directly observed in a separate measurement. For this, the experimental cycle shown in Fig. 4.12 has been modified. After Doppler cooling, a π -pulse on the ${}^2S_{1/2} \leftrightarrow {}^2D_{5/2}$ carrier transition is added to transfer the population to the ${}^2D_{5/2}$ state. Subsequently, a pulse at the 1650 nm transition with variable pulse length is sent to the ion. This is followed by the usual electron shelving state detection on the Doppler cooling transition. Fig. 4.13 shows the results of some of these measurements performed at three different laser intensities at 1650 nm. The laser power used for those measurements is in the range of a few hundreds of nW. For the sideband cooling sequence the decay rate $\Gamma' = 2\pi \times (7.79 \pm 0.25)$ kHz has been chosen as a good compromise between cooling rate and final temperature.

The only optimization to the continuous sideband cooling pulse was to reduce the power of 411 nm laser to approximately 0.2 mW. This reduces the effective cooling

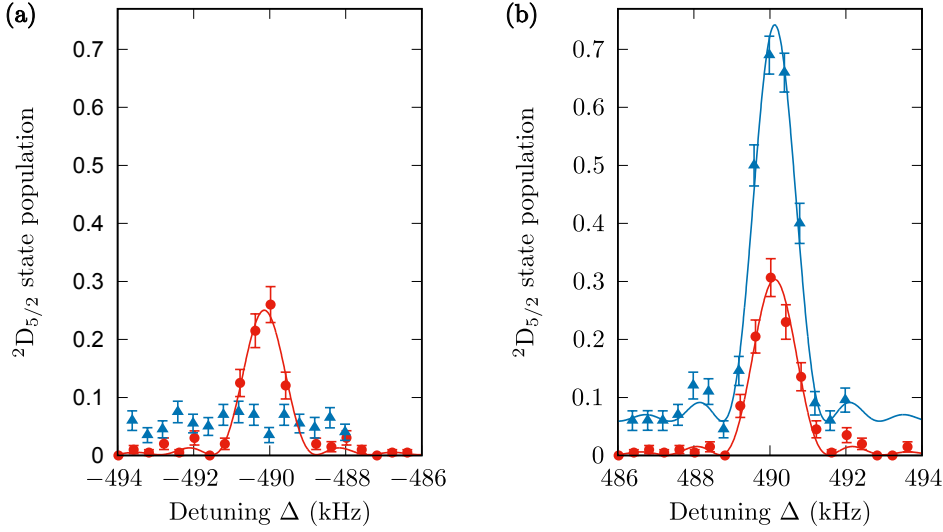


Figure 4.14.: Excitation spectrum on the first (a) red sideband and (b) blue sideband of the ${}^2S_{1/2} \leftrightarrow {}^2D_{5/2}$ quadrupole transition. The red circles have been measured directly after the Doppler cooling phase. The blue triangles have been recorded after continuous sideband cooling. The blue data points have been corrected for a small drift of the carrier frequency of about 4.8 kHz. The lines are squared sinc functions fitted to the data points.

rate, but also helps to reduce off-resonant excitation of unwanted quadrupole transitions. As described in [58], the high frequency noise of the spectroscopy laser is causing the observed off-resonant excitation. Especially the transition ${}^2S_{1/2}(m_j = -1/2) \leftrightarrow {}^2D_{5/2}(m_j = +3/2)$ needs to be suppressed, because it is likely to decay into the ${}^2S_{1/2}(m_j = +1/2)$ state. There, the ion will not be cooled any more and will not be excited in the subsequent spectroscopy pulse. As a result, this will increase the background of state detection measurements.

Sideband Spectroscopy and Temperature Determination

After sideband cooling, a light pulse on the quadrupole transition is sent to the ion. This pulse can vary in duration, frequency and light intensity. E.g. a pulse with a frequency fixed to the carrier transition with maximum intensity and scanning of the pulse duration would allow to record Rabi oscillations and to measure the achieved Rabi frequency. This can be used to calculate the 411 nm light intensity that is seen by the ion via Eq. 4.7.

Sideband spectroscopy also has been used to measure the mean phonon number \bar{n} after ground state cooling. Therefore, the excitation probability on the first blue sideband transition I_{BSB} is compared to the excitation probability on the first red sideband transition I_{RSB} . For both probe pulses the same 411 nm laser intensity and

pulse duration has to be used. As derived e.g. in [58, 84] under this condition the probabilities can be used to determine the mean phonon number with

$$\bar{n} = \frac{1}{\frac{I_{\text{BSB}}}{I_{\text{RSB}}} - 1}. \quad (4.8)$$

A result of the measurement of the excitation probabilities after Doppler and after sideband cooling are shown in Fig. 4.14. The excitation probability has been determined by fitting of squared sinc functions to the data points. After sideband cooling, the excitation of the RSB could not be distinguished any more from the background. The increased background that is observed after the sideband cooling pulse is attributed mainly to off-resonant excitation during the sideband cooling phase. As a worst case scenario, it has here been assumed that I_{RSB} equals the maximum difference of the measured data points near the RSB. With this definition, a mean phonon number after continuous sideband cooling of $\bar{n}_{\text{sbc}} = 0.06 \pm 0.03$ is calculated.

The method is less suitable to measure higher temperatures with $\bar{n} \gg 1$. From Eq. 4.8 it is seen that for large values of \bar{n} both probabilities are of equal size $I_{\text{RSB}} \approx I_{\text{BSB}}$. Hence only small errors on the determination of one of the two probabilities will produce a large error in \bar{n} . After Doppler cooling a temperature close to the Doppler cooling temperature of $T_D = 0.47$ mK (see Eq. 2.50) is expected. This corresponds to a mean phonon number of

$$\bar{n} = \frac{k_B T_D}{2\hbar\omega_{\text{sec}}} - 1/2 \approx 9.3. \quad (4.9)$$

From the amplitudes as shown in Fig. 4.14, the mean phonon number of $\bar{n}_{\text{Doppler}} = 4.7 \pm 2.2$ has been determined. This shows that in this higher temperature range the temperature or at least its error is underestimated. For a more reliable measurement of the ion temperature at larger values of \bar{n} , higher order sidebands can be used. Alternatively the sideband amplitudes can also be compared to the carrier transition probability as discussed in [85, 86]. Another approach that determines the temperature from measured Rabi oscillations is discussed in [58].

Repumping

The last step of the experimental cycle that was used for ground state cooling, is to bring the state population back to the $^2\text{S}_{1/2}$ ground state. Therefore, all repumping lasers and the Doppler cooling light is illuminating the ion. Compared to the description in [58], the laser power at 638 nm could be increased from 4.6 mW to 22 mW which helps to deplete the $^2\text{F}_{7/2}$ state faster. Also the additional power broadening helps to address all Zeeman sublevels of the $^2\text{F}_{7/2}$ state. The repumping rates have not been characterized in detail, but the number of ‘bright’ reference images indicated that the 20 ms repump time are sufficient to come back to the ground state.

5. Ion Trap Characterization

The ion trap main properties have been determined by a series of measurements that are discussed in this chapter. It starts with a description of the trap temperature measurements performed with three different ion traps. This is followed by measurements of the secular frequencies in dependence of the trap dc and rf voltages. The third and fourth section details on the measurement of micromotion amplitudes and the results of the heating rate measurements, respectively.

5.1. Temperature of the Ion Trap

This section discusses simulations and measurements that were performed to deduce the temperature rise ΔT of three slightly different traps due to the applied rf voltage. General considerations on the heating sources and on how the trap design and materials influence the trap temperature rise have been discussed in section 3.4. The target of the trap temperature measurements and of the simulations is to find the temperature of the black-body radiation at the position of the ions. This temperature will finally determine the electric field strength of the black-body radiation which induces the BBR frequency shift (see Eq. 2.62). The temperature at the ion position does not coincide with the trap temperature because the emissivity of the surfaces is below unity, which reduces the amount of black-body radiation that is emitted. The temperature at the position of the ion can therefore only be determined by simulations or by direct measurements of the associated frequency shift. All results presented in this section have been obtained in a collaboration with the Czech Metrology Institute (CMI). Trap II and trap III have been brought to CMI to Petr Balling and Miroslav Doležal in order to perform infrared camera measurements. Also, all simulations of the trap temperature have been carried out by Miroslav Doležal from CMI. The measurements and simulations of trap II have been published in Ref. [76].

The main differences between the three investigated traps are listed in Tab. 5.1. Besides the thickness of the gold layer, trap III and trap IV are identical. After the temperature measurements of trap II, it was possible to introduce a couple of improvements to the trap manufacturing process of those two ion traps. The measurements in [76] showed that thin gold layers (thickness below $1\ \mu\text{m}$) lead to additional resistive heating and have to be avoided. On trap II, these thin gold layers have been present due to a insufficient masking of the trap during the sputtering process. For trap III and IV these unwanted areas with gold coating have been identified by optical inspection

trap number	gold thickness	spacers	support board
II	4.5 μm ; gold layer is sporadically peeling off	lapped surfaces $R_a = 640 \text{ nm}$ $t_{\text{PK}} = 0.254 \text{ mm}$	thickness 1.0 mm glued to PK1 via alignment holes
III	PK wafer 4.5 μm PRF wafer 2.5 – 3 μm	polished surfaces $R_a = 50 \text{ nm}$ $t_{\text{PK}} = 0.128 \text{ mm}$	thickness 1.5 mm glue applied to whole contact area of PK1
IV	4.5 μm	polished surfaces $R_a = 50 \text{ nm}$ $t_{\text{PK}} = 0.128 \text{ mm}$	thickness 1.5 mm glue applied to whole contact area of PK1

Table 5.1.: Main differences between the three different traps whose temperature behaviour has been investigated. The trap numbers are correspond to the denomination in Tab. 3.4. R_a is a value for the surface roughness and t_{PK} is the thickness of the spacers between PK and PRF chips (see Fig. 3.1).

and have been removed by laser ablation. In addition, the results of trap II made clear that the thermal contact resistivity between the different AlN wafer can limit the total thermal conductivity which is needed to transport the produced heat to the vacuum chamber. To improve the thermal contact conductivity, polished spacers have been used. Because of the lower surface roughness compared to a lapped surface, it is expected that the effective contact area to the AlN wafer is increased. Also the contact surfaces have been cleaned carefully before the assembly of the trap stack. Any particle in between the contact areas would lead to a reduced thermal contact conductivity. Additionally, for trap III and IV, glue was applied to the whole contact area between the PK1 wafer and the support board. The glue acts as a thermal compound and helps to increase the thermal contact conductivity. Additionally, trap II did have an insufficient gold layer adhesion to the AlN substrate and as a result the gold layer peeled off on some small spots. Because of the small size of the spots compared to the total gold area, it is not expected that this flaw has a significant influence on the trap heating.

Experimentally, the temperature of the trap has been measured by two Pt100 sensors or with an infrared camera¹ through a Zinc Selenide (ZnSe) vacuum viewport. The Pt100 sensors are located on the two PRF wafer (see Fig. 3.3) and thus can only measure local temperatures. To reduce the absolute uncertainty of the temperature measurement, the sensors have been calibrated. The calibration procedure and results for trap IV are described in the appendix A.4. With the calibration, an absolute temperature uncertainty of 50–60 mK is achieved, while the temperature resolution is below 1 mK. The Pt100 sensors of the other two traps have been calibrated with similar setups at

¹FLIR A615, spectral sensitivity 7–13 μm

trap number	PRF2 heated R_{th} (K/W)	PRF3 heated R_{th} (K/W)
II	9.75	10.28
III	6.22	6.34
IV	6.63	6.54

Table 5.2.: Values of the measured effective thermal resistances R_{th} . The uncertainties of all values are approximately $\sigma_{R_{\text{th}}} = 0.02 \text{ K/W}$.

CMI. Rf heating of the sensors has been prevented by placing two capacitors directly beneath each temperature sensor. In order to observe temperature gradients across the whole trap, the IR camera measurements have been used. The temperatures measured with the IR camera images are corrected for the effective emissivity of the observed material and for losses due to the ZnSe viewport. The temperature uncertainty of the IR camera measurement is $\sigma_{T,\text{cam}} = 0.2 \text{ K} + 0.05 \Delta T$, where ΔT is the observed temperature rise in Kelvin. More details about the determination of emissivity values of different materials and the measurement with the IR camera can be found in [76]. Within this work, only the temperature increase ΔT of the trap has been measured. This describes the difference of the steady state temperature that is measured with the applied rf voltage to the steady state temperature without any rf voltage. For a full characterization of the temperature distribution around the ion, also the temperature of the vacuum chamber needs to be measured and controlled. Due to the relatively low thermal conductivity of steel and titanium commonly used to build vacuum vessels, also significant gradients can exist. In Ref. [76] it has been shown that the electrical feedthrough used for the rf voltage heats up and can introduce such temperature gradients across the vacuum chamber.

The trap temperature increase is determined by the heat production due to the applied rf voltage on one side and the removal of the heat via conduction and radiation on the other side. In order to separate these two phenomena experimentally, a known amount of heat has been introduced via a dc current to one of the Pt100 sensors while the other sensor has been used to measure the temperature rise. An effective thermal resistance of the whole trap can be deduced by deriving the ratio $R_{\text{th}} = \frac{\Delta T}{P}$, where P is the heat power introduced via one Pt100 sensor and ΔT is the temperature rise measured with the other sensor. Table 5.2 shows the effective thermal resistances of all three traps. The numbers show that for each trap there is only a small difference if the sensor used for heating is changed. It can also be seen that the thermal resistances of trap III and trap IV are similar and they are approximately a factor 0.65 smaller than the resistance of trap II. This shows that the design changes could increase the thermal contact conductivities and also shows that this is reproducible. By corresponding simulations these values have been used to determine thermal contact conductivities between the trap chips and the spacers. For trap II a value of $1000 \text{ W}/(\text{m}^2 \text{ K})$ have been found. For ion trap III and IV this could be increased to $1500 \text{ W}/(\text{m}^2 \text{ K})$.

trap number	U_{rf} (V)	$\Omega_{\text{rf}}/2\pi$ (MHz)	ΔT_{PRF2} (K/kV ²)	ΔT_{PRF3} (K/kV ²)
II	500	15.41	1.85	2.03
II	1000	15.41	2.51	2.86
III	708	7.53	0.14	0.16
III	1000	15.77	0.63	0.82
III	1017	21.41	1.22	1.55
IV	794	24.38	0.78	1.21

Table 5.3.: Observed temperature rises measured with the two Pt100 sensors rescaled to a rf voltage amplitude of $U_{\text{rf}} = 1$ kV. Because the trap heating has been measured at different drive frequencies Ω_{rf} the results cannot be compared directly.

In the next step, the rf voltage has been applied to the trap and the resulting temperature rise was measured using the Pt100 sensors on the trap wafers PRF2 and PRF3. Table 5.3 shows the results of these measurements. Because the two heating sources (see Eq. 3.1 and 3.2) scale quadratically with the rf voltage amplitude U_{rf} , also the resulting temperature increase scales quadratically with the drive voltage amplitude. This behaviour has been confirmed by the measurements as shown in Fig. 5.1 (a). For better comparability, all measured temperature increases are rescaled to a trap voltage of 1 kV. For trap II the trap heating followed the quadratic dependency up to a trap voltage of 500 V and increased faster for higher voltages. This can be seen by the fact that the scaled temperature increase measured at 500 V is lower than the values measured at 1 kV. The additional heating is attributed to a contamination of the trap wafers, which is probably caused by outgassing of heat-conductive paste used in the test vacuum chamber [76]. It was possible to remove some contamination and to decrease the rf heating by cleaning the trap wafers with acetone.

In contrast to the scaling of the temperature rise with the rf voltage there is no simple scaling rule for the rf frequency Ω_{rf} . This makes a comparison of temperature increases measured at different rf frequencies more difficult. There are three main heating sources that are expected to show different frequency dependencies. From Eq. 3.2 it is seen that dielectric losses scale linearly with the rf frequency. It is assumed that the relative permeability ε_r and the loss tangent $\tan(\delta)$ are constant within the considered frequency band. For the resistive losses (see Eq. 3.1), the frequency dependency of the current I and of the resistance R has to be taken into account. Because electrically, the ion trap is a capacitive load, its impedance is $Z = (i\Omega_{\text{rf}}C)^{-1}$, and we receive for the current amplitude $I \propto U_{\text{rf}}\Omega_{\text{rf}}C$. In addition, the effective conductor resistance is also frequency dependent because of the skin effect. Via integration over the current density in a conductor, the frequency dependency is found to be

$$R(\Omega_{\text{rf}}) \propto \frac{1}{\delta(\Omega_{\text{rf}}) (1 - \exp(-d/\delta(\Omega_{\text{rf}})))}, \quad (5.1)$$

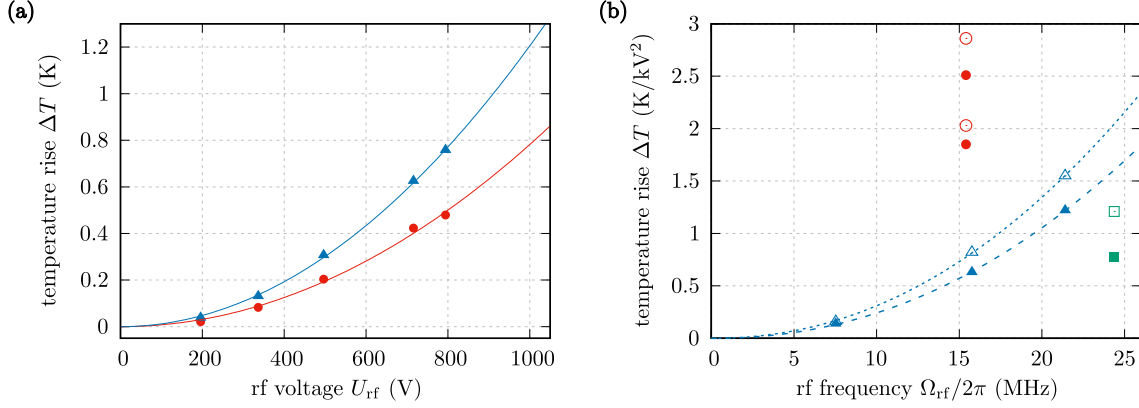


Figure 5.1.: (a) Observed temperature rise of trap IV as a function of U_{rf} . Red dots (blue triangles) show the temperature rise measured with the Pt100 sensor on PRF2 (PRF3). The lines are purely quadratic fits to the data points. The uncertainties of U_{rf} and of the temperature rise are on the order of the dot sizes. (b) Observed temperature rises rescaled to an rf voltage of 1 kV for trap II (red dots), trap III (blue triangles) and trap IV (green squares) as a function of the rf frequency Ω_{rf} . Closed symbols correspond to ΔT_{PRF2} and open symbols show ΔT_{PRF3} . The dashed and dotted line show the expected frequency scaling behaviour for trap III.

where $\delta(\Omega_{\text{rf}}) = \sqrt{\frac{2\rho}{\Omega_{\text{rf}}\mu}}$ is the skin depth and d is the thickness of the conductor. Here, ρ is the resistivity of the conductor material and $\mu = \mu_0\mu_r$ is the permeability. Thus, the total frequency dependency of the resistive heating is given by (compare Eq. 3.1)

$$P_{\text{res}}(\Omega_{\text{rf}}) \propto \frac{\Omega_{\text{rf}}^2}{\delta(\Omega_{\text{rf}}) [1 - \exp(-d/\delta(\Omega_{\text{rf}}))]} . \quad (5.2)$$

For $d \gg \delta(\Omega_{\text{rf}})$ the exponential term can be neglected and $P_{\text{res}} \propto \Omega_{\text{rf}}^{2.5}$. The skin depth at $\Omega_{\text{rf}} = 2\pi \times 24.38$ MHz is $\delta = 15.3 \mu\text{m}$. Therefore, in the experiment this condition is met for the copper stripes ($d = 100 \mu\text{m}$) connecting the electrical feedthrough to the trap rf electrodes. In the other case $d < \delta(\Omega_{\text{rf}})$ the skin effect can be neglected and $P_{\text{res}} \propto \Omega_{\text{rf}}^2$. In the experiment this is the case for trap electrodes with a thickness of $d \approx 4 \mu\text{m}$. In total the frequency dependence of the trap temperature rise can be described by

$$\Delta T = a_1 \Omega_{\text{rf}} + a_2 \Omega_{\text{rf}}^2 + a_3 \Omega_{\text{rf}}^{2.5} . \quad (5.3)$$

The coefficients $a_{1,2,3}$ are determined by the magnitude of the three discussed heating sources. Due to the differences of the investigated traps as listed in Tab. 5.1, it is expected that each trap has different coefficients.

As listed in Tab. 5.3 the trap heating of the three traps has been measured at different frequencies and for a comparison the frequency scaling needs to be taken into account. In Fig. 5.1 (b) the measured trap temperatures from Tab. 5.3 are plotted as a function of the measured frequency. Only for trap III measurements have been made at different rf frequencies. Based on the simulation results it has been assumed that for this trap the resistive loss in the conductors is the dominant heating source. Therefore, the

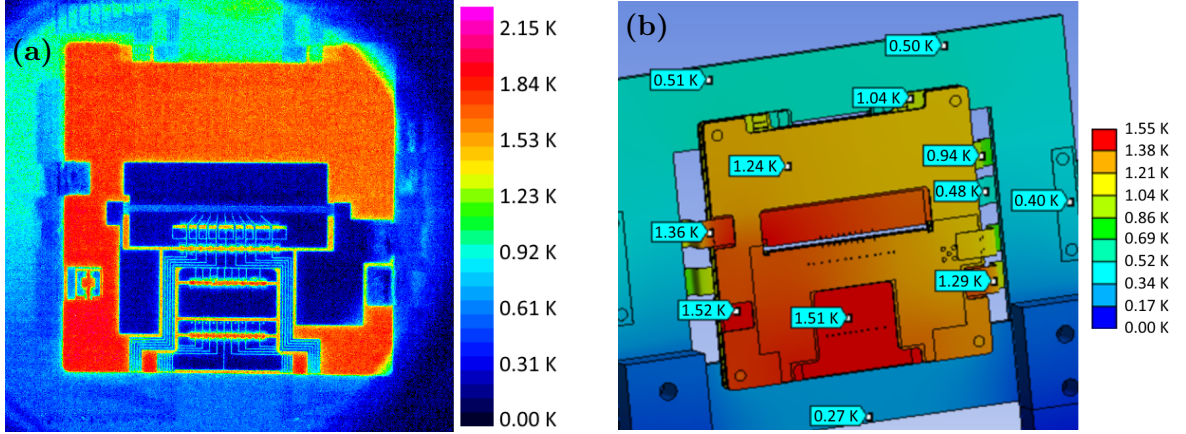


Figure 5.2.: (a) IR camera measurement of trap III at $\Omega_{\text{rf}} = 2\pi \times 21.5$ MHz and $U_{\text{rf}} = 1.5$ kV. Shown is a differential image, where a cold image (rf off) has been subtracted from the hot image (rf on). The scale has been rescaled to 1 kV and includes corrections for the AlN emissivity and the vacuum viewport transmission. (b) Simulation result for trap IV at $\Omega_{\text{rf}} = 2\pi \times 24.38$ MHz and $U_{\text{rf}} = 0.5$ kV. The indicated temperature rises and the scale have been rescaled to 1 kV for a better comparability.

function $\Delta T(\Omega_{\text{rf}}) = a\Omega_{\text{rf}}^b$ has been fitted to the data with fit parameters a and b . The fit resulted in $b_{\text{PRF2}} = 2.13 \pm 0.05$ and $b_{\text{PRF3}} = 2.12 \pm 0.05$. The plot shows that the fit agrees well with the measured data. The scaling exponents confirm that resistive losses are the dominant source of heating. The diagram shows that trap II exhibits the highest temperature increase of the investigated traps. The temperature increase of trap III measured at a similar frequency is about a factor 2.5 to 4 lower. The estimated frequency scaling of trap III allows a comparison to trap IV at $\Omega_{\text{rf}} = 2\pi \times 24.38$ MHz. At this frequency it is expected that the temperature increase of trap IV is a factor 1.7 to 2.1 lower as for trap III. The comparisons show that the changes to the trap design of the ion traps III and IV are effectively reducing the temperature increase. Furthermore from the observed difference between trap III and IV it can be concluded that a thicker gold layer is significantly reducing the trap temperature.

For the simulation the ANSYS FEM software package has been used. The trap temperature has been modelled in two steps. In the first step the heat introduced by the rf voltage has been calculated with an electrodynamic model. In the second step the resulting steady-state temperature distribution was derived. In order to determine the temperature at the ion position, a small sphere with unity emissivity has been added at the location of the ions. The temperature of this sphere is used to sample the black-body radiation temperature. A more detailed description of the FEM analysis can be found in Ref. [76].

The temperature increase predicted by the FEM simulation is determined by a number of physical parameters. The main parameters are the emissivities of the trap and vacuum chamber surfaces, the thermal contact conductivities between the trap wafers and of the connections to the trap mounts and the vacuum chamber, the electrical con-

ductivity of the gold layer, the thickness of the gold coating, the rf voltage amplitude and the loss tangent $\tan \delta$ of the AlN wafer. The emissivity values have been measured using the IR camera as discussed in detail in Ref. [76]. The thermal contact conductivities have been determined by the heating with the Pt100 sensors as described above. The electrical conductivity of the sputtered gold layers has been measured through 4-wire-measurements and have been found to be $\rho = (26 \pm 5) \times 10^6 \text{ S m}^{-1}$ which is a factor 1.7 lower than textbook values for bulk material. The gold coating thicknesses have been measured on selected locations for all wafer using a tactile profilometer. The applied rf voltage amplitude is determined by the pickup voltage and a calibration factor (see Secs. 4.2 and 5.2 for more details). The loss tangent of the used AlN material is known from the supplier data sheet (see Appendix A.2), but also has been used to match the simulation results with the observed temperature increases. As described in [76], for trap II it was necessary to increase the loss tangent to $\tan \delta = 8 \times 10^{-4}$ to account for the additional heating caused by contamination of the ion trap. For trap III and IV it was found that the loss tangent has to be reduced to 5×10^{-5} in order to match the simulations to the observed temperatures. As the data sheet values are typically measured in air it could be that the vacuum leads to a reduction of the dielectric losses. A possible explanation of such an effect could be that water molecules that are adsorbed to the surface in air evaporate under vacuum conditions. To proof this assumption a series of measurements would be necessary.

Comparisons to the IR camera measurements of trap II and III have been used to verify the simulation results. Fig. 5.2 (a) shows the IR camera measurement of trap III. The view on the trap is limited by the size of the ZnSe vacuum viewport. It is seen that all gold surfaces appear to be colder than the AlN wafer. Because of the much lower emissivity of gold ($\varepsilon_{\text{Au}} = 0.05$ and $\varepsilon_{\text{AlN}} = 0.78$), the electrodes emit less thermal radiation. The temperature scale of the image includes correction factors for the emissivity of the AlN and for the vacuum viewport transmission. Thus only the temperature of the visible AlN surface is shown correctly. Besides these corrections, reflections of thermal radiation that are imaged with the IR camera are another error source. The influence of the reflections is suppressed by determining the local temperature rise instead of the absolute temperature. However, an increased amount of reflections due to the increased temperature of the trap cannot be detected. This could lead to an overestimation of the temperatures measured with the IR camera.

The simulation result for trap IV is shown in Fig. 5.2 (b). For the simulation, an rf voltage amplitude of $U_{\text{rf}} = 500 \text{ V}$ was used. In the image the temperature increase has been rescaled to a voltage of 1000 V assuming a quadratic voltage dependency. The IR image and the simulation both show a temperature gradient across the visible PK4 wafer. The highest temperature rise is observed in the lower left corner and the lowest temperature is located in the upper right corner of the PK4 wafer. A more detailed comparison shows that maximum local deviation for the temperature increase between the IR measurements and the simulation are 0.4 K/kV^2 for trap II and 0.42 K/kV^2 for trap III. A possible reason for this observation is that the thermal contact conductivities

5. Ion Trap Characterization

trap number	ΔT_{PRF2} (K/kV ²)	ΔT_{PRF3} (K/kV ²)	A	B	ΔT_{ion} (K/kV ²)
II	2.51 ± 0.41	2.86 ± 0.41	0.40 ± 0.10	0.35 ± 0.10	1.01 ± 0.22
IV	0.78 ± 0.43	1.21 ± 0.43	0.43 ± 0.10	0.32 ± 0.10	0.36 ± 0.13

Table 5.4.: Temperature rise seen by the ions for trap II and IV at $U_{\text{rf}} = 1$ kV. The error estimations of the values are described in the main text. The temperature rise ΔT_{ion} and its uncertainty increase quadratically with the rf voltage amplitude.

will be different for every contact surface, whereas in the simulation are all set to the same value. Also, the gold thickness measurements show gradients for all wafers. The observed thickness deviations from the mean value are on the order of ± 1 μm . These deviations will lead to spacial fluctuations of the resistive heat production which are not captured in the FEM model. The simulation also allows to identify the dominant heat sources. For trap II [76] the dominant heat source is the dielectric loss in the AlN wafer or respectively the loss due to the trap contamination. These losses account for 72 % of the total losses. In contrast, for trap IV the resistive losses of the gold coating are dominant and contribute with 52 % to the total losses.

The main purpose of the simulations is to define a relationship between the temperature rise measured with the Pt100 sensors to the temperature increase at the ion positions. The relationship is approximated by two conversion factors

$$\Delta T_{\text{PRF2}}^{\text{ion}} = A \times \Delta T_{\text{PRF2}}, \quad (5.4)$$

$$\Delta T_{\text{PRF3}}^{\text{ion}} = B \times \Delta T_{\text{PRF3}}, \quad (5.5)$$

$$\Delta T_{\text{ion}} = \frac{\Delta T_{\text{PRF2}}^{\text{ion}} + \Delta T_{\text{PRF3}}^{\text{ion}}}{2}. \quad (5.6)$$

The factors are independent of the used rf voltage amplitude, but may change for different rf drive frequencies. The conversion factors have been determined for trap II and trap IV and are listed in Tab. 5.4. The uncertainties of the Pt100 temperatures contain the estimated uncertainty of the sensor calibration and the maximum observed local deviation of the temperature rise between the IR image and the simulation result. The latter is an upper boundary for the mismatch between the observed and the simulated temperature rise of the trap. For trap IV the IR measurement of trap III has been used to determine this error. To estimate the error of the conversion factor, the simulations have been repeated while the most important physical properties have been varied one by one within their respective level of uncertainty. Many of these parameters that have been listed above, will affect the measured temperature and their influence on the conversion factors A and B is small. They do not significantly change the ration between trap temperature and the temperature at the ion position. For the emissivity of the gold coating, this is not case as this value only has little contribution to the trap temperature but has significant influence on the temperature seen by the ions. So the main contribution of the estimated uncertainty of the conversion factors

is originating from the gold emissivity $\varepsilon_{\text{Au}} = 0.05_{-0.03}^{+0.10}$. Finally, for the uncertainty of the ion temperature, the Gaussian error propagation is used.

With the values from Tab. 5.4 the contribution of the trap temperature rise to the black-body radiation shift of $^{115}\text{In}^+$ ions can be derived using Eq. 2.62. If the uncertainty of the scalar polarizability $\Delta\alpha_s$ is neglected (see Sec. 2.5.2), the resulting shifts and its uncertainties are

$$\text{for trap II: } \frac{\Delta\nu_{\text{BBR}}}{\nu_0} = (-1.84 \pm 0.40) \times 10^{-19}, \quad (5.7)$$

$$\text{for trap IV: } \frac{\Delta\nu_{\text{BBR}}}{\nu_0} = (-0.66 \pm 0.24) \times 10^{-19}. \quad (5.8)$$

For the calculation of these numbers an rf voltage amplitude of $U_{\text{rf}} = 1 \text{ kV}$ has been assumed. The given frequency shift only accounts for the trap related temperature increase as seen by the ion over the temperature of the vacuum chamber. The vacuum chamber temperature is assumed to be $T_{\text{vac}} = 293.15 \text{ K} = 20^\circ\text{C}$. In order to avoid an increased BBR shift uncertainty, the temperature of the vacuum chamber needs to be measured and controlled with the same level of accuracy as the trap temperature. The total BBR shift at the assumed temperature T_{vac} is $\frac{\Delta\nu_{\text{BBR}}}{\nu_0} = -1.25 \times 10^{-17}$.

Summarizing the results of the trap temperature measurements it could be shown that for both traps the contribution of the trap temperature to the frequency uncertainty is well below 1×10^{-19} . The improvements that were introduced in the manufacturing of trap IV helped to reduce the induced frequency shift by almost a factor 3 and the uncertainty contribution is reduced by 40%. The remaining challenge for the determination of the total BBR shift is the precise determination of the polarizability $\Delta\alpha_s$. As discussed in Sec. 2.5.2 the current uncertainty of the simulated polarizability $\Delta\alpha_s$ contributes to a BBR shift uncertainty of $\Delta\nu_{\text{BBR}}/\nu_0 = 1.1 \times 10^{-18}$, which is more than an order of magnitude higher than the contribution of the temperature uncertainty.

5.2. Secular Frequencies

In this section measurements of the secular frequencies of a single $^{172}\text{Yb}^+$ ion are compared to results of the trap potential calculator (see Sec. 3.3 and the Appendix A.4). Through the comparison the reliability and accuracy of the calculated potentials is tested. Because the trap potentials are sensitive to changes of the trap geometry, the comparison can also serve as another cross check of the trap electrode distances.

The trap frequencies were measured by modulating the light intensity of the H2 cooling laser beam with an AOM with a modulation depth of close to 100%. The modulated light intensity modulates the cooling and heating rate. If the modulation frequency matches to the secular frequency, the ion heats up, which can either be observed as a blurring of the image on the EMCCD or by a drop of the fluorescence intensity. In

contrast to the parametric heating method, where the rf voltage is amplitude modulated, this method can heat up the ion only at the position of the laser beam. Thus it is very unlikely to heat the ion completely out of the trap. Also the other two cooling laser beams can be used to damp the motion and the heating of the ion. This allows to tune the sensitivity of this measurement method.

Using the a -parameters $a_z(U_{\text{ax}}, U_t, U_e)$ and $a_{\text{rad},i}(U_{\text{ax}}, U_t, U_e)$ and the q -parameter $q(U_{\text{rf}})$ the trap frequencies can be calculated with

$$\omega_{\text{ax}} = \frac{\Omega_{\text{rf}}}{2} \sqrt{a_z(U_{\text{ax}}, U_t, U_e)}, \quad (5.9)$$

$$\omega_{\text{rad},i} = \frac{\Omega_{\text{rf}}}{2} \sqrt{a_{\text{rad},i}(U_{\text{ax}}, U_t, U_e) + 0.5 q^2(U_{\text{rf}})}. \quad (5.10)$$

Where the index $i \in \{1, 2\}$ represents the two orthogonal principal axes and U_{ax} are the symmetrically applied U_t voltages of the two neighbouring trap segments, which provide the axial confinement. E.g. for trap segment 7 the voltage $U_{\text{ax}} = 1 \text{ V}$ corresponds to $U_{\text{t,seg6}} = U_{\text{t,seg8}} = 1 \text{ V}$.

Because of Eq. 2.11 the q -parameter scales linear with U_{rf} . The pure ponderomotive potential is radially symmetric and does not have a preferred direction. A radial asymmetry is introduced by the application of the dc voltages U_{ax} , U_t and U_e . The resulting radial potential of each of these voltages is close to the trap center well approximated by a saddle potential, which can be described in polar coordinates with

$$V(r, \varphi) = \frac{1}{2} m \omega_{\text{rad}}^2(\varphi) r^2 = \frac{1}{2} m (u_0 + u_1 \sin(2\varphi - \theta)) r^2. \quad (5.11)$$

The angle θ defines the orientation of the strong and weak trap axis with respect to the x -axis. The strong axis is defined by the angle $\theta + \frac{\pi}{4}$ and the weak axis by $\theta - \frac{\pi}{4}$. The sum of the three different saddle potentials associated to the three dc voltages is again a saddle potential and can also be described by Eq. 5.11. The relations of the parameters u_0 and u_1 to the a - and q -parameters are given by

$$u_0 = \frac{\Omega_{\text{rf}}^2}{4} \left(q^2 + \frac{a_{\text{rad},1} + a_{\text{rad},2}}{2} \right), \quad (5.12)$$

$$u_1 = \frac{\Omega_{\text{rf}}^2}{8} |a_{\text{rad},1} - a_{\text{rad},2}|. \quad (5.13)$$

Tab. 5.5 lists the calculated radial a -parameters and the orientation for the individual dc potentials. It shows that the influence of U_t on the radial potential is a factor of 2–10 stronger than the influence of the other two voltages. From the table it is seen that all three dc potentials have a different orientation. Because of this, the trap axes can be rotated by adjusting the ratio U_e/U_t . If the dominating contribution to the a -parameters originates from U_e the principal axis is only tilted by approximately 4° with respect to the x -axis. If U_t is dominating, the radial trap axis has an angle of 48°

Voltage	Segment length	Orientation of $\tilde{a}_{\text{rad},1}$ to x-axis	$\tilde{a}_{\text{rad},1}$ (V^{-1})	$\tilde{a}_{\text{rad},2}$ (V^{-1})
U_{ax}	1 mm	-32.9°	-4.38×10^{-5}	-1.16×10^{-5}
U_{t}	1 mm	48.1°	1.60×10^{-4}	-9.73×10^{-5}
U_{e}	1 mm	4.7°	1.77×10^{-5}	-1.31×10^{-5}
U_{ax}	2 mm	-15.1°	-1.47×10^{-5}	-1.11×10^{-5}
U_{t}	2 mm	48.9°	1.57×10^{-4}	-1.30×10^{-4}
U_{e}	2 mm	4.0°	2.30×10^{-5}	-1.96×10^{-5}

Table 5.5.: Calculated radial a -parameters and their orientation with respect to the x -axis for the individual dc potentials for 1 mm and 2 mm long trap segments at $\Omega_{\text{rf}} = 2\pi \times 24.509$ MHz. The a -parameters are derived by setting the corresponding dc voltage to 1 V and ground all other electrodes.

to the x -axis. Because of the different orientations of the trap axes the a -parameters given in the table cannot simply be summed up to calculate the overall a -parameters $a_{\text{rad},i}(U_{\text{ax}}, U_{\text{t}}, U_{\text{e}})$. Instead for each dc voltage the resulting potential given by Eq. 5.10 has to be derived and added up to receive the total potential. As this approach is rather complicated in practice it is more convenient to use the Matlab trap potential calculator to predict the secular frequencies and the orientation of the trap axes.

The trap frequencies have been measured in the 2 mm wide trap segment 1 and in the 1 mm wide segment 7. The measurement results are shown and compared to the calculated values in Figs. 5.3 and 5.4. Each of the trap voltages U_{rf} , U_{ax} , U_{t} and U_{e} have been varied separately to show that the calculated potential predicts the influence of every voltage correctly. The rf voltage has been calculated by multiplying the voltage amplitudes measured at the pick up pin of the helical resonator (see Fig. 4.2) with a calibration factor $k = 5830$. The calibration factor was determined such that the experimentally measured secular frequencies match the calculation results. The factor was observed to be constant over the course of several months. For all measurements it was observed that the frequency splitting between the two radial frequencies does not fully match to the values expected from the calculation. It was found that the calculation results only fit to the observed secular frequencies if an offset voltage is added to U_{e} . This offset voltage was found to be $U_{\text{e,off,seg1}} = 2.4$ V in trap segment 1 and $U_{\text{e,off,seg7}} = 3.0$ V in trap segment 7. These voltages were added in the calculations to all trap segments in order to not influence the axial potential. Conversely, this means that there is a stray quadrupole field with an orientation identical to the field produced by U_{e} . A possible explanation for this could be static charges on insulators that are close to the ions. These charges could be produced by the incident UV light and the resulting photoelectric effect. In fact, it was observed, that a misaligned cooling laser beam hitting the trap electrodes affects the measured secular frequencies. Over the course of a few weeks the offset voltage that is needed to match the calculation results to the experimental measurements changed slowly. All calculation results shown in this section use the above mentioned offset voltages. The secular frequency measurements

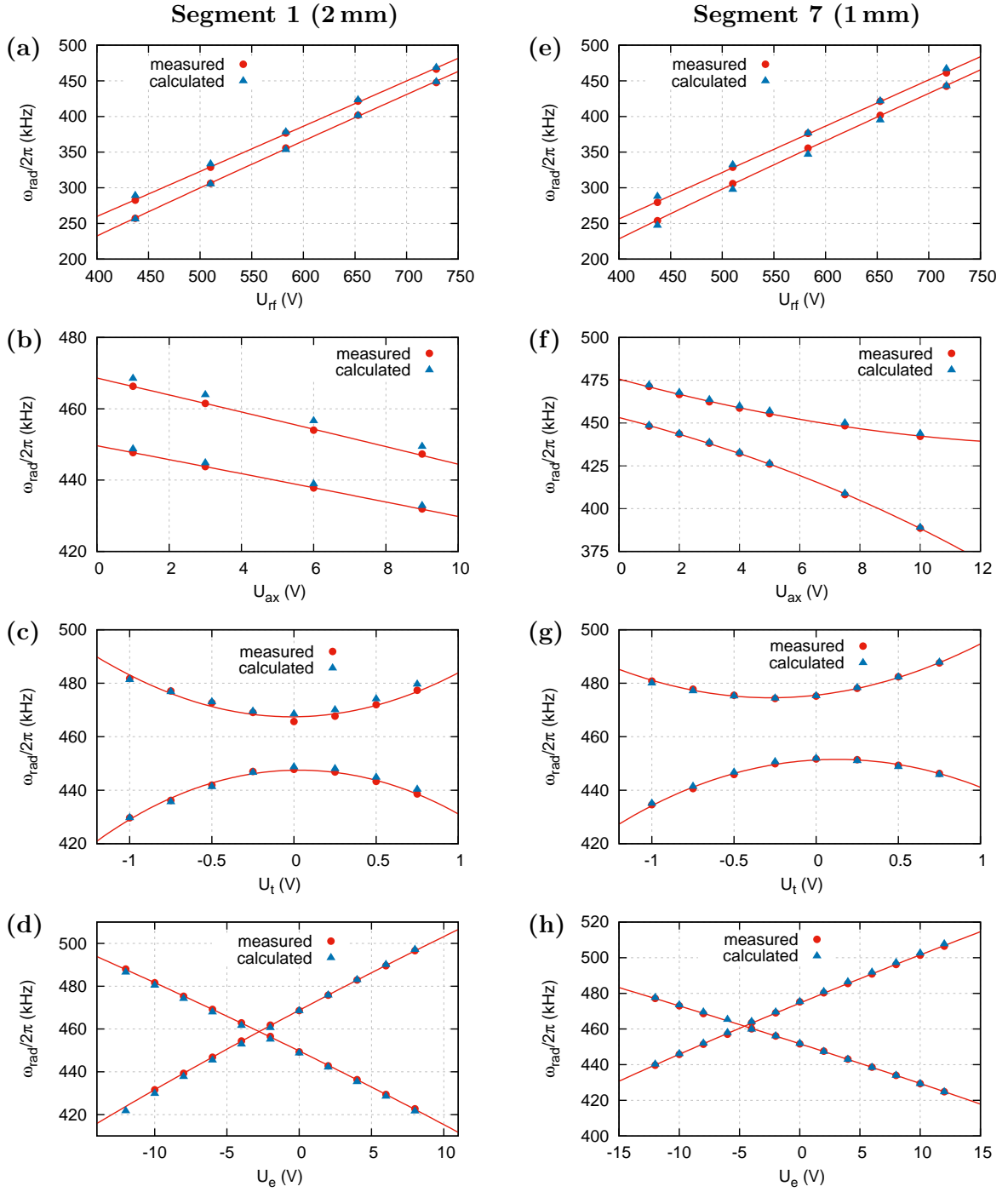


Figure 5.3.: Measured and calculated radial secular frequencies for a single $^{172}\text{Yb}^+$ ion at a trap drive frequency of $\Omega_{rf}=24.509$ MHz. (a)-(d) Trap frequencies in the 2 mm long segment 1. (e)-(h) Trap frequencies in the 1 mm long segment 7. Except for the voltage that is changed the trap voltage configuration for all measurements was $U_{ax} = 1$ V, $U_t = U_e = 0$ V and $U_{rf} = 729$ V. In order to match the calculations to the data it was necessary to adjust the calculations with a constant offset voltage $U_{e, \text{stray}}$, which was added in the calculations for all trap segments. The uncertainty of the trap frequency measurements is $\sigma_\omega = 0.2$ kHz.

shown in this work have been measured within a duration of less than a week and because of the short time period an adaption of the values was not necessary.

The measured and calculated radial trap frequencies are shown in Fig. 5.3. It is shown that for the chosen calculation parameters all calculated trap frequencies are close to the measured frequencies. The maximum deviations of 6–8 kHz are observed for the lowest rf voltages. Varying only the dc voltages, the differences between measured and calculated trap frequency is only 2–3 kHz. To obtain experimental values for the q -parameter the function

$$\omega_{\text{rad}}(U_{\text{rf}}) = \frac{\Omega_{\text{rf}}}{2} \sqrt{0.5 \tilde{q}^2 U_{\text{rf}}^2 + a}, \quad (5.14)$$

with fit parameters \tilde{q} and a has been fitted to the measured data of Fig. 5.3 (a) and (e). \tilde{q} is the q -parameter normalized to $U_{\text{rf}} = 1$ V and a is a constant that includes the contribution of the dc potential. The average and standard deviation of the resulting fit values is $\tilde{q} = (7.39 \pm 0.07) \times 10^{-5} \text{ V}^{-1}$. A comparison to the calculated values is not meaningful, because these have been used to define the calibration factor k . The dependency of the radial frequencies on the dc voltages U_{ax} , U_{t} and U_{e} is described by

$$\omega_{\text{rad}}(U_{\text{ax}}) = \frac{\Omega_{\text{rf}}}{2} \sqrt{\tilde{a}_{\text{ax},1} U_{\text{ax}}^2 + \tilde{a}_{\text{ax},2} U_{\text{ax}} + c_{\text{ax}}}, \quad (5.15)$$

$$\omega_{\text{rad}}(U_{\text{t}}) = \frac{\Omega_{\text{rf}}}{2} \sqrt{\tilde{a}_{\text{t},1} U_{\text{t}}^2 + \tilde{a}_{\text{t},2} U_{\text{t}} + c_{\text{t}}}, \quad (5.16)$$

$$\omega_{\text{rad}}(U_{\text{e}}) = \frac{\Omega_{\text{rf}}}{2} \sqrt{\tilde{a}_{\text{e}} U_{\text{e}} + c_{\text{e}}}. \quad (5.17)$$

These functions have been fitted to the measured trap frequencies shown in Fig. 5.3 (b)-(e) and (f)-(h). The quadratic term that is needed to describe the U_{ax} and U_{t} dependency is resulting from the different orientation of these potentials compared to the observed stray field potential that is aligned with the U_{e} potential. It is resulting from the sum of two potentials described by Eq. 5.10 with different angles θ . Because of the different angles the U_{ax} and U_{t} potential cannot completely counteract the stray field potential. In Fig. 5.3 (b) the curvature introduced by the quadratic term is not visible, because the angle between the two potentials is smaller and also the influence of U_{ax} on the radial trap frequency is small. For the description of the U_{e} dependency, the quadratic term is not needed because the resulting potential is aligned with the observed stray potential. This can also be seen by the fact that a crossing of the trap frequencies is observed. At this point the U_{e} potential cancels the stray field potential.

Fig. 5.4 shows the measured and calculated dependencies of the axial trap frequency on the trap voltages. Overall it is seen that the calculated and measured trap frequencies are in good agreement. The largest deviation between the measured and calculated frequency is about 6 kHz and it is observed for high values of U_{e} and correspondingly

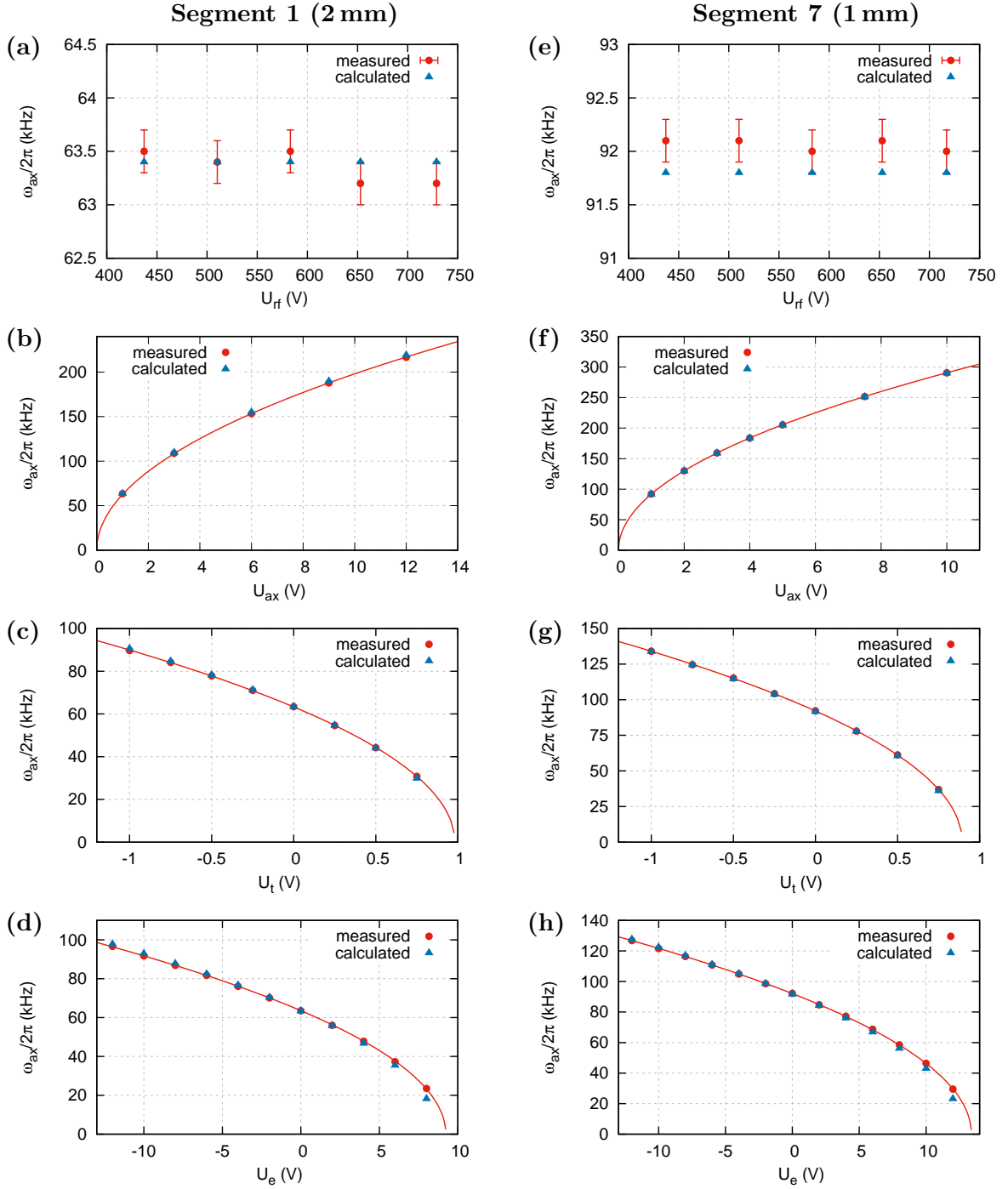


Figure 5.4.: Measured and calculated axial secular frequencies for a single $^{172}\text{Yb}^+$ ion. (a)-(d) Trap frequencies in the 2 mm long segment 1. (e)-(h) Trap frequencies in the 1 mm long segment 7. Except for the voltage that is changed the trap voltage configuration for all measurements was $U_{\text{ax}} = 1$ V, $U_{\text{t}} = U_{\text{e}} = 0$ V and $U_{\text{rf}} = 729$ V. The uncertainty of the measurement was estimated to be $\sigma_{\omega}/2\pi = 0.2$ kHz.

Voltage	Segment length	Measured \tilde{a}_{ax} (V^{-1})	Calculated \tilde{a}_{ax} (V^{-1})
U_{ax}	1 mm	$5.622(3) \times 10^{-5}$	5.59×10^{-5}
U_{t}	1 mm	$-6.312(11) \times 10^{-5}$	-6.30×10^{-5}
U_{e}	1 mm	$-4.216(6) \times 10^{-6}$	-4.36×10^{-6}
U_{ax}	2 mm	$2.612(8) \times 10^{-5}$	2.68×10^{-5}
U_{t}	2 mm	$-2.715(6) \times 10^{-5}$	-2.78×10^{-5}
U_{e}	2 mm	$-2.915(7) \times 10^{-6}$	-3.07×10^{-6}

Table 5.6.: Comparison of calculated and measured axial a -parameters for 1 mm and 2 mm long trap segments at $\Omega_{\text{rf}} = 24.509$ MHz. The a -parameters are derived by setting the corresponding dc voltage to 1 V and ground all other electrodes.

low axial frequencies of < 20 kHz. Figs. 5.4 (a) and (e) show that the rf voltage does not have a contribution on the axial trap frequency. The fluctuations of the measured values do reflect only the measurement uncertainty of $\sigma_{\omega}/2\pi = 0.2$ kHz. Thus the axial trap potential depends only on three dc voltages U_{ax} , U_{t} and U_{e} . The relation between ω_{ax} and the dc voltages is given by

$$\omega_{\text{ax}}(U_{\text{ax}}, U_{\text{t}}, U_{\text{e}}) = \frac{\Omega_{\text{rf}}}{2} \sqrt{\tilde{a}_{z,\text{ax}} U_{\text{ax}} + \tilde{a}_{z,\text{t}} U_{\text{t}} + \tilde{a}_{z,\text{e}} U_{\text{e}}}. \quad (5.18)$$

The parameters $\tilde{a}_{z,i}$ only depend on the electrode geometry and therefore a comparison between measured and calculated values can serve as a test of the trap electrode geometry. To derive the experimental a -parameters the functions

$$\omega_{\text{ax}}(U_{\text{ax}}) = \frac{\Omega_{\text{rf}}}{2} \sqrt{\tilde{a}_{z,\text{ax}} U_{\text{ax}}} \quad (5.19)$$

$$\omega_{\text{ax}}(U_{\text{t}}) = \frac{\Omega_{\text{rf}}}{2} \sqrt{\tilde{a}_{z,\text{t}} U_{\text{t}} + \tilde{c}_{\text{t}}} \quad (5.20)$$

$$\omega_{\text{ax}}(U_{\text{e}}) = \frac{\Omega_{\text{rf}}}{2} \sqrt{\tilde{a}_{z,\text{e}} U_{\text{e}} + \tilde{c}_{\text{e}}} \quad (5.21)$$

have been fitted to the measured trap frequencies. The resulting normalized a -parameters are compared to the calculated values in Tab. 5.6. The listed errors are the resulting fit errors. The table shows a good agreement between the measured and calculated axial a -parameters. The maximum relative deviation between calculation and measurement is approximately 5% for the axial U_{e} potential. In terms of the trap frequency this corresponds to the differences as shown in the plots.

In summary, it is found that the trap potential calculator is a useful tool that can predict the trap frequencies with an uncertainty of only a few kHz. To achieve this level of uncertainty, the rf calibration factor k as well as stray field potentials need to be known. Changes in these two parameters will lead to larger deviations. The calculator is also useful to estimate the orientation of the two radial trap axes. However the accuracy of this estimation has not been tested.

5.3. Excess Micromotion Measurements

As discussed in Sec. 3.1 the minimization of excess micromotion (EMM) along the axial trap axis has been one of the main targets of the trap development process. It is essential for the realization of a multi-ion clock. Otherwise, the related second-order Doppler shift and Stark shift will lead to an unacceptable large frequency shift and uncertainty.

5.3.1. Photon-Correlation Spectroscopy

The micromotion amplitudes have been measured using the photon-correlation spectroscopy technique. Due to the first-order Doppler shift, the ion fluorescence resulting from the Doppler cooling light shows a modulation at the trap drive frequency Ω_{rf} . The modulation amplitude is correlated to the micromotion amplitude. In the limit $\Omega_{\text{rf}} \ll \Gamma$, the method has been described in detail in [65]. Within this limit, the time between photon absorption and spontaneous emission is small compared to the rf cycle time and the fluorescence signal will always follow the modulated absorption rate without any delay.

This approximation is not valid for this experiment, where $\Omega_{\text{rf}} = 2\pi \times 24.38$ MHz and $\Gamma = 2\pi \times 19.6$ MHz. Therefore, a more general theoretical description is needed to correctly calculate the relation between the observed modulation of the fluorescence and the micromotion amplitude. Such a model has been presented and verified in [58, 87] and in the following the main results of those publications are summarized.

In the reference frame of the ion, the effect of the first-order Doppler shift due to micromotion can be described as a laser phase modulation at Ω_{rf}

$$E(\omega) = E_0 \cos(\omega t + \beta \cos \Omega_{\text{rf}} t). \quad (5.22)$$

The phase modulation amplitude $\beta = |\vec{k}\vec{x}_0| = \frac{|k\vec{v}_0|}{\Omega_{\text{rf}}}$, where \vec{x}_0 and \vec{v}_0 are the micromotion position and velocity amplitude. Within this work the rf field amplitude — \vec{E}_{rf} is used to quantify the micromotion. The relation to \vec{x}_0 , \vec{v}_0 and β is given by

$$|\vec{E}_{\text{rf}}| = \frac{m\Omega_{\text{rf}}^2}{e} |\vec{x}_0| = \frac{m\Omega_{\text{rf}}}{e} |\vec{v}_0| = \frac{m\Omega_{\text{rf}}^2}{ke} \beta. \quad (5.23)$$

For low micromotion amplitudes with $\beta \ll 1$ (e.g. $\beta = 0.1$ corresponds to $|\vec{E}_{\text{rf}}| = 246$ V/m), the laser frequency spectrum in the ion reference frame can be approximated by

$$E(\omega) \propto J_0(\beta)\delta(\omega - \omega_L) + J_1(\beta)(\delta(\omega - \omega_L - \Omega_{\text{rf}}) - \delta(\omega - \omega_L + \Omega_{\text{rf}})), \quad (5.24)$$

where J_n are the Bessel functions of the first kind. This spectrum is interacting with the ion resonance, which in a classical description can be described by a damped harmonic oscillator with the frequency response described by [31]

$$A(\omega - \omega_0) = \frac{1}{2} \frac{\frac{\Gamma}{2} - i(\omega - \omega_0)}{(\omega - \omega_0)^2 + (\frac{\Gamma}{2})^2}. \quad (5.25)$$

Both spectra are shown in Fig. 5.5 (a), which also illustrates the detuning Δ , the rf frequency Ω_{rf} and the decay rate Γ . The resulting excitation is proportional to the observed fluorescence signal which is given in the time domain by

$$\begin{aligned} S(\Delta, t) &= \left| \int_{-\infty}^{\infty} A(\omega - \omega_0) E(\omega) e^{i\omega t} d\omega \right| \\ &\propto \underbrace{J_0^2(\beta) |A(\Delta)|^2 + J_1^2(\beta) (|A(\Delta + \Omega_{\text{rf}})|^2 + |A(\Delta - \Omega_{\text{rf}})|^2)}_{S_0} \\ &\quad + 2 \underbrace{J_0(\beta) J_1(\beta) |A^*(\Delta) A(\Delta + \Omega_{\text{rf}}) - A(\Delta) A^*(\Delta - \Omega_{\text{rf}})|}_{\Delta S} \cos(\Omega_{\text{rf}} t + \varphi) \\ &\quad + \mathcal{O}(J_1^2(\beta)) \\ &\propto S_0 + \Delta S \cos(\Omega_{\text{rf}} t + \varphi). \end{aligned} \quad (5.26)$$

The equation shows that the fluorescence consists of a static component labelled S_0 and a component ΔS that is oscillating at Ω_{rf} . The oscillating part results from the beat of the excitation on the micromotion sidebands with the carrier excitation. Fig. 5.5 (b) shows the measured $^{172}\text{Yb}^+$ ion fluorescence and its oscillation at Ω_{rf} . For $\beta \ll 1$ the constant term with the factor $J_1^2(\beta)$ can be neglected and the quantity $\Delta S/S_0 \propto J_1(\beta)/J_0(\beta)$ can be used to determine β or E_{rf} . For higher micromotion amplitudes, where the limitation $\beta \ll 1$ does not hold anymore, also higher order micromotion sidebands have to be considered. This will lead to additional frequency components in the fluorescence signal.

In order to maximize the sensitivity of the measurement, the detuning has been optimized to achieve a maximum signal $\Delta S/S_0$. This measurement is shown in Fig. 5.5 (c) and it is compared to the theoretical expectation resulting from Eq. 5.26. The graph shows that the theoretical description correctly describes the observed dependency. The signal is maximized at a detuning $\Delta \approx \Omega_{\text{rf}}$. At this detuning the red micromotion sideband is close to the atomic resonance and this maximizes its contribution to ΔS . In [58, 87] it is shown that the detuning dependency of the phase $\varphi(\Delta)$ in Eq. 5.26 is also described correctly by this model.

Although the classical approach is describing the observed dependencies correctly, it does not allow to take saturation effects into account. To decrease errors in the data evaluation, numerical simulations of the quantum mechanical master equation have

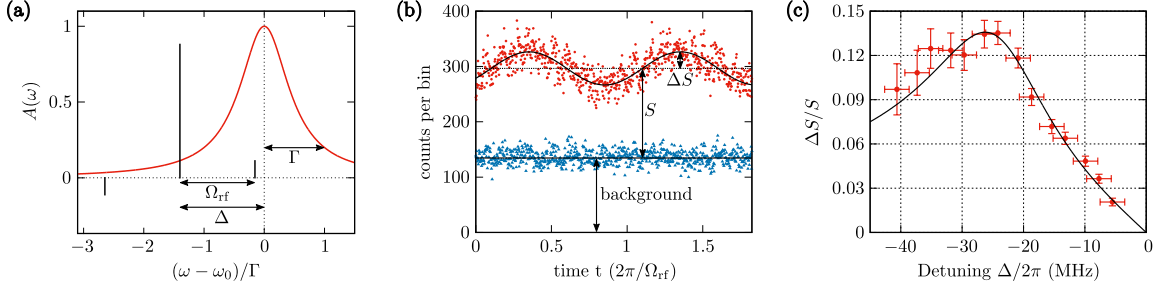


Figure 5.5.: Graphs illustrating the principles of the photon-correlation spectroscopy. (a) Spectrum $E(\omega)$ of the laser as seen by the ion and the classical frequency response of the ion $A(\omega)$. (b) The amplitude of the fluorescence is oscillating at Ω_{rf} . Background counts resulting from stray light have to be subtracted to determine the signal $\Delta S/S_0$. (c) Dependence of the measured signal $\Delta S/S_0$ on the detuning Δ . The solid line is showing the theoretical expectation that has been adjusted only by a frequency offset and by scaling of the amplitude to match the experimentally measured data.

been used to find the relation $E_{\text{rf}}(\Delta S/S_0)$. The Hamiltonian describing the system in the interaction picture is given by

$$H(t) = \hbar \begin{pmatrix} 0 & \frac{\Omega}{2} \\ \frac{\Omega}{2} & \Delta \end{pmatrix} + \hbar \begin{pmatrix} 0 & 0 \\ 0 & \vec{k}\vec{v}_0 \end{pmatrix} \cos(\Omega_{\text{rf}}t), \quad (5.27)$$

where $\Omega = \Gamma\sqrt{I/2I_{\text{sat}}}$ is the Rabi frequency (I_{sat} is the saturation intensity) and $\vec{k}\vec{v}_0$ is the first order Doppler shift resulting from micromotion. A numerical calculation [88] of the excited state population is used to determine the dependence of $\Delta S/S_0$ on the micromotion amplitude. To find an appropriate expression for $E_{\text{rf}}(\Delta S/S_0)$, a third-order polynomial is fitted to the simulation results. The relative error introduced by this approximation is less than 1% of the observed micromotion in the range of $E_{\text{rf}} < 765 \text{ V/m}$. By using different values for the light intensity, the influence of the saturation on $\Delta S/S_0$ has been studied. This shows that an increased intensity is leading to a reduction of $\Delta S/S_0$ (see also Ref. [58]). However, for the experimentally available laser power, corresponding to $I \approx I_{\text{sat}}$ for all three Doppler cooling beams, the increase of the ion fluorescence count rate overcompensates this contrast reduction.

5.3.2. Experimental Implementation

For the 3-dimensional determination of the micromotion amplitude all three cooling laser beams (labelled H1, H2 and V as introduced in Fig. 4.7) have been used successively. Since the V beam has no projection on the axial trap axis, a strongly attenuated H1 beam has been added during the V measurement to provide cooling in axial direction. The ion fluorescence is imaged on a photomultiplier tube (PMT). Each photon count is used as a start trigger for a time-to-amplitude converter (TAC) and the stop trigger is generated by the next zero crossing of the trap drive voltage U_{rf} . A histogram of the resulting amplitudes is generated by feeding the output of the TAC to a

multi-channel analyser. Typical measurement times that have been used are between 45–90 s for each one of the three beams. The resulting signal is shown in Fig. 5.5 (b) and shows the oscillation of the fluorescence at the drive frequency Ω_{rf} . The signal is corrected for parasitic crosstalk of the rf field on the PMT signal [58, 87] and a previously measured background level is subtracted. A sinusoidal is then fitted to the resulting data and the value $\Delta S/S_0$ is determined by the offset and amplitude of the fit function as shown in Fig. 5.5 (b). Using the third order polynomial resulting from the numerical calculations of the system, the three rf amplitudes $E_{\text{rf,H1}}$, $E_{\text{rf,H2}}$ and $E_{\text{rf,V}}$ are found. These are the projections of the rf field \vec{E}_{rf} onto the three laser axis. From these values the values of the rf field along the coordinate axes as defined in Fig. 4.7 are derived by

$$E_{\text{rf,x}} = \frac{1}{2 \cos(\theta_x)} \sqrt{E_{\text{rf,H1}}^2 + E_{\text{rf,H2}}^2 + 2E_{\text{rf,H1}}E_{\text{rf,H2}} \cos(\varphi_{\text{H1}} - \varphi_{\text{H2}})} \quad (5.28)$$

$$E_{\text{rf,y}} = E_{\text{rf,V}} \quad (5.29)$$

$$E_{\text{rf,z}} = \frac{1}{2 \cos(\theta_z)} \sqrt{E_{\text{rf,H1}}^2 + E_{\text{rf,H2}}^2 - 2E_{\text{rf,H1}}E_{\text{rf,H2}} \cos(\varphi_{\text{H1}} - \varphi_{\text{H2}})}. \quad (5.30)$$

The equations are resulting solely from geometrical considerations. In the equations $\theta_x = 65^\circ$ is the angle between the laser beams H1 and H2 and the x-axis. Respectively $\theta_z = 25^\circ$ is the angle of H1 and H2 to the z-axis. φ_{H1} and φ_{H2} are the phases of rf voltage to the micromotion measured by H1 and H2. For a fixed detuning and without micromotion caused by rf voltage phase shifts (see Sec. 2.2.1), the phase difference $\varphi_{\text{H1}} - \varphi_{\text{H2}}$ will be either 0 or $\pm\pi$. Since it frequency fluctuations and rf voltage phase shifts cannot be excluded, the fitted phases of the photon-correlation signals have been used for the calculations of the rf fields.

Uncertainties that have been included in the error budget are the fit error of $\Delta S/S_0$ and of the phases φ_{H1} and φ_{H2} , the error of determining the background, the intensity uncertainty, the detuning uncertainty and the uncertainty of the angels θ_x and θ_z . The size and determination of the main uncertainties have been studied in [58, 87]. The dominating error source is the fit error of the sine amplitude ΔS . As also shown in [58], the total uncertainty is limited by shot noise and hence can be reduced by increasing the measurement time. The typical total uncertainty for the given measurement times of 45–90 s is in the rage of $\Delta_{E_{\text{rf,xyz}}} = 5 - 10 \text{ V/m}$.

For the determination of the micromotion amplitude along the trap axis, a single ion was shifted by changing the axial trap voltages. A comparison of this method with a measurement of micromotion on a complete Coulomb crystal [89] has shown that both methods provide identical results. Thus, the single ion can be used to measure the micromotion that will be seen by an ion Coulomb crystal.

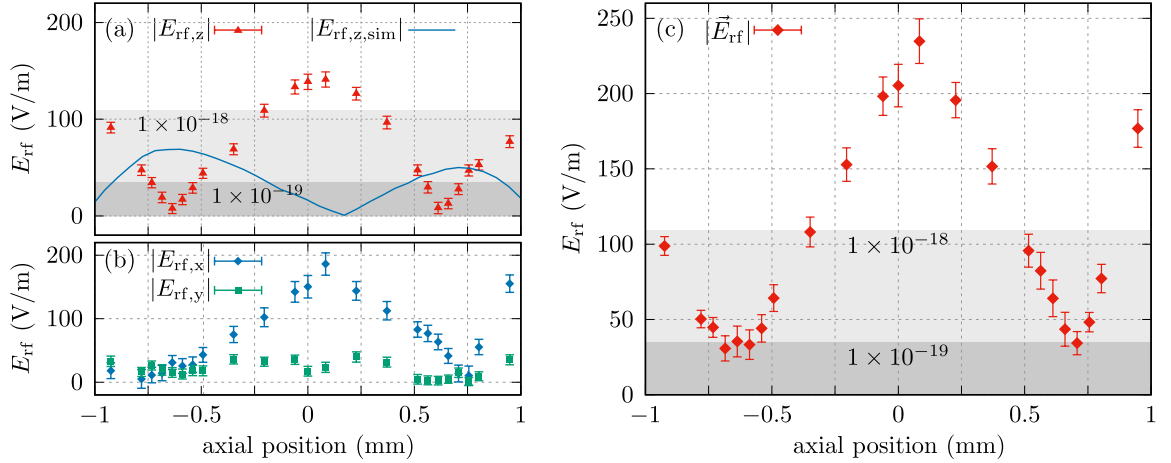


Figure 5.6.: Results of EMM measurement in segment 1 with a width 2 mm. (a) Measured axial micromotion $|E_{rf,z}|$ (red triangles) compared to the FEM calculation result of a trap with perfect geometry (blue line). (b) Measured radial micromotion $|E_{rf,x}|$ (blue diamonds) and $|E_{rf,y}|$ (green squares). (c) Resulting total micromotion amplitude $|\vec{E}_{rf}|$. The shaded areas indicate the resulting time dilation shifts for $^{115}\text{In}^+$ ions.

5.3.3. Results of Micromotion Measurements

The axial and radial micromotion have been measured in trap segment 1 with 2 mm width and in segment 7 with a width of 1 mm (segment numbering according to Fig. 3.3). The measured micromotion amplitudes are shown in the graphs of Figs. 5.6 and 5.7. In segment 1, the measured trap frequencies for the used voltage configuration have been $\omega_{ax} = 2\pi \times 211.5$ kHz, $\omega_{rad,1} = 2\pi \times 457.4$ kHz and $\omega_{rad,2} = 2\pi \times 489.3$ kHz. With these values the rf voltage amplitude has been determined with the trap potential calculator to be $U_{rf} = 778$ V. Fig. 5.6 (a) shows the comparison of the experimentally measured axial micromotion to the FEM simulation results of a trap without any geometry imperfections. Over the length of the whole trap segment the measured axial micromotion is $|E_{rf,z}| < 145$ V/m, which is only about a factor of two higher than the maximum value obtained in the simulation. In contrast to the simulation result, the maximum axial micromotion is observed close to the centre of the trap segment. Two minima are observed which are both approximately ± 0.625 mm away from the trap center. At the left side at -0.625 mm there is a region of approx. $100 \mu\text{m}$ length with a fractional frequency shift of $^{115}\text{In}^+$ at the level of 1×10^{-19} .

In order to find possible explanations for the axially shifted micromotion minima, various simulations have been performed. The simulations showed that all symmetric deviations (deviations that are of equal size for all rf or dc electrodes) cannot be the reason for the shifted zero crossing of the axial micromotion. A tilt angle α , as illustrated in Fig. 3.6, would cause a constant offset of the axial rf field and therefore shifts the zero point. Another possible explanation for a shifted zero point is an asymmetry in the position or shape of the notches at the end of the trap segment

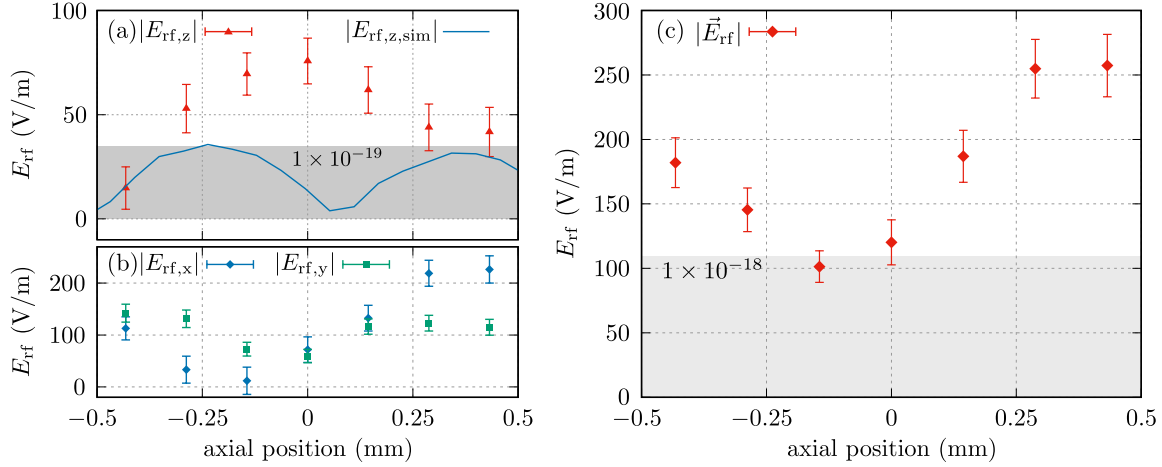


Figure 5.7.: Results of EMM measurement in segment 7 with a width 1 mm. (a) Measured axial micromotion $|E_{rf,z}|$ (red triangles) compared to the FEM calculation result of a trap with perfect geometry (blue line). (b) Measured radial micromotion $|E_{rf,x}|$ (blue diamonds) and $|E_{rf,y}|$ (green squares). (c) Resulting total micromotion amplitude $|\vec{E}_{rf}|$. The shaded area indicates the resulting time dilation shift for $^{115}\text{In}^+$ ions.

electrodes. Such an asymmetry is introduced by the broken off corners on the backside of the PRF wafers or by the waviness of the backside edges as shown in Fig. 3.10.

Compared to the previously used prototype trap [30, 58], the axial micromotion amplitude could be reduced substantially. The prototype showed only a region of $40 \mu\text{m}$ with $|E_{rf,z}| < 145 \text{ V/m}$. This could now be extended to the whole trap segment. Also for the prototype traps, a displacement of the axial micromotion minimum away from the trap segment centre has been observed [30], although the displacement was smaller than the value observed in the AlN trap. It is assumed that because of the lower axial rf field the AlN trap is more sensitive to asymmetries in the trap geometry.

Fig. 5.6 (b) shows the radial micromotion components that have been measured together with the axial micromotion. Radial micromotion has been minimized with the compensation voltages U_{tc} and U_{ec} at the position -0.625 mm . At other positions, the radial micromotion amplitudes can be further reduced by a better choice of compensation voltages. Fig. 5.6 (c) shows the absolute value of the micromotion vector $|\vec{E}_{rf}|$. It can be seen that this is mainly dominated by the axial micromotion amplitude. The maximum observed amplitude $|\vec{E}_{rf}| = (235 \pm 15) \text{ V/m}$ corresponds to a time dilation shift for $^{115}\text{In}^+$ of $(4.6 \pm 0.3) \times 10^{-18}$. Within a range of about $580 \mu\text{m}$, a time dilation shift due to micromotion of less than 1×10^{-18} is observed. The smallest observed 3D micromotion amplitude is $|\vec{E}_{rf}| = (8 \pm 5) \text{ V/m}$ which corresponds to a shift of only 5.3×10^{-21} .

Fig. 5.7 (a) shows the axial micromotion amplitudes measured in the 1 mm wide segment 7 and compares it to the FEM simulation results of a perfectly shaped ion trap. Compared to the measurement in segment 1, the measurement time for each point has

been reduced from 90 s to 45 s. This also explains the larger uncertainties of this measurement. The rf voltage was kept at $U_{\text{rf}} = 778 \text{ V}$ and the measured trap frequencies have been $\omega_{\text{ax}} = 2\pi \times 319.2 \text{ kHz}$, $\omega_{\text{rad},1} = 2\pi \times 404.3 \text{ kHz}$ and $\omega_{\text{rad},2} = 2\pi \times 471.6 \text{ kHz}$. Again, the measured micromotion amplitudes are about a factor of two larger than expected from simulations. The maximum observed axial micromotion amplitude of $E_{\text{rf},z} = (76 \pm 11) \text{ V/m}$ is observed at the segment centre. This corresponds to a time dilation shift for $^{115}\text{In}^+$ of $(4.8 \pm 1.4) \times 10^{-19}$. The smallest axial micromotion $E_{\text{rf},z} = (15 \pm 10) \text{ V/m}$ is observed close to the edge of the segment. The possible explanations for the unexpected large displacement of the axial micromotion minimum are identical to those discussed above for segment 1.

The measured radial components and the total 3D micromotion amplitudes are shown in Fig.5.7 (b) and (c). They show that the radial micromotion amplitudes have not been very well compensated during the measurement. Because of this, the radial components are also dominating the 3D micromotion amplitudes which are observed to be in the range of 100–260 V/m. Still, at maximum micromotion amplitude the second-order Doppler shift is only $(5.5 \pm 1.0) \times 10^{-18}$. At the minimum 3D micromotion amplitude the shift reduces to $(8.5 \pm 2.0) \times 10^{-19}$. It is expected that by a more careful compensation of radial micromotion this shift can be reduced to lower values.

In total, it can be concluded that regardless of the ion position along the trap axis the fractional frequency shift uncertainty due to micromotion of an $^{115}\text{In}^+$ ion is $\leq 1 \times 10^{-18}$. When the ions are shifted to the appropriate position it seems to be feasible to reduce the uncertainty to below 1×10^{-19} . Also, the results prove that the FEM results can predict the level of micromotion with an acceptable accuracy. Only through the simulation results it has been possible to optimize the trap design for lowest micromotion amplitudes.

5.4. Heating Rate Measurement

For precision spectroscopy ion temperatures in the range of 1 mK or below are desirable and the temperature needs to be measured and kept stable, because it causes a second-order Doppler shift (see Eq. 2.60). Additionally, during the clock spectroscopy pulse it is desirable to switch off all cooling lasers in order to minimize ac stark shifts. These conditions can only be fulfilled simultaneously if the external heating rate is sufficiently low.

The ion heating is caused by electric field noise which is exciting the secular motion of the ion. If micromotion is neglected, the relation between the heating rate \dot{n} in units of phonons/s and the spectral density of the electric field noise is given by [66]

$$\dot{n} = \frac{e^2}{4m \hbar \omega_{\text{sec}}} S_E(\omega_{\text{sec}}). \quad (5.31)$$

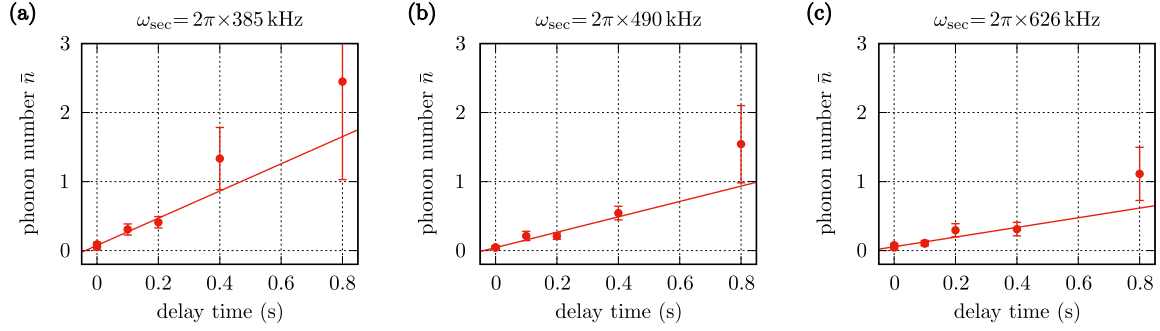


Figure 5.8.: Results of the heating rate measurements at three different trap frequencies. For higher trap frequencies, the heating rate decreases. Solid lines represent linear fits to the measured data points.

The electric field noise itself can have various sources and because of the complexity it is difficult to identify dominant noise sources. The comparison of observed heating rates at different experiments [66] reveals a spread over several order of magnitudes even when similar experimental conditions apply. The reasons for this huge spread are currently not well understood and need further investigation. Besides the complexity, some scaling effects are expected and have also been observed experimentally. Typically, the heating rate reduces for an increased secular frequency, for an increased electrode-ion distance [84, 90] and for a decreased trap temperature [90, 91].

In order to measure the ion heating rate experimentally, a single $^{172}\text{Yb}^+$ ion in the trap has first been cooled to its motional ground state as described in Sec. 4.4. After the sideband cooling pulse and before the temperature determination via sideband spectroscopy, a variable delay time was added to the experimental sequence shown in Fig. 4.12. A linear fit to the temporal evolution of the mean phonon number \bar{n} was used to obtain the heating rate $\dot{\bar{n}}$. The measured data and the linear fits are shown in Fig. 5.8. The results of all heating rate measurements are summarized in table Tab. 5.7. The calculated influence of the heating rate on a single trap axis on the second-order Doppler shift shows that the shift is well below 1×10^{-19} . Considering the optimum spectroscopy pulse length for $^{115}\text{In}^+$ ions of 365 ms in the case of Rabi

secular frequency $\omega_{\text{sec}}/2\pi$ (kHz)	heating rate $\dot{\bar{n}}$ (phonons/s)	Spectral density of electric field noise $S_E(\omega_{\text{sec}})$ ($\text{V}^2\text{m}^{-2}\text{Hz}^{-1}$)	2 nd -order Doppler shift for $^{115}\text{In}^+$ $\frac{\partial}{\partial t} \frac{\Delta\nu}{\nu_0}$ (s^{-1})
385	1.97(29)	$2.2(3) \times 10^{-14}$	$2.9(4) \times 10^{-20}$
490	1.10(15)	$1.6(2) \times 10^{-14}$	$2.1(3) \times 10^{-20}$
626	0.70(17)	$1.3(3) \times 10^{-14}$	$1.7(4) \times 10^{-20}$

Table 5.7.: Results of the heating rate measurements at three different secular frequencies ω_{sec} . The frequency shift only considers the heating in one of the three trap axes.

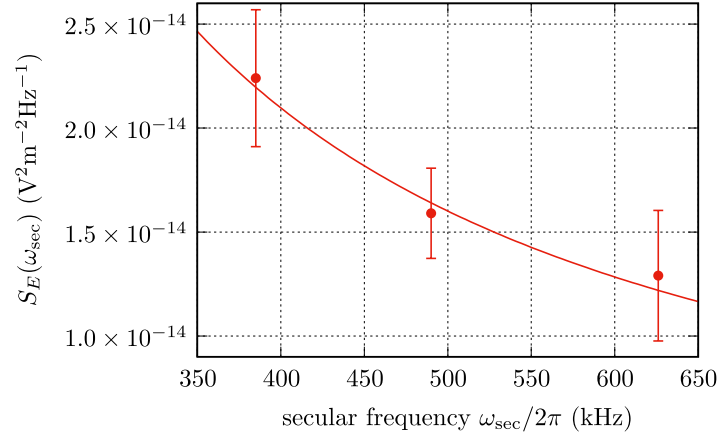


Figure 5.9.: Measured spectral density of electric field noise versus the secular frequency. The line shows the fit result discussed in the main text.

excitation and 194 ms in the case of Ramsey excitation the resulting shift will be even below 1×10^{-20} and totally negligible.

In Fig. 5.9 the resulting spectral density of the electric field noise S_E is plotted over the secular frequency ω_{sec} . The solid line shows the function $S_E(\omega_{\text{sec}}) = c \omega_{\text{sec}}^{-\alpha}$ fitted to the data points. The scaling parameter is found to be $\alpha = 1.2 \pm 0.2$, which is still in agreement with the commonly observed $1/f$ noise. For clock operation it is important to see that there is no resonance near the operating trap frequency. This allows to freely choose the secular frequency for clock operation. The measured data does not allow to clearly identify a main source for the observed heating rate. The heating rate that is contributed by the voltage noise from the dc supply and by the Johnson-Nyquist noise have been calculated in Sec. 4.2.2. For both sources the estimated contribution is negligibly small compared to the measured values. The observed heating rate is at the same level as reported on the previously used Rogers prototype trap [58]. Compared to similar sized ion traps (cf. Fig. 8 in [66]), the observed heating rate is one of the lowest that have been reported.

6. Creation and Dynamics of Topological Defects in Ion Coulomb Crystals

This chapter includes the authors manuscript that has been published in [92]¹. The author has contributed to these publications by performing experiments, experimental data evaluation, performing simulations with experimental parameters and the analysis of the simulation results. The main focus of this work was to study the influence of mass defects on the creation and stability of topological defects through numerical simulations and experiments. Furthermore, the author contributed to simulations and measurements that use external electric fields to manipulate and create kinks in a controlled manner. All experiments presented in this chapter used the prototype trap, which has been characterized in Refs. [29, 30].

¹The original publication is available at http://en.sif.it/books/series/proceedings_fermi

Creation and Dynamics of Topological Defects in Ion Coulomb Crystals

T. BURGERMEISTER and T. E. MEHLSTÄUBLER

Physikalisch-Technische Bundesanstalt, Bundesallee 100, 38116 Braunschweig, Germany

Summary. — We discuss our recent studies of topological defects (kinks) in ion Coulomb crystals. Experimentally two different types of kinks are created by non-adiabatically driving the second-order phase transition from a linear to a zigzag phase. The kink creation rates are investigated in relation to the inhomogeneous Kibble-Zurek mechanism. Stability and dynamic properties of both types of kinks are explained by the Peierls-Nabarro potentials. In addition, we report on the influence of mass defects on kinks. We show how the application of electric fields can change the influence of mass defects in a controlled way and present a first evidence for a deterministic creation and manipulation of kinks.

1. – Introduction

Since the first observation of topological defects in ion Coulomb crystals [1] several groups have reported on the creation of stable kinks [2, 3, 4, 5] within a short period of time. Kink defects have been created either during the crystallization of a laser cooled Coulomb crystal [2] or by driving the second-order phase transition from a linear to a zigzag ion configuration [3, 4, 5]. The latter method was used to investigate the scaling of kink formation rates in relation to the Kibble-Zurek mechanism [6, 7] as proposed in [8]. Further studies focussed on the dynamics of kinks, the influence of mass defects and

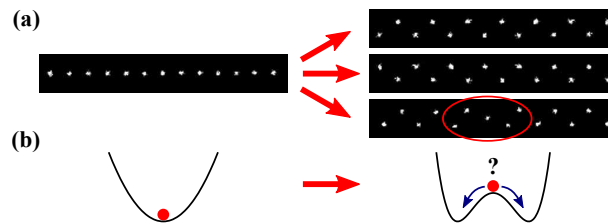


Figure 1. – (a) Illustration of the phase transition from the radially symmetric linear phase (left) to the symmetry broken zigzag phase (right). For the symmetry broken phase there are two different degenerate states: ‘zigzag’ (top right) or ‘zagzig’ (centre right). Different choices at spatially separated regions lead to topological defects (bottom right). (b) The phase transition can be described by a system, where the confinement changes from a simple harmonic potential (left) to a double well potential (right).

electric fields [9, 10]. Kink solitons have also been proposed as a tool for storing quantum information [11], for the generation of entanglement [12] and to study quantum phase transitions [13].

This article summarizes the results of our work on kinks in ion Coulomb crystals published in [3, 9] and is structured as follows. In section 2, we first discuss how different types of kinks can be created experimentally. In section 3, the results of our test of the inhomogeneous Kibble-Zurek mechanism [8] are presented. In section 4, we explain the stability and dynamics of kinks with the help of the Peierls-Nabarro (PN) potential. In section 5, we show that an implanted mass defect can trap kinks at its location in the ion chain. As discussed in section 6, the effect of mass defects can be modified by an additionally applied electric field. We show methods using this controllable modification to manipulate kinks and to create them in a deterministic way.

2. – Creation of topological defects in ion Coulomb crystals

For our experiments we load and laser cool around 30 $^{172}\text{Yb}^+$ ions in a linear segmented Paul trap. The trap is designed to achieve minimal micromotion at the trap axis for long linear ion Coulomb crystals [14, 15]. We start the experimental sequence in the linear phase with an axial trapping frequency of $\nu_z = (24.5 \pm 0.5)$ kHz and initial radial frequencies $\nu_{x,i} \approx \nu_{y,i} \approx 500$ kHz. If the radial frequencies are reduced below a critical value ν_{crit} the linear chain buckles into a zigzag configuration. The critical frequencies can be derived using $\nu_{\text{crit}} \approx 0.73 \nu_z \times N^{0.86}$, where N is the number of ions [16].

To create kinks probabilistically the radial trapping frequencies are ramped down to a value $\nu_{x,f} < \nu_{\text{crit}}$ with ramp times on the order of several tens of μs . To confine the zigzag to a well-defined plane, an asymmetry in the radial potential is applied such that $\nu_{y,f}/\nu_{x,f} \approx 1.3$. When the critical frequency is passed the ions arrange themselves in a zigzag configuration. As depicted in fig. 1, the system does have two degenerate choices for the broken symmetry phase. Locally separated regions in the ion chain that can not communicate this choice will choose their state independently. If the choices are

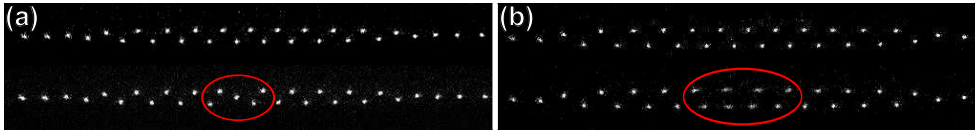


Figure 2. – Experimentally observed ion configurations. The kinks (indicated by red ellipses) are created by a quench of the radial potential and then imaged onto a CCD camera with exposure times of 40 ms. (a) Zigzag and localized kink configuration for $\nu_{x,f}/\nu_z \approx 8$. (b) Zigzag and extended kink configuration for $\nu_{x,f}/\nu_z \approx 5.5$.

incompatible, topological defects will form at the boundary of these regions (figs. 1 and 2).

Depending on the ratio of the final radial to the axial trapping frequencies $\nu_{x,f}/\nu_z$ we observe two different stable kink configurations in molecular dynamics simulations as well as in the experiment (fig. 2). For higher ratios $\nu_{x,f}/\nu_z$ the kinks have a localized structure, where one ion is placed between the two rows of the zigzag (see fig. 2a). If the ratio is lowered the kink converts into a more extended structure as shown in fig. 2b. In molecular dynamics simulations we observed that as the critical point is crossed all kinks first appear as localized kinks and while the radial potential is lowered further transform into extended kinks. As will be discussed in sec. 4 in more detail, extended kinks are more stable than localized ones, i.e. the probability of a kink moving out of the chain is smaller for extended kinks. Because of this the scaling of kink creation rates was tested with extended kinks.

3. – Kink densities and the Kibble-Zurek mechanism

As the transition from the linear to the zigzag phase is a second-order phase transition [17], ion Coulomb crystals have been proposed to test the Kibble-Zurek mechanism [8]. This universal theory [6, 7] is applicable to all second-order phase transitions independent of the microscopic structure of the considered system. In fact, a wide range of different systems have been investigated to test its predictions [18, 19] (see also supplementary part of [3]).

The Kibble-Zurek mechanism employs equilibrium thermodynamics to describe non-equilibrium processes. When a system crosses a second-order phase transition the relaxation time τ and the healing length ξ diverge. The main assumption of the theory is, that the system freezes out, when the relaxation time $\tau(\hat{t})$ is equal to the time \hat{t} left for the system to reach the critical point. The healing length at that instant $\xi(\hat{t})$ is expected to be the average domain size after the phase transition. The full calculation [7] results in a power law scaling $\xi(\hat{t}) \propto \tau_Q^{\nu/1+\nu z}$, with critical exponents ν and z . In our case the quench time $\tau_Q = t_{\text{ramp}}/2$.

This description is only valid for homogeneous systems. The main difficulty of testing the theory experimentally is the typically small scaling exponent. To be sensitive to the small exponent the quench time τ_Q has to be varied over a large range. In inhomogeneous systems the scaling can be enhanced [8]. For the case of ion Coulomb crystals a scaling

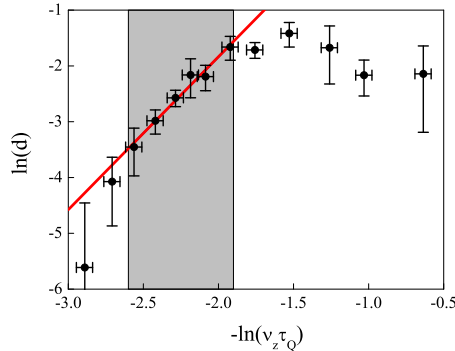


Figure 3. – Double logarithmic plot of experimentally measured kink densities d versus the quench time τ_Q . In the shaded region losses are negligible. A linear fit gives a scaling factor $\sigma_{\text{exp}} = 2.7 \pm 0.3$. Uncertainties of the defect densities are statistical errors.

of the density of kinks d with the quench rate of $d \propto \tau_Q^{-1/3}$ for the homogeneous case and $d \propto \tau_Q^{-4/3}$ for the inhomogeneous case was predicted [8]. The kink density d for finite systems is given by the ratio of the system size to the average domain size $\hat{\xi}$.

In our experiment we load 27 to 31 ions. The small fluctuation of the ion number is not relevant as the maximal change of the critical frequency is only about 40 kHz and does not affect the rate at which the phase transition is crossed. In our experiment we load 27-31 ions and vary the quench time t_Q from 12.5 to 150 μs . After quenching the crystal is imaged onto a EMCCD camera with an exposure time of 40 ms. For each quench time τ_Q the experimental cycle is repeated up to 4400 times. We derive the kink density as the average number of kinks per quench cycle. Depending on the quench time kink densities between 0.01 and 0.24 have been observed. As Kibble-Zurek theory only describes how many kinks are created, we investigated losses of kinks after the quench using molecular dynamics simulations. Therefore we evaluated the number of kinks directly after crossing of the critical point and after an additional time of 350 μs . It was found that for slow and fast quenches significant losses appear, but in a region in between they can be neglected. In fig. 3 the experimental results are shown in a double logarithmic plot. In the region with negligible kink losses ($-\ln(\nu_z \tau_Q) = -1.9$ to -2.6) a linear fit gives a slope $\sigma_{\text{exp}} = 2.7 \pm 0.3$ which is in good agreement with the value obtained from simulations $\sigma_{\text{sim}} = 2.63 \pm 0.13$. However, this does not match the theoretically expected slope $\sigma_{\text{theo}} = 4/3 \approx 1.33$, but agrees with twice this value. In fact, a doubling of the critical exponent has been previously observed in homogeneous systems for the case when at maximum one defect per quench is produced [19, 20]. This is also the case in our experiment and could be an explanation for the observed steeper scaling.

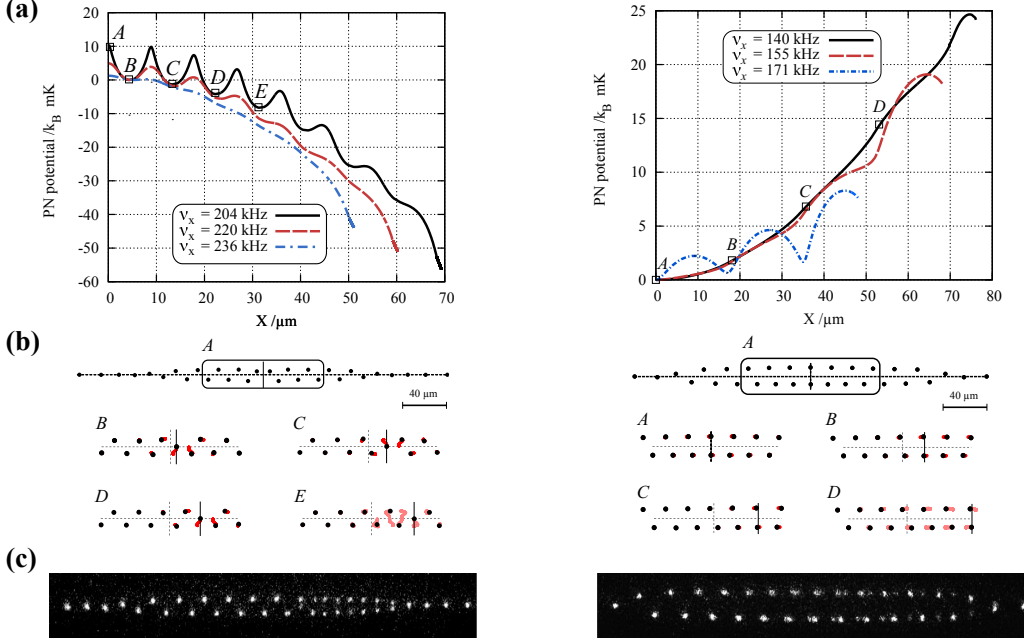


Figure 4. – (a) Peierls-Nabarro potentials for localized (left) and extended kinks (right) from [9]. Simulations were done for 30 ions in a harmonic trap with $\nu_z = 24.6$ kHz and radial potentials given in the legends. The black lines correspond to our experimental parameters. (b) Simulated kink configurations at different kink positions. The corresponding PN potentials are marked in the plots with squares. Solid black lines indicate kink positions and dashed lines show the centre of the crystal. Red traces indicate ion movement to the next depicted configuration. In the last frame E(D) the full trajectories B-E(A-D) are shown. (c) Experimental observation of kinks leaving the ion chain. Localized kinks (left) move by transverse motion of the ions and extended kinks (right) move by axial motion of the two rows against each other. The observed time averaged motion of the ions matches with the simulation results.

4. – The Peierls-Nabarro potential and kink stability

In order to be able to use kinks in ion Coulomb crystals as a storage of quantum information or for the creation of entanglement, it is necessary to get a better understanding of their stability and dynamics. Therefore it is useful to derive the so called Peierls-Nabarro (PN) potential [21]. The PN potential is given by the overall potential energy of the crystal as a function of the position of the kink centre. One point of the PN potential can be derived numerically by minimizing the energy of a crystal under the constraint that the kink is at a fixed, given position. A more detailed description how to compute the PN potentials for ion Coulomb crystals can be found in [9].

Fig. 4 shows PN potentials for different values of the radial trapping frequency $\nu_{x,f}$. For infinite homogeneous systems a periodic potential is expected, because the system is invariant under a translation of an integer multiple of the lattice spacing [21]. For finite

inhomogeneous systems this behaviour is changed due to the non-constant lattice spacing and the boundaries of the system. The PN potentials for localized kink structures are shown in fig. 4a). At the centre of the chain ($X = 0$) the expected periodic structure of the potential is visible. The height of the potential barriers increases when the radial trapping frequency $\nu_{x,f}$ is decreased. The potential tends to decrease as the kink is moving away from the centre. A kink can be trapped at the local minima of the potential, but if it has enough energy to move over a local maximum to the next lattice site further away from the centre, it is likely to move out of the zigzag region.

For the extended kink configurations (fig. 4b) the shape of the PN potential changes. For ($\nu_{x,f} = 171$ kHz) the periodic structure of the potential is still visible, but with an approximately two times larger period. The periodicity of the potential vanishes, if the axial frequency $\nu_{x,f}$ is reduced further. The main difference to the localized case is, that the potential is now increasing as the kink moves away from the centre, making it an overall trapping potential. The potential barrier a kink has to overcome in order to move out of the chain increases with decreasing axial trapping frequency $\nu_{x,f}$. This explains, why in the experiment kinks exclusively stabilize at the centre of the chain. This also makes it almost impossible to have two stable extended kinks at the same time, because after creation both kinks will move to the centre and annihilate.

For the explanation of kink losses (see section 3) it is important to consider the time dependence of the PN potential as the radial confinement is ramped down further after the kink creation. The initially created localized kink can be lost easily, because of the low potential barriers. As the radial potential is reduced further and the kink transforms to the extended structure the PN potential barrier increases and stably traps kinks. Hence, for slow quenches the build up of the potential barrier is not fast enough, so that kinks move out of the chain before they can be trapped. On the other side for fast quenches the energy introduced by the quench is sufficient to overcome the PN potential barrier even after the ramp is finished. The interplay between the build up of the PN potential, the initial kink energy and the energy introduced due to the quench is very complex and needs further investigation.

5. – Influence of mass defects

Next, we discuss the influence of mass defects on kinks. It arises from the fact that the radial secular frequency is mass dependent $\nu_x \propto 1/m$. Therefore, an ion with a deviating mass experiences a different overall potential and will distort the ion configuration. This distortion also leads to a modification of the PN potential. Here, we focus our discussion on the effect of mass defects on extended kinks. The influence on both kink types is discussed in more detail in [9].

Experimentally mass defects appear as molecular ions, which are formed during collisions of the ions with background gases. The molecules appear in the fluorescence images as dark ions. $^{172}\text{Yb}^+$ can react with water and form either YbO^+ or $\text{Yb}(\text{OH})^+$ or other molecules [22, 23]. In the experiment we determined the molecule masses via parametric excitation. Here we could primarily detect the formation of YbO^+ or $\text{Yb}(\text{OH})^+$, where

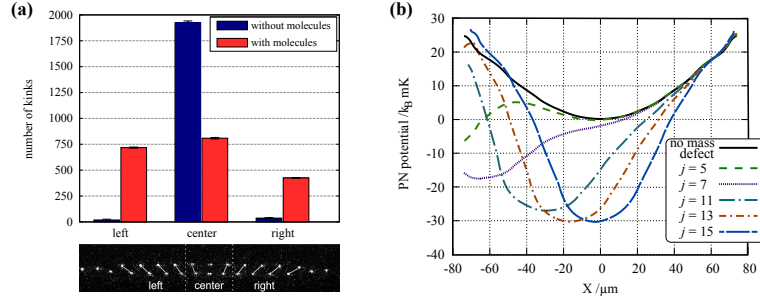


Figure 5. – Influence of mass defects on kinks. (a) Experimentally observed kink positions with and without mass defects. The data indicate that the presence of molecules leads to stably trapped kinks outside the center of the ion crystal. Bottom: Definition of left, centre and right region. (b) PN potentials for extended kinks without and with mass defects ($m = 220$ u) at different positions j . In the simulations the ions are numbered in axial direction starting with $j = 0$ for the leftmost ion. Hence for the simulated 30 ions $j = 14, 15$ correspond to the two central ions. The minima of the potentials are located at the position of the mass defect. Experimental parameters were used for the calculations.

the addition of hydrogen was not resolvable. As an independent method of measuring the mass of molecules we compared the distortion of ion configurations in the experiment with configurations resulting from simulations. Using these methods we have identified even heavier masses involving up to three oxygen atoms. Therefore representative masses of $m = 188$ u and $m = 220$ u were chosen for the simulations.

A first experimental evidence that mass defects do have a significant influence on kinks can be extracted from fluorescence pictures by comparing the spatial distribution of kinks in ion chains with and without mass defects (fig. 5a). As already discussed in section 4, without mass defects the kinks almost always stabilize in the centre of the crystal. In contrast to this, with mass defects the positions of the kinks are more evenly distributed. This behaviour is a clear indication that mass defects affect the PN potential.

Calculated PN potentials for ion chains with mass defects placed at different positions are compared to the PN potential for a pure crystal in fig. 5b). The PN potentials show a local minimum at the position of the mass defect. This explains the spatial distribution of kinks as the mass defects in our experiment are randomly placed. Another effect is that the potential depth with a mass defect is significantly larger, if the mass defect is placed not too far from the centre (e.g. $j = 11, 13, 15$). For positions further away from the centre (e.g. $j = 5$) the minimum at the position of the mass defect also reduces the PN potential barrier leading to an increase of kink losses [9].

Mass defects do not only affect the PN potential, but also the creation of kinks. The lower radial potential for heavier ions initiates the phase transition earlier at the site of the mass defect. The consequences do depend strongly on the position of the molecule. If the molecule is at the centre, it will slow down the phase transition front and hence less kinks are produced. For mass defects outside the centre, it leads to an enhanced

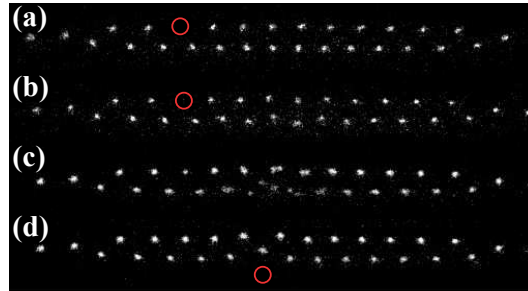


Figure 6. – Experimental images showing a kink moving together with a molecule. We used 20 ms exposure time and had 20 ms dead time between two images. (a) A kink in the centre is created through a radial quench. A molecule (indicated by a red circle) is placed on the left. (b) Ion configuration after adiabatic application of an electric field with field vector lying in the zigzag plane and pointing downwards in the image. (c) The crystal is heated by tuning the cooling light closer to the resonance. The additional energy lets the kink oscillate and move to the molecule position. Once the kink attaches to the mass defect, the heavy molecule is pushed away from the trap axis due to the higher charge density of the kink and is pulled towards the centre of the harmonic axial confinement, where the kink stabilizes (d).

kink creation as two phase fronts collide. Further details of the influence of mass defects on kink creation can be found in [9].

6. – Mass defects and electric fields

Finally, we focus on the effects of mass defects with externally applied electric fields. As the radial potential decreases with higher masses the position shift of the ions due to an additional electric field in the radial direction is also mass dependent. This means that a heavy molecule can be displaced with respect to the $^{172}\text{Yb}^+$ ions by adding an electric field in the radial direction. The amount of the displacement can be increased by increasing the field strength. The behaviour of a molecule with an applied electric field is similar to the behaviour of a molecule with increased effective mass. Hence, electric fields give us a handle to manipulate and control kinks actively.

The first experimental sequence (see fig. 6) allows to move a mass defect with the help of a kink to the centre of the ion chain. It starts with a kink and a molecule in the ion chain (fig. 6a) and without any additional electric fields. To enhance the trapping effect of the molecule an electric field is now applied adiabatically (fig. 6b). Then the red detuning of the cooling light is reduced by some MHz. This leads to heating of the whole crystal and provides the kink with kinetic energy (fig. 6c). If the kink moves to the molecule site, the higher charge density of the kink pushes the molecule further out of the zigzag. At a certain displacement of the molecule the force of the overall axial trapping potential becomes stronger than the repulsion due to the neighbouring ions. Hence, the molecule moves together with the kink to the axial centre of the trap, because the PN potential minimum is always at the molecule position (fig. 6d). The electric field strength

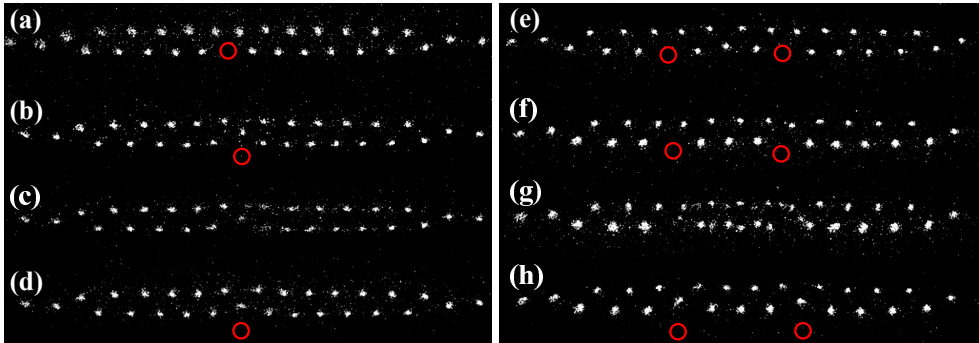


Figure 7. – Two experimental time series (a-d and e-h) demonstrating kink creation with a ramp of the electric field. (a) Zigzag with mass defect located at the centre of the chain (indicated by red circle). (b) After application of the electric field ramp the molecule is displaced and two kinks are created. One at the position of the molecule and one just to the right of it. (c) The kink not attached to the molecule moves to the right and leaves the chain. (d) Only the kink attached to molecule remains. (e) Zigzag with two mass defects. (f) After application of an electric field ramp the two molecules are displaced. On the right side an ion is already pulled to the emerging vacancy left from the molecule. (g) Two kinks are created at the right mass defect. (h) The two kinks stabilize at the molecule positions.

needed to induce this movement depends on the mass and the position of molecule. Using simulations we found minimal electric field values ranging from $\sim 10 \text{ V m}^{-1}$ ($m = 220 \text{ u}$) to $\sim 100 \text{ V m}^{-1}$ ($m = 188 \text{ u}$). The induced excess micromotion and the resultant temperature increase due to rf-heating is still small compared to the energy needed to move the kink.

The second method allows to create kinks in a deterministic way without quenching of the radial potential. Starting point is a crystal in the zigzag phase with at least one mass defect (see figs. 7a, 7e). Now we adiabatically add an electric field (figs. 7b, 7f). This causes the molecule to move out of the zigzag radially. When the mass defect leaves its original position two kinks are created, one being directly attached to the molecule. To get a better understanding of this mechanism it is useful to think of lattice sites. When the molecule leaves the zigzag this produces a vacancy defect at its original position and an interstitial defect, because there is no other available place in the zigzag. Both defects are unstable and convert into kinks immediately. Another interpretation is to think of the creation of a kink and an anti-kink. In order to use the kink for further experiments, where small micromotion amplitudes are needed, the electric field can be switched off again without losing the kink. These two and other methods using electric fields for kink manipulation are discussed in [9] in detail.

7. – Conclusion

We experimentally demonstrated the creation of two different kink configurations via quenching of the radial trap potential. We investigated the kink creation rates in dependence of the quench time and found an exponential scaling in a regime, where at maximum one defect at a time is produced. The observed scaling factor is twice as big as the scaling factor predicted for inhomogeneous systems. The experimentally observed differences of localized and extended kinks were explained by the different Peierls-Nabarro potentials. We showed that heavy mass defects are able to trap kinks, because of the generation of local minima in the PN potential. In addition, we demonstrated how the application of electric fields opens up ways to control kinks actively. We demonstrated experimental sequences that allow for a controlled preparation and creation of kinks.

The results of our work will help to experimentally study kink-kink interaction and studies of kinks as carriers of quantum information [11, 12]. Ultimately, ion Coulomb crystals can be used to investigate non-linear quantum-many-body systems and quantum phase transitions [13, 24].

REFERENCES

- [1] SCHNEIDER C., PORRAS D. and SCHÄTZ T., *Rep. Prog. Phys.*, **75** (2012) 024401.
- [2] MIELENZ, M. AND BROX, J. AND KAHRA, S. AND LESCHHORN, G. AND ALBERT, M. AND SCHÄTZ, T. AND LANDA, H. AND REZNIK, B., *Phys. Rev. Lett.*, **110** (2013) 133004.
- [3] PYKA K., KELLER J., PARTNER H. L., NIGMATULLIN R., BURGERMEISTER T., MEIER D. M., KUHLMANN K., RETZKER A., PLENIO M. B., ZUREK W. H., DEL CAMPO A. and MEHLSTÄUBLER T. E., *Nature Commun.*, **4** (2013) 2291.
- [4] ULM S., ROSSNAGEL J., JACOB G., DEGÜNTHER C., DAWKINS S. T., POSCHINGER U. G., NIGMATULLIN R., RETZKER A., PLENIO M. B., SCHMIDT-KALER F. and SINGER K., *Nature Commun.*, **4** (2013) 2290.
- [5] EJTEMAEE S. and HALJAN P. C., *Phys. Rev. A*, **87** (2013) 051401(R).
- [6] KIBBLE T. W. B., *J. Phys. A:Math. Gen.*, **9** (1976) 1387.
- [7] ZUREK W. H., *Nature*, **317** (1985) 505.
- [8] DEL CAMPO, A. AND DE CHIARA, G. AND MORIGI, G. AND PLENIO, M. B. AND RETZKER, A., *Phys. Rev. Lett.*, **105** (2010) 075701.
- [9] PARTNER H. L., NIGMATULLIN R., BURGERMEISTER T., PYKA K., KELLER J., RETZKER A., PLENIO M. B. and MEHLSTÄUBLER T. E., *New J. Phys.*, **15** (2013) 103013.
- [10] LANDA H., REZNIK B., BROX J., MIELENZ M. and SCHÄTZ T., *New J. Phys.*, **15** (2013) 093003.
- [11] LANDA H., MARCOVITCH S., RETZKER A., PLENIO M. B. and REZNIK B., *Phys. Rev. Lett.*, **104** (2010) 043004.
- [12] LANDA H., RETZKER A., SCHÄTZ T. and REZNIK B., *arXiv:1308.2943*, (2013) .
- [13] SILVI P., CALARCO T., MORIGI G. and MONTANEGRO S., *arXiv:1311.2510*, (2013) .
- [14] PYKA K., HERSCHBACH N., KELLER J. and MEHLSTÄUBLER T. E., *Appl. Phys. B*, (2013) 1.
- [15] HERSCHBACH N., PYKA K., KELLER J. and MEHLSTÄUBLER T., *Appl. Phys. B*, **107** (2012) 891.
- [16] STEANE A. M., *Appl. Phys. B*, **64** (1997) 623.

- [17] FISHMAN S., DE CHIARA G., CALARCO T. and MORIGI G., *Phys. Rev. B*, **77** (2008) 064111.
- [18] DEL CAMPO A. and ZUREK W. H., *arxiv:1310.1600*, (2013) .
- [19] MONACO R., MYGIN J., RIVERS R. J. and KOSHELETS V. P., *Phys. Rev. B*, **80** (2009) 180501(R).
- [20] SAITO H., KAWAGUCHI Y. and UEDA M., *Phys. Rev. A*, **76** (2007) 043613.
- [21] BRAUN O. M. and KIVSHAR Y. S., *The Frenkel-Kontorova model, concepts, methods, and applications* (Springer) 2004.
- [22] SUGIYAMA K. and YODA J., *Jpn. J. Appl. Phys.*, **34** (1995) L584.
- [23] RUTKOWSKI P. X., MICHELINI M. C., BRAY T. H., RUSSO N., MARALO J. and GIBSON J. K., *Theor. Chem. Acc.*, **129** (2011) 575.
- [24] RETZKER A., THOMPSON R. C., SEGAL D. M. and PLENIO M. B., *Phys. Rev. Lett.*, **101** (2008) 260504.

7. Summary and Outlook

The work presented in this thesis contributes to the development of an optical multi-ion clock. The aim of the experiment is to reduce the clock instability by probing multiple $^{115}\text{In}^+$ clock ions simultaneously. The proposed clock uses mixed species ion Coulomb crystals, where $^{172}\text{Yb}^+$ ions are used to sympathetically cool multiple $^{115}\text{In}^+$ clock ions. In order to achieve low systematic uncertainties also for a spatially extended Coulomb crystal, a novel linear Paul trap design was introduced in Ref. [27]. The first prototype traps with this design have been presented and characterized in [29, 30].

Within this work, the objectives of the trap development have been presented. The first design goal was to minimize axial rf fields as these cannot be compensated and cause varying time dilation shifts along the ion crystal. In order to study effects of different trap designs and geometrical imperfection and to reduce the axial rf fields, FEM calculations have been used. The EMM measurements showed that the results of the FEM calculations are reasonable and are able to predict the axial rf fields of different trap designs. The observed differences between the measured and simulated axial micromotion amplitudes can be explained by the remaining trap geometry imperfections. In comparison to the prototype trap, the micromotion amplitudes could be reduced substantially. For the measurement of the micromotion amplitude along the axial trap axis a single ion has been shifted to different positions by adjusting the axial trap potential. Further investigations with the same trap, which are not part of this work and have been done during writing this thesis, could demonstrate that the simultaneous measurement of micromotion on a linear ion Coulomb crystal gives identical results [89].

Another trap design goal was to reduce the uncertainty of the trap temperature increase as this contributes the BBR shift uncertainty. The rise of the trap temperature is caused by resistive and dielectric losses of the rf voltage that is driving the ion trap. The temperature rise has been improved by selecting AlN as wafer material which offers a low dielectric loss tangent together with a high thermal conductivity. Additionally, each trap has been equipped with two calibrated Pt100 temperature sensors allowing precise trap temperature measurements. Comparisons of the measured and simulated temperatures of trap II allowed to identify thin gold layers, poor thermal contacts and contaminations as the cause for additional trap heating. These points could be improved by small changes to the trap design and manufacturing process and hence trap III and IV showed a significantly lower temperature increase. Experimental and simulation results indicate that resistive losses are now the dominant heating source. A further improvement is therefore expected by an increased gold layer thickness.

The third important trap design objective has been the minimization of external ion heating rates. The heating rate contributes to the uncertainty of the ion temperature and increases the time dilation shift uncertainty. The observed heating rates have been achieved by selecting a rather large ion-electrode distance of 0.707 mm and by the use of heavily filtered low noise dc electronics. The ion heating rate has been measured at three different trap frequencies. The frequency scaling follows the typically expected $1/f$ noise. The comparison to the prototype trap shows that the ion heating rate of the AlN trap is at the same level. A comparison to other experiments shows that the measured heating rates are among the best of the reported values [66]. For the measurement of the heating rate, a single $^{172}\text{Yb}^+$ ion has been cooled to the motional ground state. For this a continuous sideband cooling scheme has been implemented and characterized. Precise frequency control of the repumping laser at 1650 nm is needed for the implementation of this cooling method. To allow for measurement and control of the wavelength with the available precision wavemeter, a frequency doubling cavity was setup and has been characterized.

Another achievement of this work is the development of a reliable and repeatable trap manufacturing process. This was achieved by close cooperation with PTB's scientific instrumentation department. The process has been described and documented in detail. In total five AlN ion traps have been manufactured (see Tab. 3.4). In the course of the production of these traps, the manufacturing process has been optimized. Measurements of the wafer and trap geometry show that the geometric imperfections are mainly within the targeted error bands. Compared to the prototype traps, the geometric errors could be reduced significantly, enabling the measured low micromotion amplitudes.

In Tab. 7.1, the expected trap related frequency shifts and their uncertainties for a single $^{115}\text{In}^+$ ion are summarized. This shows that the trap is well suited for reducing the uncertainty of single ion clocks to below 1×10^{-19} . For a multi-ion clock additional effects have to be considered for these shifts. Because of the axial length of a linear chain of ions the EMM amplitudes will differ for each ion. Thus, there is a spread of frequency shifts between the ions which will also increase the associated uncertainty. The final value of the uncertainty depends on the selected length of the ion chain and based on Fig. 5.6 it will increase for longer Coulomb crystals. In contrast, the BBR shift and its uncertainty is considered to be independent from the ion position along the trap axis and will stay at an equal level also for a multi-ion clock. The total frequency shift due to the external heating rate depends on the choice of the three trap frequencies. The measured results show that the heating rate scales with $\frac{1}{\omega_{\text{sec}}}$ and thus higher radial trap frequencies produce lower frequency shifts. For the proposed multi-ion trap, the axial trap frequency will be much lower than the radial in order to form a linear ion chain. The external heating rate in axial direction has not been measured so far. As an estimate the extrapolation of the measured radial heating rate to an axial trap frequency of $\omega_{\text{ax}} = 2\pi \times 30 \text{ kHz}$ yields a frequency shift of $(2.7 \pm 0.2) \times 10^{-19}$. Because of the size of the expected shift, a direct measurement of

type of shift	shift (1×10^{-19})	uncertainty (1×10^{-19})
time dilation (EMM)	-0.79	0.43
blackbody radiation at $T = 293.15$ K	-124.5	0.14
ion heating rate (per second)	-0.21	0.03
total trap related shifts	-125.5	0.45

Table 7.1.: Estimated trap related relative frequency shifts for a single $^{115}\text{In}^+$ ion at $U_{\text{rf}} = 750$ kV. For the uncertainty of the BBR shift only the uncertainty of the temperature is considered and the uncertainty of the polarizability $\Delta\alpha_s$ is neglected. The shift due to the ion heating rate only includes the heating on a single trap axis with $\omega_{\text{sec}} = 2\pi \times 490$ kHz.

the axial heating rate will be needed. This is experimentally more challenging, because the ground state cooling starts with higher phonon numbers and further outside the Lamb-Dicke regime.

In a later experimental work by Keller et al. [93], which is not part of this thesis, two possible experimental configurations are assumed for a multi-ion clock within the presented ion trap. An ion crystal with 10 $^{115}\text{In}^+$ ions and 3 $^{172}\text{Yb}^+$ is assumed. A detailed calculation of all relevant frequency shifts shows that a total frequency uncertainty of below 1×10^{-19} is achievable. For this low uncertainty, a precise measurement of the static polarizability $\Delta\alpha_s$ is required. This could be achieved by a measurement of the frequency shift due to irradiation of the ion with a strong IR laser. Similar experiments for the determination of $\Delta\alpha_s$ have been done in Refs. [8] and [26]. The remaining frequency uncertainty is then dominated by the time dilation shifts due to micromotion and thermal motion.

Further steps that are planned for the realization of a multi-ion trap are the installation of a new and more compact vacuum chamber that allows better optical access and the installation of magnetic shielding. The magnetic shielding together with a set of Helmholtz coils will allow to realize the needed homogeneity and low noise level of the magnetic field. This new setup will use ion trap V (see Tab. 3.4) and the characterization of this trap will show whether the trap temperature increase and the micromotion amplitudes are reproducible. For the spectroscopy on multiple $^{115}\text{In}^+$ ions, the state detection on the intercombination line $^1\text{S}_0 \leftrightarrow ^3\text{P}_1$ with the EMCCD camera has to be implemented. This will then allow to simultaneously measure the temperature of each ion in a mixed species ion Coulomb crystal, which is needed to characterize the time dilation shift due to thermal motion.

Besides these preparatory tasks for the realization of a multi-ion clock, the trap also provides an ideal test bed for studying many-body physics with trapped ions. This has first been demonstrated in the previous work by Pyka [30, 94]. These experiments utilize the similarity of ion Coulomb crystals to a solid-state crystals. The advantage of ion crystals is that they provide a much better possibility to control the system and also allow a simple single ion excitation and readout. The results presented in

Chapter 6, which also includes a review of the previous work of Pyka et. al [94], show how topological defects can be created in 2-dimensional Coulomb crystals and how they are affected by mass defects and externally applied electric fields. Furthermore it has been shown how topological defects can be created deterministically. This will be helpful for further experiments as these types of topological defects exhibit localized high frequency modes with long decoherence times, which could be used for the implementation of quantum information protocols [95]. The trap also has been used to study nanofriction and Aubry-type transitions from a sticking to a sliding phase [96]. Further investigations published in Ref. [97] showed that this transition is sensitive to an asymmetric axial trap potential. These asymmetries have been observed for the prototype trap and have been found to be negligible for trap IV. Thus, also such experiments benefit from lower trap manufacturing tolerances.

Further applications of optical clocks in general also illustrate further long-term goals for the presented experiment. Among these applications is the search for new physics beyond the standard model and for possible violations of general relativity [16–19]. In Ref. [20] it has been proposed to use the Yb^+ octupole transition to test local Lorentz invariance with an unprecedented level of accuracy. Multi-ion clocks and their improved instability also are well suited for the emerging field of chronometric levelling [22, 23], where the gravitational red shift of an atomic resonance frequency is used to measure the local gravitational potential of the Earth. The experiment described in Ref. [98] uses an almost identical trap design to build a transportable Al^+ ion clock. For these kind of experiments, a low clock instability is especially desirable in order to resolve fluctuations of the gravitational potential. Finally experiments on quantum simulations with ions [99, 100] could also profit from the presented ion trap properties. These types of experiments will benefit from long coherence times (possible through low micromotion levels and low ion heating rates) and the possibility to store multiple ion strings simultaneously in different trap segments.

A. Appendix

A.1. Trap Dimensions of Trap Potential Simulator

parameter	design value	FEM model
L	29 mm	29 mm
d	1.000 mm	1.000 mm
t_{RF}	1.000 mm	1.015 mm
t_{PK}	0.128 mm	0.120 mm
t_w	0.380 mm	0.398 mm
l_n	1 mm, 2 mm	1.010 mm, 2.005 mm
$w_n = w_{n,\text{ion}} = w_{n,\text{back}}$	0.100 mm	0.090 mm
depth of electrodes	-	5 mm

Table A.1.: Comparison of the design values of the most important trap dimensions with the values used for the FEM calculations. The dimensions for the FEM calculations are adapted to resemble the measured trap geometry as closely as possible. The depth of the electrodes is the dimension along the y -axis.

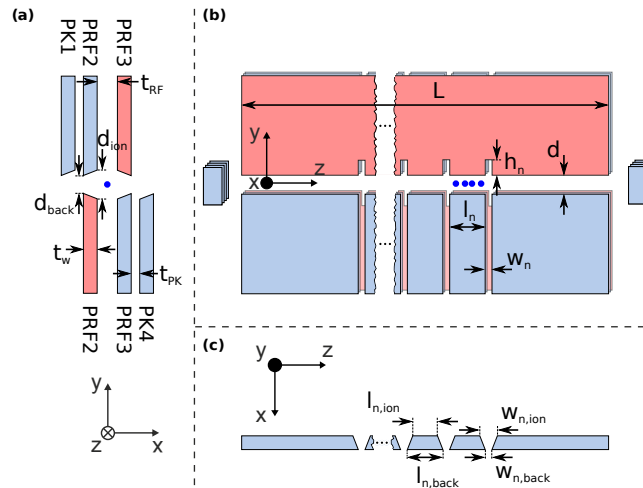


Figure A.1.: Drawings of the trap electrodes, which show all important geometric dimensions and the chosen orientation of the coordinate system.

A.2. Aluminium Nitride Material Properties

property	value
medium grain size	4–5 μm
surface roughness R_a	0.05 μm
thickness trap wafer	(380 \pm 25) μm
thickness thick spacer	(1000 \pm 25) μm
thickness thin spacer	(127 \pm 13) μm
parallelism trap wafer	0.15 mrad
parallelism spacer	0.09 mrad
bulk density	3.3 g/cm ³
thermal conductivity	170 W m ⁻¹ K ⁻¹
thermal expansion coefficient	4.7 \times 10 ⁻⁶ K ⁻¹
relative permittivity	8.9
loss tangent tan δ	
data sheet value	4 \times 10 ⁻⁴
estimated values Sec. 5.1	
trap 2 [76]	8 \times 10 ⁻⁴
trap 3 and 4	5 \times 10 ⁻⁵
break down voltage	16 kV mm ⁻¹

Table A.2.: Properties of the polished Aluminium Nitride Material. If not stated otherwise the values correspond the data sheet values from the supplier Valley Design Corporation.

A.3. DC Voltage Supply - Circuit Diagram

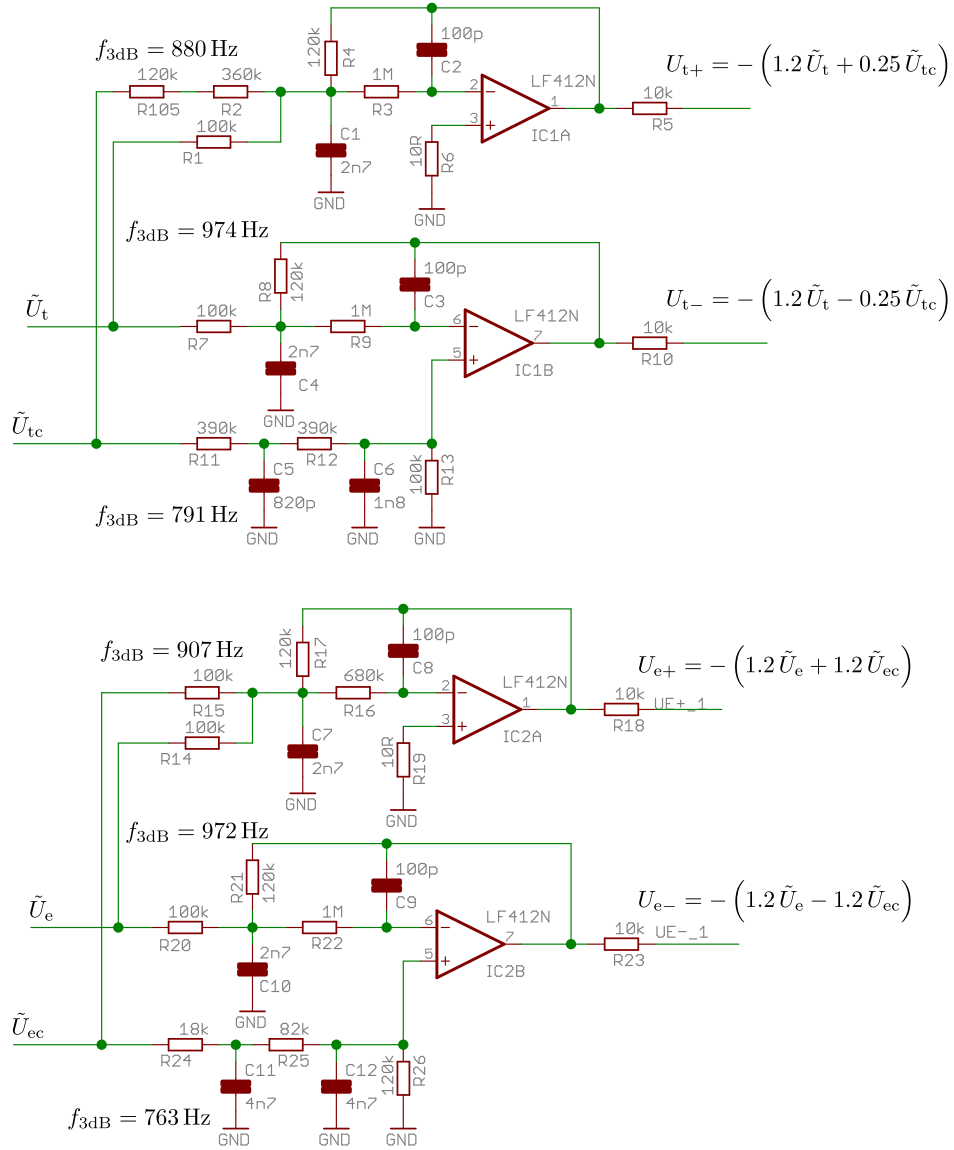


Figure A.2.: Circuit diagram of the self built analogue circuit for the generation of the dc trap voltages. Each signal path includes a second-order low-pass filter with cut-off frequencies f_{3dB} shown in the drawing. As the resistances define the amplification factor, precision resistors with tolerance of 0.1% have been selected. The operational amplifiers are from Texas Instruments LF412N.

A.4. Calibration of Temperature Sensors on Trap IV

For a precise determination of the trap temperature two Pt100 platinum resistance temperature detector (RTD)¹ are directly soldered onto the two PRF trap chips (see Fig. 3.3 and Fig. 3.7). This type of sensor makes use of the temperature dependent electrical resistance $R(T)$. Typically this relation is approximated by a second order polynomial

$$R(T) = R_0 (1 + AT + BT^2), \quad (\text{A.1})$$

where the temperature T is measured in °C. For temperatures above 0 °C the inverse relation is given by

$$T(R) = \frac{-R_0A + \sqrt{(R_0A)^2 - 4R_0B(R_0 - R)}}{2R_0B}. \quad (\text{A.2})$$

Because the temperature uncertainty given by the manufacturer ($\sigma_{T,\text{man}} \approx 0.3^\circ\text{C}$) is too large for a precise temperature measurement, a calibration was performed to find more accurate values for the coefficients R_0 , A and B . Therefore, after the finished assembly trap IV was mounted inside a cuboid made out of 10 mm thick copper sheets. Four reference temperature sensors with an absolute temperature uncertainty of $\sigma_{T,\text{ref}} \approx 0.007^\circ\text{C}$ have been used to measure the temperature of the copper cuboid at different positions. For thermal isolation the cuboid was wrapped with several layers of bubble wrap and placed inside a styrofoam box. This box was placed inside a cool box with an integrated Peltier element. The Peltier element was used to heat and cool the box to different temperature levels. For the resistance measurements, a calibrated precision digital multimeter² and the four-wire sensing method was used.

The resistances of the two sensors have been measured at eight different temperatures in the range between 19.7 °C and 34 °C. Fig. A.3 shows the results of these measurements and the result of a fit to the data using eq. A.1. The fit results for the parameters R_0 , A and B and the corresponding fit errors are listed in Tab. A.3. Error sources that have been accounted for are the self heating of the reference and the calibrated sensors, the temperature uncertainty of the individual reference sensors, the uncertainties of the resistance measurements, the temperature drifts during each measurement and the temperature gradient between the reference sensors. The dominant error source was the observed temperature gradient on the copper cuboid, which was increasing for higher temperatures. The calculated standard deviation between the four reference sensors was in the range of 8–25 mK. With Gaussian error propagation on eq. A.2 and the values from Tab. A.3 an absolute temperature uncertainty of 50–60 mK is derived. The temperature resolution that was achieved with the trap inside the vacuum chamber was below 1 mK. Thus, very small temperature changes can be detected with the calibrated sensors.

¹Heraeus Sensor Technology, SMD 0805FC

²Agilent 34401A

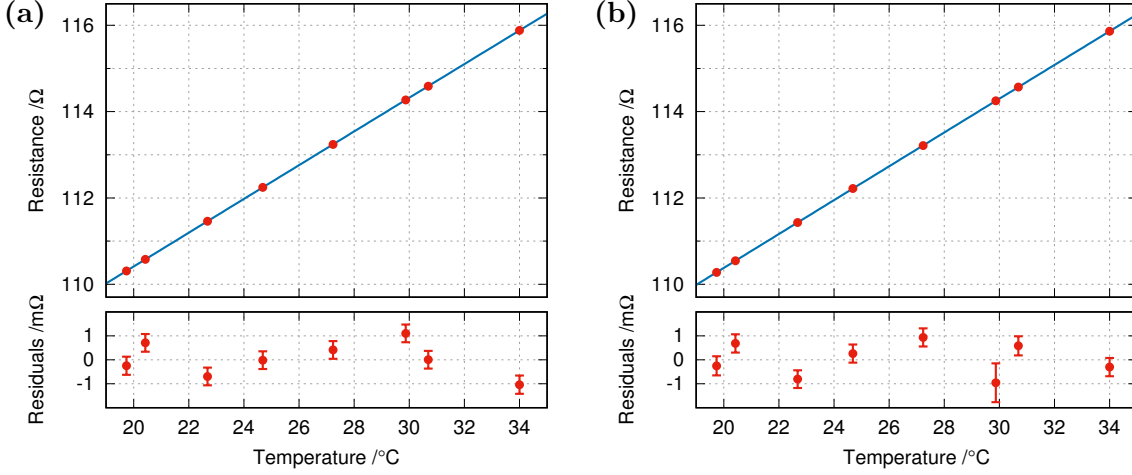


Figure A.3.: Results of the temperature calibration of the temperature sensors placed on (a) PRF2 and on (b) PRF3. The insets below show that the residuals are on the order of 1 mΩ. A difference in the resistance of 1 mΩ corresponds roughly to a temperature difference of 2.6 mK. The temperature uncertainties of the measurement points are in the range of 9–26 mK.

sensor	R_0	A	B
PRF2	102.530(11) Ω	$3.860(9) \times 10^{-3} \Omega/^\circ\text{C}$	$-8.9(17) \times 10^{-7} \Omega/^\circ\text{C}^2$
PRF3	102.478(12) Ω	$3.872(10) \times 10^{-3} \Omega/^\circ\text{C}$	$-8.8(18) \times 10^{-7} \Omega/^\circ\text{C}^2$

Table A.3.: Determined coefficients for the temperature sensors on trap IV.

A.5. Trap Potential Simulator

This section of the appendix describes the Matlab trap potential simulator program that has been developed for a reliable prediction of trap potentials for a given set of dc and rf voltages. It was inspired by a similar program, which was developed in the group of Jonathan Home at ETH Zürich. Their source code has been used as guideline for the program described here. The program takes the voltage configuration of the dc and rf voltages, calculates and graphically displays the resulting trap potential in the selected trap segment. As discussed in Sec. 5.2 the resulting trap potentials show good agreement to the experimentally measured potentials, if additional stray fields are taken into account.

In order to be able to compute the trap potential for all possible combinations of dc and rf voltages a simplified trap geometry with six segments (one 2 mm long segment, three 1 mm long segments and two end segments) was modelled with the FEM software Comsol Multiphysics. The simplification was necessary, because of the limited computational power that was available and the demanded high accuracy of the simulated data. Because of the mirror symmetry of the trap for in total 24 dc electrodes only 12 simulations are needed. For each simulation a voltage of 1 V was applied to a single electrode, while all other electrodes are grounded. The obtained output is the electric potential $\varphi(x, y, z)$. For the simulation of the rf potential 1 V has been applied to both rf electrodes, while all dc electrodes have been grounded. Here instead of the electric potential the absolute value of the electric field $|\vec{E}_{\text{rf}}(x, y, z)|$ was simulated. The resulting simulation data were exported along the trap axis and on radial planes in the centre of each trap segment.

The obtained data files have been imported into Matlab in the form of matrices with dimensions $2 \times N$ for the z -axis and $3 \times N$ for the radial planes. The import routine only reads data that are within a specified region of interest. The region of interest is chosen to be ± 0.4 mm in the x - and y -coordinate and ± 0.5 mm from each segment centre in z -direction. Because the mesh of the FEM simulation is generated by the software the data points of each datafile do not have values at identical coordinates. Therefore, in a first step all data sets are interpolated linearly in order to receive data at a grid with fixed spacing. The grid size for the xy -planes have been selected to be 200×200 points corresponding to a grid spacing of $4 \mu\text{m}$. For the z -axis the spacing of the data points is $20 \mu\text{m}$. The rf potential is calculated using Eq. 2.28. Then all potentials are multiplied with the respective applied voltage and summed up in order to receive the total ponderomotive trap potential in radial direction $V_{\text{p,rad}}(x, y)$ and in axial direction $V_{\text{p,ax}}(z)$.

In order to find the orientation of the radial trap axes line cuts of the potential are generated with varying orientation angles. Through parabola fits to the line cuts the orientation of the strongest and weakest confinement is found and the trap frequencies are calculated. The fit range for the parabola fit is limited to $\pm 100 \mu\text{m}$ around the

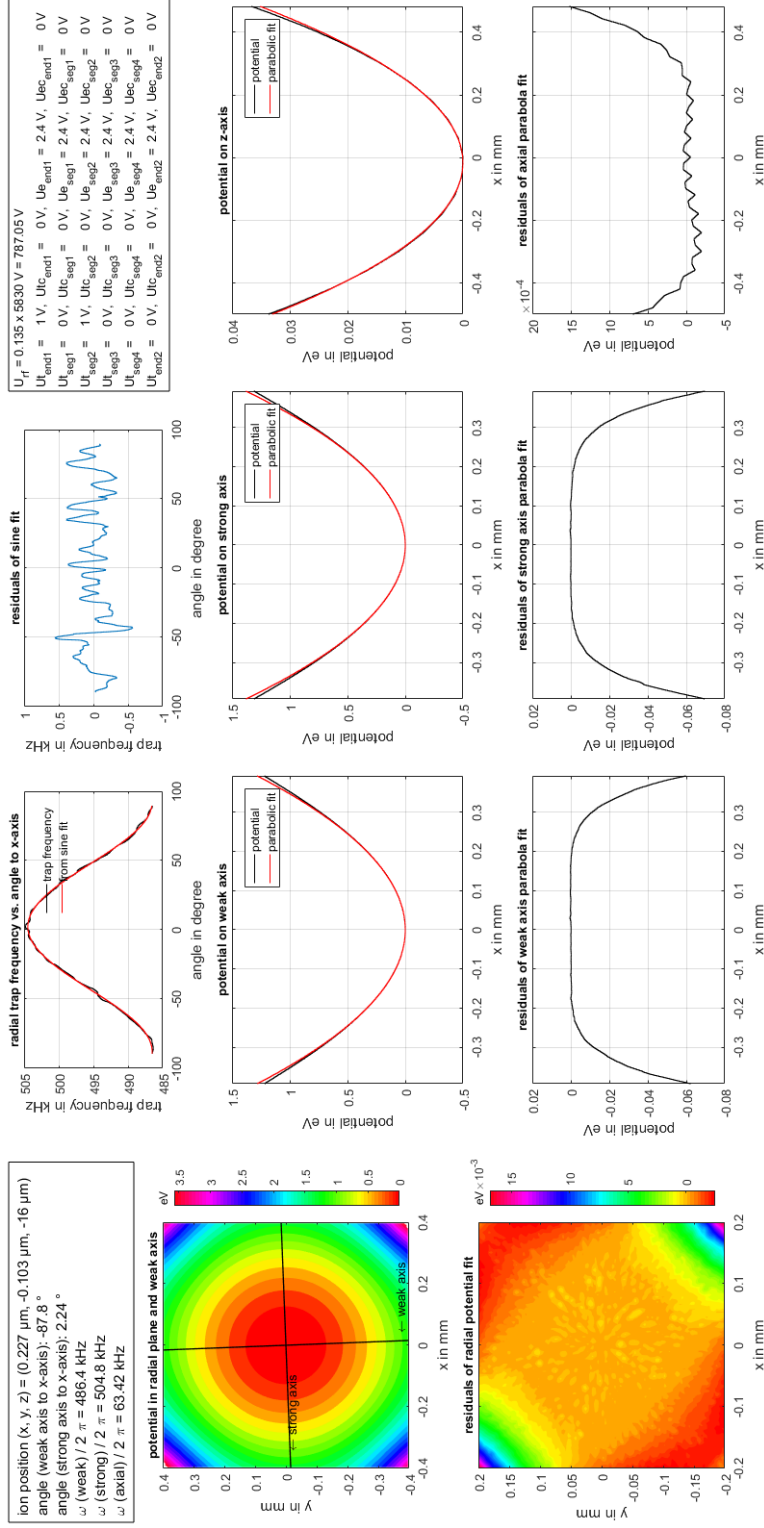


Figure A.4.: Example of the graphical output of the trap potential simulator for typical experimental parameters. On the upper left corner the position of the potential minimum as well as the resulting trap frequencies and the orientation of the radial trap axes are displayed. The graphs show different illustrations of the radial and axial potentials, of the fit functions and of the residuals as described in the figure.

centre, which empirically showed the best results. The axial trap frequency is also determined by a parabola fit to the potential. Finally, the trap potentials, the fit functions and the residuals are presented graphically as shown in Fig. A.4.

Bibliography

- [1] D. Landes, *Revolution in Time: Clocks and the Making of the Modern World*, Harvard University Press, 2000 (cit. on p. 1).
- [2] F. L. Walls and J. R. Vig, „Fundamental limits on the frequency stabilities of crystal oscillators“, *IEEE Transactions on Ultrasonics, Ferroelectrics, and Frequency Control* **42**, 576–589 (1995), ISSN: 0885-3010 (cit. on p. 1).
- [3] L. Essen and J. V. L. Parry, „An Atomic Standard of Frequency and Time Interval: A Cæsium Resonator“, *Nature* **176**, 280–282 (1955) (cit. on p. 1).
- [4] J. C. Maxwell, *The scientific papers of James Clerk Maxwell*, ed. by W. D. Niven, vol. II, Cambridge University Press, 1890 (cit. on p. 1).
- [5] J. Terrien, „News from the International Bureau of Weights and Measures“, *Metrologia* **4**, 41–45 (1968) (cit. on p. 1).
- [6] J. Guéna et al., „First international comparison of fountain primary frequency standards via a long distance optical fiber link“, *Metrologia* **54**, 348–354 (2017) (cit. on p. 1).
- [7] B. J. Bloom et al., „An optical lattice clock with accuracy and stability at the 10-18 level“, *Nature* **506**, 71 (2014) (cit. on p. 1).
- [8] N. Huntemann et al., „Single-Ion Atomic Clock with 3×10^{-18} Systematic Uncertainty“, *Phys. Rev. Lett.* **116**, 063001 (2016) (cit. on pp. 1, 2, 7, 23, 25, 119).
- [9] C. W. Chou et al., „Frequency Comparison of Two High-Accuracy Al^+ Optical Clocks“, *Phys. Rev. Lett.* **104**, 070802 (2010) (cit. on pp. 1, 2, 23, 25).
- [10] A. L. Schawlow and C. H. Townes, „Infrared and Optical Masers“, *Phys. Rev.* **112**, 1940–1949 (1958) (cit. on p. 1).
- [11] T. H. Maiman, „Stimulated Optical Radiation in Ruby“, *Nature* **187**, 493–494 (1960), ISSN: 1476-4687 (cit. on p. 1).
- [12] T. W. Hänsch and A. L. Schawlow, „Cooling of gases by laser radiation“, *Opt. Commun.* **13**, 68 (1975) (cit. on pp. 1, 19).
- [13] D. J. Wineland and H. Dehmelt, „Proposed $10^{14} \delta\nu/\nu$ laser fluorescence spectroscopy on Tl^+ mono-ion oscillator III (sideband cooling)“, *Bull. Am. Phys. Soc.* **20**, 637 (1975) (cit. on pp. 1, 19, 20).
- [14] B. C. Young et al., „Visible Lasers with Subhertz Linewidths“, *Phys. Rev. Lett.* **82**, 3799–3802 (1999) (cit. on p. 1).
- [15] T. Udem, R. Holzwarth, and T. W. Hänsch, „Optical frequency metrology“, *Nature* **416**, 233–237 (2002) (cit. on pp. 2, 5).

- [16] A. D. Ludlow et al., „Optical Atomic Clocks“, *Rev. Mod. Phys.* **87**, 637 (2015) (cit. on pp. 2, 5, 23, 28, 120).
- [17] N. Huntemann et al., „Improved Limit on a Temporal Variation of m_p/m_e from Comparisons of Yb^+ and Cs Atomic Clocks“, *Phys. Rev. Lett.* **113**, 210802 (2014) (cit. on pp. 2, 120).
- [18] R. M. Godun et al., „Frequency Ratio of Two Optical Clock Transitions in $^{171}\text{Yb}^+$ and Constraints on the Time Variation of Fundamental Constants“, *Phys. Rev. Lett.* **113**, 210801 (2014) (cit. on pp. 2, 120).
- [19] T. Pruttivarasin, M. Ramm, and H. Häffner, „Direct spectroscopy of the $^2\text{S}_{1/2} - ^2\text{P}_{1/2}$ and $^2\text{D}_{3/2} - ^2\text{P}_{1/2}$ transitions and observation of micromotion modulated spectra in trapped $^{40}\text{Ca}^+$ “, *J. Phys. B* **47**, 135002 (2014) (cit. on pp. 2, 120).
- [20] V. A. Dzuba et al., „Strongly enhanced effects of Lorentz symmetry violation in entangled Yb^+ ions“, *Nature Physics* **12**, 465 (2016) (cit. on pp. 2, 120).
- [21] P. Delva et al., „Test of Special Relativity Using a Fiber Network of Optical Clocks“, *Phys. Rev. Lett.* **118**, 221102 (2017) (cit. on p. 2).
- [22] A. Bjerhammar, „On a relativistic geodesy“, *B. Geod.* **59**, 207–220 (1985) (cit. on pp. 2, 120).
- [23] T. E. Mehlstäubler et al., „Atomic clocks for geodesy“, *Reports on Progress in Physics* **81**, 064401 (2018) (cit. on pp. 2, 120).
- [24] W. Paul, H. P. Reinhard, and U. von Zahn, „Das elektrische Massenfilter als Massenspektrometer und Isotopentrenner“, *Z. Phys.* **152**, 143–182 (1958) (cit. on p. 2).
- [25] W. Paul, „Electromagnetic traps for charged and neutral particles“, *Rev. Mod. Phys.* **62**, 531–540 (1990) (cit. on p. 2).
- [26] P. Dubé et al., „High-Accuracy Measurement of the Differential Scalar Polarizability of a $^{88}\text{Sr}^+$ Clock Using the Time-Dilation Effect“, *Phys. Rev. Lett.* **112**, 173002 (2014) (cit. on pp. 2, 119).
- [27] N. Herschbach et al., „Linear Paul trap design for an optical clock with Coulomb crystals“, *Appl. Phys. B* **107**, 891–906 (2012) (cit. on pp. 3, 5, 9, 28, 31, 33, 35, 37, 39, 40, 117).
- [28] C. Champenois et al., „Ion ring in a linear multipole trap for optical frequency metrology“, *Phys. Rev. A* **81**, 043410 (2010) (cit. on p. 3).
- [29] K. Pyka et al., „A high-precision segmented Paul trap with minimized micromotion for an optical multiple-ion clock“, *Appl. Phys. B* **114**, 231–241 (2014) (cit. on pp. 3, 33, 35, 37, 39, 55, 103, 117).
- [30] K. Pyka, „High-precision ion trap for spectroscopy of Coulomb crystals“, PhD thesis, Leibniz-Universität Hannover, 2013 (cit. on pp. 3, 10, 33–35, 37, 39, 44, 50, 55, 59, 61, 62, 67, 72, 99, 103, 117, 119).
- [31] F. Riehle, *Frequency Standards - Basics and Applications*, Wiley-VCH, Weinheim, 2004 (cit. on pp. 5, 95).

-
- [32] D. W. Allan, „Statistics of atomic frequency standards“, *P. IEEE* **54** (1966) (cit. on p. 6).
- [33] W. M. Itano et al., „Quantum projection noise: Population fluctuations in two-level systems“, *Phys. Rev. A* **47**, 3554–3570 (1993) (cit. on p. 7).
- [34] E. Peik, T. Schneider, and C. Tamm, „Laser frequency stabilization to a single ion“, *J. Phys. B* **39**, 145–158 (2006) (cit. on p. 7).
- [35] D. G. Matei et al., „1.5 μm Lasers with Sub-10 mHz Linewidth“, *Phys. Rev. Lett.* **118**, 263202 (2017) (cit. on p. 7).
- [36] S. Häfner et al., „ 8×10^{-17} fractional laser frequency instability with a long room-temperature cavity“, *Opt. Lett.* **40**, 2112–2115 (2015) (cit. on p. 7).
- [37] J. Keller et al., „Simple vibration insensitive cavity for laser stabilization at the 10^{-16} level“, *Appl. Phys. B* **116**, 203–210 (2014) (cit. on pp. 7, 67, 71).
- [38] E. Peik, G. Hollemann, and H. Walther, „Laser cooling and quantum jumps of a single indium ion“, *Phys. Rev. A* **49**, 402–408 (1994) (cit. on p. 8).
- [39] T. Liu et al., „Progress toward a single indium ion optical frequency standard“, *2007 IEEE International Frequency Control Symposium Joint with the 21st European Frequency and Time Forum*, May 2007, pp. 407–411 (cit. on p. 8).
- [40] J. A. Sherman et al., „Progress on indium and barium single ion optical frequency standards“, *Digest of the LEOS Summer Topical Meetings, 2005*. July 2005, pp. 99–100 (cit. on p. 8).
- [41] R. H. Garstang, „Hyperfine structure and intercombination line intensities in the spectra of magnesium, zinc, cadmium and mercury“, *J. Opt. Soc. Am.* **52**, 845 (1962) (cit. on p. 8).
- [42] E. Peik, „Laserspektroskopie an gespeicherten Indium-Ionen“, PhD thesis, Max-Planck-Institut für Quantenoptik, 1993 (cit. on p. 8).
- [43] H. G. Dehmelt, „Mono-ion oscillator as potential ultimate laser frequency standard.“, *IEEE Trans. Instrum. Meas.* **31**, 83–87 (1982) (cit. on p. 8).
- [44] W. Nagourney, J. Sandberg, and H. Dehmelt, „Shelved optical electron amplifier - Observation of quantum jumps“, *Phys. Rev. Lett.* **56**, 2797–2799 (1986) (cit. on pp. 8, 16, 66, 74).
- [45] M. S. Safronova, M. G. Kozlov, and C. W. Clark, „Precision Calculation of Blackbody Radiation Shifts for Optical Frequency Metrology“, *Phys. Rev. Lett.* **107**, 143006 (2011) (cit. on pp. 9, 26).
- [46] T. Becker et al., „High-resolution spectroscopy of a single In^+ ion: Progress towards an optical frequency standard“, *Phys. Rev. A* **63**, 051802 (2001) (cit. on p. 9).
- [47] J. B. Wübbena et al., „Sympathetic cooling of mixed-species two-ion crystals for precision spectroscopy“, *Phys. Rev. A* **85**, 043412 (2012) (cit. on pp. 9, 66).
- [48] P. K. Ghosh, *Ion Traps*, Oxford University Press, 1995 (cit. on pp. 9, 11).
- [49] F. G. Major, V. N. Gheorge, and G. Werth, *Charged Particle Traps*, Springer-Verlag, Heidelberg, 2005 (cit. on p. 9).

- [50] W. Paul, O. Osberghaus, and E. Fischer, research rep. 415, Forschungsber. Wirtsch. Verkehrsminist. Nordrhein-Westfalen, 1958 (cit. on pp. 10, 11).
- [51] M. Combescure, „A quantum particle in a quadrupole radio-frequency trap“, eng, *Annales de l'I.H.P. Physique thorique* **44**, 293–314 (1986) (cit. on p. 14).
- [52] Richard J. Cook, Donn G. Shankland, and Ann L. Wells, „Quantum theory of particle motion in a rapidly oscillating field“, *Phys. Rev. A* **31**, 564–567 (1985) (cit. on p. 14).
- [53] D. F. V. James, „Quantum dynamics of cold trapped ions with application to quantum computation“, *Appl. Phys. B* **66**, 181–190 (1998) (cit. on pp. 15, 73).
- [54] A. Steane, „The ion trap quantum information processor“, *Appl. Phys. B* **64**, 623–643 (1996) (cit. on p. 15).
- [55] G. Morigi and H. Walther, „Two-species Coulomb chains for quantum information“, *European Physical Journal D* **13**, 261–269 (2001) (cit. on p. 15).
- [56] F. Diedrich et al., „Laser cooling to the zero-point energy of motion“, *Phys. Rev. Lett.* **62**, 403–406 (1989) (cit. on pp. 16, 20).
- [57] D. Leibfried et al., „Quantum dynamics of single trapped ions“, *Rev. Mod. Phys.* **75**, 281–324 (2003) (cit. on pp. 16, 17, 19).
- [58] J. Keller, „Spectroscopic characterization of ion motion for an optical clock based on Coulomb crystals“, PhD thesis, Leibniz-Universität Hannover, 2015 (cit. on pp. 16, 66, 67, 71, 75, 77, 78, 94–97, 99, 102).
- [59] R. H. Dicke, „The Effect of Collisions upon the Doppler Width of Spectral Lines“, *Phys. Rev.* **89**, 472–473 (1953) (cit. on p. 18).
- [60] K. E. Cahill and R. J. Glauber, „Ordered Expansions in Boson Amplitude Operators“, *Phys. Rev.* **177**, 1857–1881 (1969) (cit. on p. 18).
- [61] D. J. Wineland and W. M. Itano, „Laser cooling of atoms“, *Phys. Rev. A* **20**, 1521–1540 (1979) (cit. on pp. 18, 19, 22).
- [62] Stig Stenholm, „The semiclassical theory of laser cooling“, *Rev. Mod. Phys.* **58**, 699–739 (1986) (cit. on p. 19).
- [63] Jürgen Eschner et al., „Laser cooling of trapped ions“, *J. Opt. Soc. Am. B* **20**, 1003–1015 (2003) (cit. on pp. 19, 22).
- [64] I. Marzoli et al., „Laser cooling of trapped three-level ions: designing two-level systems for sideband cooling“, *Phys. Rev. A* **49**, 2771–2779 (1994) (cit. on pp. 22, 67).
- [65] D. J. Berkeland et al., „Minimization of ion micromotion in a Paul trap“, *J. Appl. Phys.* **83**, 5025–5033 (1998) (cit. on pp. 24, 25, 27, 94).
- [66] M. Brownnutt et al., „Ion-trap measurements of electric field noise near surfaces“, *Rev. Mod. Phys.* **87**, 1419 (2015) (cit. on pp. 25, 32, 63, 64, 100–102, 118).
- [67] S. G. Porsev and A. Derevianko, „Multipolar theory of blackbody radiation shift of atomic energy levels and its implications for optical lattice clocks“, *Phys. Rev. A* **74**, 020502(R) (2006) (cit. on p. 26).

-
- [68] W. M. Itano, „External-Field Shifts of the $^{199}\text{Hg}^+$ Optical Frequency Standard“, *J. Res. Natl. Inst. Stand. Technol.* **105**, 829–837 (2000) (cit. on pp. 27, 28).
- [69] K. Beloy, D. R. Leibbrandt, and W. M. Itano, „Hyperfine-mediated electric quadrupole shifts in Al^+ and In^+ ion clocks“, *Phys. Rev. A* **95**, 043405 (2017) (cit. on p. 28).
- [70] D. J. Wineland et al., „Experimental issues in coherent quantum-state manipulation of trapped atomic ions“, *J. Res. Natl. Inst. Stand. Technol.* **103**, 259 (1998) (cit. on p. 29).
- [71] G. Kotowski, *Z- Angew. Math., Mech.* **23**, 203 (21943) (cit. on p. 32).
- [72] Y. Wang, F. Franzen, and K. P. Wanczek, *Int. Journ. Mass Spectr. Ion Proc.* **124**, 125 (1993) (cit. on p. 32).
- [73] F. Guidugli and P. Traldi, *Rapid Comm. Mass Spectrom.* **5**, 343 (1991) (cit. on p. 32).
- [74] D. M. Eades, J.V. Johnsen, and R. A. Yost, *J. Am. Soc. Mass Spectrom.* **4**, 917 (1993) (cit. on p. 32).
- [75] R. Alheit et al., *Int. J. Mass Spectr. Ion Proc.* **154**, 155 (1996) (cit. on p. 32).
- [76] M. Doležal et al., „Analysis of thermal radiation in ion traps for optical frequency standards“, *Metrologia* **52**, 842 (2015) (cit. on pp. 42–45, 79, 81, 82, 84–86, 124).
- [77] R. J. Meredith, *Engineers’ Handbook of Industrial Microwave Heating*, The Institution of Electrical Engineers, London, 1988 (cit. on p. 43).
- [78] A. K. Datta and C. A. Ramaswamy, *Handbook of Microwave Technology for Food Applications*, CRC Press, 2001 (cit. on p. 46).
- [79] E. Biémont et al., „Lifetime calculations in Yb II“, *J. Phys. B* **31**, 3321–3333 (1998) (cit. on p. 66).
- [80] B. C. Fawcett and M. Wilson, „Computed Oscillator Strengths, and Landé g-Values, and Lifetimes in Yb II“, *At. Data Nucl. Data Tables* **47**, 241 (1991) (cit. on p. 66).
- [81] M. M. Schauer et al., „Collisional population transfer in trapped Yb^+ ions“, *Phys. Rev. A* **79**, 062705 (2009) (cit. on p. 66).
- [82] T. W. Hänsch and B. Couillaud, „Laser frequency stabilization by polarization spectroscopy of a reflecting reference cavity.“, *Opt. Commun.* **35**, 441–444 (1980) (cit. on p. 70).
- [83] C. F. Roos, „Controlling the quantum state of trapped ions“, PhD thesis, Leopold-Franzens-Universität Innsbruck, 2000 (cit. on p. 73).
- [84] Q. A. Turchette et al., „Heating of trapped ions from the quantum ground state“, *Phys. Rev. A* **61**, 063418 (2000) (cit. on pp. 78, 101).
- [85] Pierre Dubé et al., „Evaluation of systematic shifts of the $^{88}\text{Sr}^+$ single-ion optical frequency standard at the 10^{-17} level“, *Phys. Rev. A* **87**, 023806 (2013) (cit. on p. 78).
- [86] N. Huntemann, „High-Accuracy Optical Clock Based on the Octupole Transition in $^{171}\text{Yb}^+$ “, PhD thesis, Leibniz-Universität Hannover, 2014 (cit. on p. 78).
- [87] J. Keller et al., „Precise determination of micromotion for trapped-ion optical clocks“, *J. Appl. Phys.* **118**, 104501 (2015) (cit. on pp. 94, 95, 97).

- [88] J. R. Johansson, P. D. Nation, and F. Nori, „QuTiP 2: A Python framework for the dynamics of open quantum systems“, *Comput. Phys. Commun.* **184**, 1234–1240 (2013) (cit. on p. 96).
- [89] J. Keller et al., „Probing Time Dilation in Coulomb Crystals in a High-Precision Ion Trap“, *Phys. Rev. Applied* **11**, 011002 (2019) (cit. on pp. 97, 117).
- [90] L. Deslauriers et al., „Scaling and Suppression of Anomalous Heating in Ion Traps“, *Phys. Rev. Lett.* **97**, 103007 (2006) (cit. on p. 101).
- [91] J. Labaziewicz et al., „Temperature Dependence of Electric Field Noise above Gold Surfaces“, *Phys. Rev. Lett.* **101**, 180602 (2008) (cit. on p. 101).
- [92] T. Burgermeister and T. E. Mehlstäubler, „Creation and dynamics of topological defects in ion Coulomb crystals“, *Proceedings of the International School of Physics "Enrico Fermi", Course 189 "Ion Traps for Tomorrow's Applications"*, 115–125 (2015) (cit. on p. 103).
- [93] J. Keller et al., „Controlling systematic frequency uncertainties at the 10^{-19} level in linear Coulomb crystals“, *Phys. Rev. A* **99**, 013405 (2019) (cit. on p. 119).
- [94] K. Pyka, J. Keller et al., „Topological defect formation and spontaneous symmetry breaking in ion Coulomb crystals“, *Nat. Commun.* **4**, 2291 (2013) (cit. on pp. 119, 120).
- [95] H. Landa et al., „Quantum Coherence of Discrete Kink Solitons in Ion Traps“, *Phys. Rev. Lett.* **104**, 043004 (2010) (cit. on p. 120).
- [96] J. Kiethe et al., „Probing nanofriction and Aubry-type signatures in a finite self-organized system“, *Nat. Commun.* **8**, 45364 (2017) (cit. on p. 120).
- [97] J. Kiethe et al., „Nanofriction and motion of topological defects in self-organized ion Coulomb crystals“, *New Journal of Physics* **20**, 123017 (2018) (cit. on p. 120).
- [98] S. Hannig, „Development and characterization of a transportable aluminum ion quantum logic optical clock setup“, PhD thesis, Leibniz-Universität Hannover, 2018 (cit. on p. 120).
- [99] C. Schneider, D. Porras, and T. Schätz, „Experimental quantum simulations of many-body physics with trapped ions“, *Rep. Prog. Phys.* **75**, 024401 (2012) (cit. on p. 120).
- [100] R. Blatt and D. J. Wineland, „Entangled states of trapped atomic ions“, *Nature* **453**, 1008–1015 (2008) (cit. on p. 120).

Lebenslauf

Tobias Burgermeister



Diplom-Physiker

Kurpfalzstraße 2a
75053 Gondelsheim
Tel.: 0160 8805322
tobias.burgermeister@gmx.de

geboren am 8. August 1984 in Groß-Gerau
verheiratet, ein Sohn

Berufliche Laufbahn

Seit 09/2016

Technischer Vertriebsingenieur

Physik Instrumente (PI) GmbH & Co. KG, Karlsruhe

Hochschulausbildung

Seit 07/2012

Promotionsstudium

am QUEST Institute for Experimental Quantum Metrology
der Physikalisch-Technischen Bundesanstalt und
der Leibniz Universität Hannover

Thema: „*Development and characterization of a linear ion trap
for an improved optical clock performance*“

Betreuer: Priv.-Doz. Dr. Tanja E. Mehlstäubler
Prof. Dr. Piet O. Schmidt

07/2011 bis 07/2012

Diplomarbeit

am Institut für Angewandte Physik
der Rheinischen Friedrich-Wilhelms-Universität Bonn

Thema: „Ultrakalte Rubidium-Atome in variablen optischen
Gitterpotentialen“

Betreuer: Prof. Dr. Martin Weitz

09/2005 bis 07/2012

Diplomstudium Physik

an der Rheinischen Friedrich-Wilhelms-Universität Bonn

08/2008 bis 06/2009

Auslandsstudium

an der Universität de València, Spanien

Schulbildung und Zivildienst

06/2004 bis 02/2005	Zivildienst in der Hautklinik des Universitätsklinikums Mainz
08/1995 bis 03/2004	Abitur am Gymnasium zu St. Katharinen Oppenheim

Gondelsheim, 25. April 2019

Tobias Bergermeister

List of publications

- J. Keller, D. Kalincev, T. Burgermeister, A. P. Kulosa, A. Didier, T. Nordmann, J. Kiethe, and T. E. Mehlstäubler, “Probing Time Dilation in Coulomb Crystals in a High-Precision Ion Trap”, *Phys. Rev. Applied* **11**, 0110002 (2019)
- J. Keller, T. Burgermeister, D. Kalincev, A. Didier, A. P. Kulosa, T. Nordmann, J. Kiethe, and T. E. Mehlstäubler, “Controlling systematic frequency uncertainties at the 10⁻¹⁹ level in linear Coulomb crystals”, *Phys. Rev. A* **99**, 013405 (2019)
- J. Keller, T. Burgermeister, D. Kalincev, J. Kiethe, and T. E. Mehlstäubler, “Evaluation of trap-induced systematic frequency shifts for a multi-ion optical clock at the 10⁻¹⁹ level”, *J. Phys.: Conf. Ser.* **723**, 012027 (2016)
- T. Burgermeister, and T. E. Mehlstäubler, “Creation and dynamics of topological defects in ion Coulomb crystals”, *Proceedings of the International School of Physics “Enrico Fermi”, Course 189 “Ion Traps for Tomorrow’s Applications”* (2015)
- M. Doležal, P. Balling, P. B. R. Nisbet-Jones, S. A. King, , J. M. Jones, H. A. Klein, P. Gill, T. Lindvall, A. E. Wallin, M. Merimaa, C. Tamm, C. Sanner, N. Huntemann, N. Scharnhorst, I. D. Leroux, P. O. Schmidt, T. Burgermeister, T. E. Mehlstäubler, and E. Peik, “Analysis of thermal radiation in ion traps for optical frequency standards”, *Metrologia* **52**, 842-856 (2015)
- J. Keller, H. L. Partner, T. Burgermeister, and T. E. Mehlstäubler, “Precise determination of micromotion for trapped-ion optical clocks”, *J. Appl. Phys.* **118**, 104501 (2015)
- H. L. Partner, R. Nigmatullin, T. Burgermeister, J. Keller, K. Pyka, M. B. Plenio, A. Retzker, W. H. Zurek, A. del Campo, and T. E. Mehlstäubler, “Structural phase transitions and topological defects in ion Coulomb crystals”, *Physica B* **460**, 114 (2015)
- H. L. Partner¹, R. Nigmatullin¹, T. Burgermeister, K. Pyka, J. Keller, A. Retzker, M. B. Plenio, and T. E. Mehlstäubler, “Dynamics of topological defects in ion Coulomb crystals”, *New J. Phys.* **15**, 103013 (2013)
- K. Pyka¹, J. Keller¹, H. L. Partner, R. Nigmatullin, T. Burgermeister, D.-M. Meier, K. Kuhlmann, A. Retzker, M. B. Plenio, W. H. Zurek, A. del Campo, and T. E. Mehlstäubler, “Topological defect formation and spontaneous symmetry breaking in ion Coulomb crystals”, *Nat. Commun.* **4**, 2291 (2013)

¹equal contributions

Danke!

An dieser Stelle möchte ich mich bei allen Menschen bedanken, die mich auf dem Weg zu dieser Arbeit begleitet und unterstützt haben. Ohne diese Hilfe wäre diese Arbeit nicht möglich gewesen.

Zuerst möchte ich mich bei Priv.-Doz. Dr. Tanja Mehlstäubler dafür bedanken, dass sie mir die Möglichkeit gegeben hat an diesem spannenden und herausfordernden Experiment mitzuarbeiten. Viele Diskussionen und ihr stetiges Fördern und Fordern haben mich und das Experiment immer weiter vorangebracht. Vielen Dank auch für die Geduld, die mir entgegengebracht wurde. Weiterhin möchte ich mich bei Prof. Dr. Piet O. Schmidt und Prof. Dr. Christof Wunderlich für die Erstellung der Gutachten bedanken. Vielen Dank auch an Prof. Dr. Klemens Hammerer für die Übernahme des Vorsitzes der Promotionskommission.

Mein besonderer Dank gilt auch allen meinen Mitstreitern im Labor. An Karsten Pyka, der das Experiment zu großen Teilen aufgebaut hat. Ein besonderer Dank auch an Jonas Keller, der mir immer die Erklärung geben konnte, die ich benötigt habe, und mit mir die Nächte im Labor verbracht hat. Vielen Dank an Heather Partner für ihre Unterstützung. Vielen Dank auch an Dimitri Kalincev, Jan Kiethe und André Kulosa. Es hat mir immer Freude bereitet mit euch zu arbeiten.

Im Laufe der Zeit haben auch viele Studenten, Praktikanten und FWJler ihren Beitrag geleistet. Durch euch habe auch ich viel gelernt und ihr habt viel geleistet. Vielen Dank dafür an David Meier, Kristijan Kuhlmann, Keshav Thirumalai, Michael Moody, Yong Lu, Henrik Wingerath, Rohit Swankar, Thorben Schmirander, Daniel Pflüger, Jan-Wilke Henke, Ida Sigusch, Achim Byl und Leander Thiessen.

Der Aufbau der Ionenfalle war nur in enger Kollaboration mit dem Fachbereich Wissenschaftlicher Gerätebau möglich. Viele Ideen und Diskussionen waren notwendig um dieses hervorragende Resultat erzielen zu können. Vielen Dank dafür an Frank Loeffler, Rudolf Meeß, Daniel Hagedorn, Holger Kuhn, Alexander Ruhz und Steffen Weiß. Ein Dankeschön auch an Christian Rothleitner und Michael Neugebauer für die Erstellung und Hilfe bei den CT Messungen. Vielen Dank auch an alle Kollegen aus dem PTB-Reinraumzentrum, die mir immer gerne geholfen haben und mir ihre Gerätschaften zur Verfügung gestellt haben.

Eine große Hilfe und Erleichterung war auch immer die schnelle und unkomplizierte Hilfe der Kollegen aus den mechanischen und elektrischen Werkstätten. Vielen Dank dafür an Alex Pablocki, Rebecca Müller, Martin Menzel, Thomas Leder, Hans-Albert Kremling, Burghard Lipphardt, Andreas Hoppmann, Peter Carstens, Julia Fenske, Nikoloi Beev und Michael Kazda.

Für die Organisation und Verwaltung benötigt man Menschen, die stets hilfsbereit sind und gute Laune verbreiten. Vielen Dank an Sandra Ludwig und Birgit Ohlendorf, dass ihr diesen Part übernommen habt.

Vielen Danke auch an alle Kollegen aus den Gruppen von Piet Schmidt und Christian Ospelkaus: Florian Gebert, Sana Amairi, Jannes Wübbena, Yong Wan, Ian Leroux, Chunyan Shi, Nils Scharnhorst, Martina Wahnschaffe, Tobias Leopold, Steven King, Matthias Kohlen, Amado Bautista-Salvador, Henning Hahn, Fabian Wolf, Jan-Christoph Heip, Stephan Hannig, Kornelius Jakobsen, and Johannes Kramer. Es hat immer Spaß gemacht euch als Kollegen zu haben.

Ein besonderes Dankeschön für das Lesen und für die Kommentare zu dieser Arbeit geht an Alexandre Didier, Tabea Nordmann, Jan Kiethe, Dimitri Kalincev und Henning Fürst.

Zuletzt möchte ich mich bei meiner Frau Katharina und meinem Sohn Julian bedanken. In den vielen Stunden über Jahre, die in diese Arbeit geflossen sind, habt ihr mir immer den Rückhalt, die Freude, die Aufmunterung, den Ansporn und die Liebe gegeben, die ich benötigt habe.